UNIVERSITÀ DEGLI STUDI DI PADOVA

Facoltà di Ingegneria
Corso di Laurea Magistrale in Ingegneria
dell'Automazione

a.a. 2010/11

Control and guidance systems for the navigation of a biomimetic autonomous underwater vehicle

RELATORE: Ch.mo Prof. Luca Schenato
CORRELATORE: Ch.mo Prof. Euan McGookin

Alberto Tonello

Padova, 11 Luglio 2011

Abstract

The field of Autonomous Underwater Vehicles (AUVs) has increased dramatically in size and scope over the past three decades. Application areas for AUVs are numerous and varied, from deep sea exploration, to pipeline surveillance to mine clearing.

However, two main factors restricted the potential usage of AUVs. The first limiting factor with the current technology is the duration of missions that can be undertaken and one contributing factor to this is the efficiency of the propulsion system, which is usually based on marine propellers. As fish are highly efficient swimmers greater propulsive efficiency may be possible by mimicking their fish tail propulsion system. Actually, mimicking is a limiting expression, since the interest relies in the comprehension and the mathematical formalization of the mechanism involved in the motion of the animals, creating simplified models which uses in the same way the same principles. This is referred to as ”biomimetic”.

The second limiting factor is associted with the current generation of onboard navigation, guidance and control systems. In fact, for truly autonomous operations, the vehicle needs to have a reliable navigation, guidance and control system, which should work in accord with each other for proper operation.

The main concept behind this work was the design and the implementation of a control and guidance system for the navigation of a biomimetic AUV. In particular, the AUV analysed in this project tries to imitate the appearance and approximate the swimming method of an Atlantic Salmon and, for this reason, has been called RoboSalmon.

Contents

Chapter 1

Introduction

1.1 Preface

In recent years, control systems have assumed an increasingly important role in the development and advancement of modern civilisation and technology.
In particular, the growing in the field of navigation, guidance and control systems, stimulated mainly by the challanges of unsolved aerospace problems, contributed significantly to progress achieved in the development of modern systems and control theories.
As an example, the success of the Soviet Union's satellite technology in the 1950s stimulated the United States to develop their own aerospace technology, thus creating between the two of them new concepts in the field of control system design. The Apollo programme in the 1960s is a classical example of the translation of various navigation, guidance and control concepts into working systems. The early success of these systems soon led to advances in such diverse areas as industrial manufacturing, energy management (Lin, 1991) and underwater vehicles. Although applications of navigation, guidance and control in these areas have shown a profound impact in control theory in general, the majority of research and development continues to find its main application in the aerospace industry.
Navigation, guidance and control of airborne systems have been reported extensively in the literature; however, little attention has been paid to the issue of guidance of autonomous underwater vehicles. Even less attention has been paid when the autonomous underwater vehicle uses a biomimetic propulsion system.
Autonomous underwater vehicles are no longer engineering curiosities. They have been under development for over three decades and, in the last decade, there have been significant advances towards their use in operational missions (Millard and Griffiths, 1998).
Although remotely operated vehicles (ROVs) play an important role in the offshore industry, their operational effectiveness is limited by the tethered cable and the reliance and cost of some kind of support platform. Given these limitations, developments in advance control engineering theory and the computation hardware for analysis, design and implementation, interest in the viability of employing AUVs in operational missions has been revived. The use of autonomous underwater vehicles is increasingly being considered for applications such as cable/pipeline tracking, mines clearing operations, deep sea exploration, feature tracking etc.
The potential usage of autonomous underwater vehicles is restricted by two main factors.
The first is the limitation of battery power, which gives a limit to the time duration of the tasks taken by autonomous underwater vehicles. Most currents vehicles have an autonomy of

just a few hours, after that the batteries need to be recharged. In fact, the main aim in the development of a biomimetic AUV relies in the efficiency improvement that may be possible by mimicking the fish tail propulsion system.

The second limiting factor is associated with the current generation of onboard navigation, guidance and control systems. The vehicles need a reliable and well-integrated navigation, guidance and control system, in which the guidance is the key element. In particular, the task of designing and implementing a suitable guidance and control system for an autonomous underwater vehicle has been undertaken during this project.

1.2 Fish classification

In order to understand how fish propel themselves through the water it is necessary to have an understanding of the basic morphological features common to most fish species.
This section aims to introduce briefly some of the fundamental swimming mechanisms found in nature. The first distinction made between biological swimming modes is between *body and/or caudal fin (BCF) swimming* and *paired and/or median fin (PMF) swimming.*
BCF swimming refers to swimming modes that generate thrust through the use of a translational wave propagated along a portion of the body and translated onto the caudal fin which acts as a propulsive surface.
BCF swimmers are often subcategorized further according to the proportion of the body involved in the propulsive wave, as shown in Figure 1.1, A to I. Typically with a BCF swimmer, the larger the proportion of the body involved in the propulsive wave, the greater the manoeuvrability, and the smaller the proportion of the body involved in the propulsive waves, the greater the efficiency and the speed of locomotion.

Typical BCF swimmers are capable of rapid swimming at speeds of the order of 10 L/s (where L denotes body length) and rapid turning, often taking much less than 1 L to turn 180 degrees.
PMF swimming refers to swimming modes that achieve locomotion through the actuation of paired pectoral fins, dorsal fins, and anal fins or paired dorsal and anal fins, the classification of which can be found in Figure 1.1, J to P.
Typical PMF swimmers are capable of precision manoeuvring with six degrees of freedom, including station-keeping and reversing manoeuvres.

A further classification criterion concerns the type of movement observed in the propulsive structure. The motion is said to be undulatory if a waveform is visible along the propulsive structure, while the motion is oscillatory if thrust is generated by the only oscillation about a fixed point of the propulsive structure.

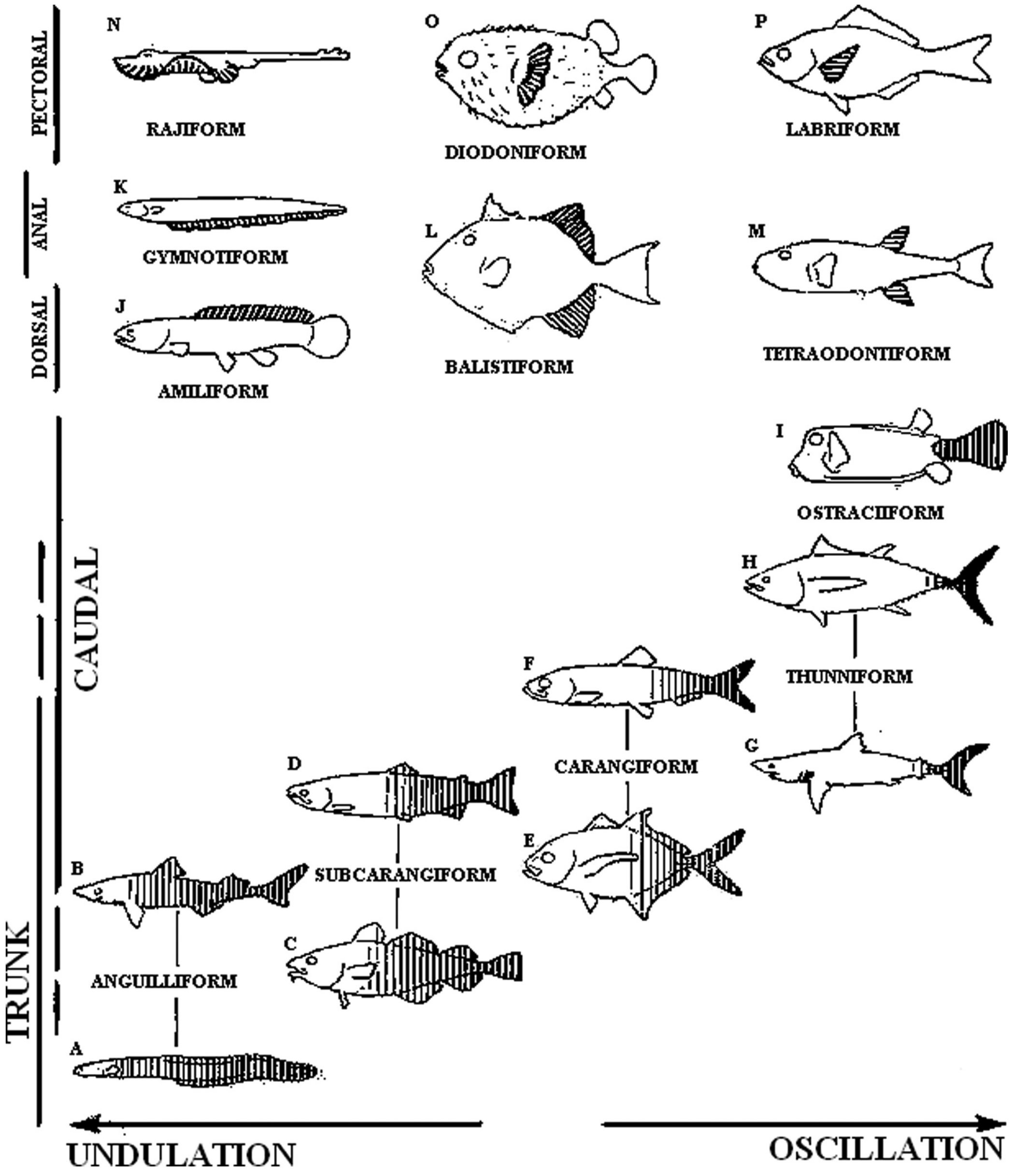

Figure 1.1: A to I show the classification of BCF swimming, while J to P show the classification of PMF swimming.

1.3 State of art

In this section, a summary of the studies and the experimental results achieved so far in AUV biomimetic vehicles is presented. In particular, more attention has been made in the description of the propulsion systems implemented and in the motivation behind the choice of the source of bioinspiration.
It can be noticed that, unlike biological evolution which seems to grow in sophistication with subsequent generations, the evolution of biomimetic swimmers commenced with an intricate complex mechanism and seems to be reducing in complexity with subsequent generations as the fundamental principles are distilled.

1.3.1 BCF swimmers

The ancestry of almost all biomimetic swimmers can be traced back to the *RoboTuna*, designed at the Massachusetts Institute of Technology (MIT). Barrett build RoboTuna [1], which was a 1.2 metres towing-tank replica of a real tuna, in order to understand better the mechanism involved in forward BCF swimming.

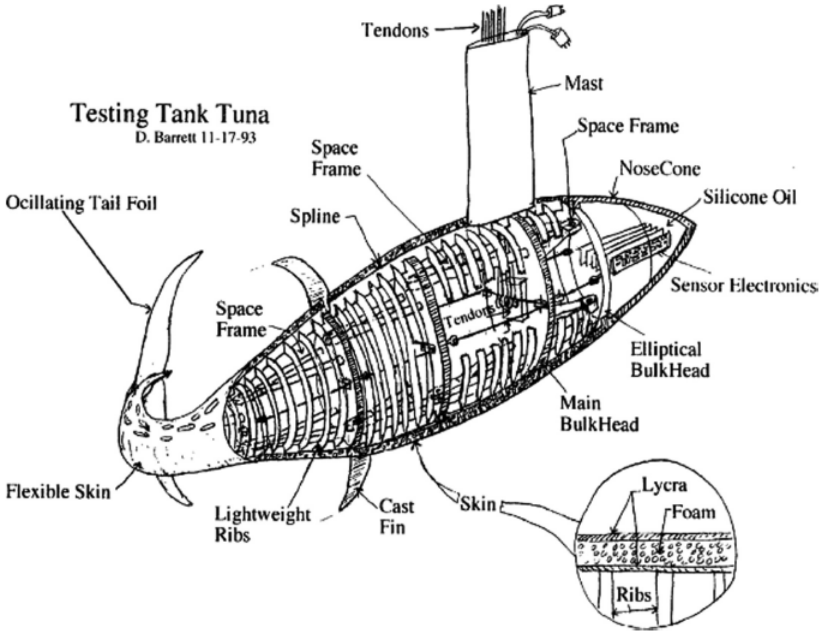

Figure 1.2: A sectional view of MIT's RoboTuna .

The tuna was chosen as a source of bioinspiration because it is one of the fastest-swimming fish in nature and is capable of long periods of swimming at high speeds. Other factors that affected the decision to use a tuna for biological inspiration was that different subspecies of tuna have similar morphologies despite differences in size, implying that any design would be easily scalable for future use as an AUV, and that it was thought that the thunniform swimming mode, which allowed a large proportion of the body to remain rigid, would allow a larger

payload.
A genetic algorithm was used to control the RoboTuna six links, in order to mimic the thunniform locomotion and improve efficiency.

Following the success of the RoboTuna project, MIT in partnership with Draper Laboratories developed the so called *vorticity-controlled unmanned underwater vehicle (VCUUV)* using many of the techniques developed during the RoboTuna project [2]. The VCUUV was designed to be autonomous and have an on-board power supply.
Once again the morphology of a real blue fin tuna was used. However, this time the shape was scaled up to 2.4 metres in length, comparable in size with conventional AUVs in use at the time.
The VCUUV's tail movement came from a simplified five-vertebrae backbone, with the four joints actively controlled by a closed-loop hydraulic system. The backbone, in turn, acted on a spline-and-rib structure. Like RoboTuna, rather than trying to seal a flexible structure, the tail was allowed to be flooded.
The VCUUV is shown in Figure 1.3.

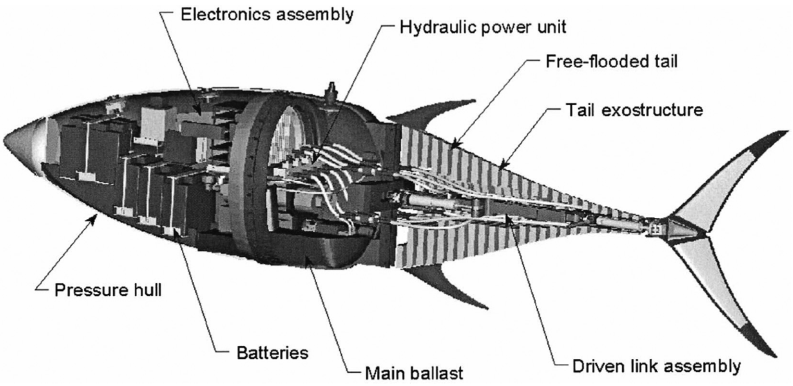

Figure 1.3: A sectional view of Draper Laboratories' VCUUV.

The most recent direct application of the RoboTuna design can be seen in Boston Engineering's *GhostSwimmer*, which is a tuna-based AUV currently being developed under commission from the US government, with advice from Barrett, for use in harbour monitoring [3].

The next generation of robotic swimmers to emerge from MIT was *RoboPike* [4]. The pike was chosen as a source of bioinspiration because of the rapid manoeuvring and acceleration abilities it demonstrates in nature.
RoboPike's tail movement came from a further simplified four-vertebrae backbone, with the three joints actively controlled by tendons driven by waterproofed brushless d.c. servomotors mounted in the midsection of the body, which, together with the tail, was flooded.
RoboPike's forward section was constructed as a single pressure vessel housing batteries and electronic subsystems.

The Japanese National Maritime Research Institute (NMRI) developed a series of further simplified link-based robotic fish, including a three-link 34 cm robotic sea bream denoted *PF-300*,

which was built to study the turning performance [5].
The sea bream was selected as a source of bioinspiration because in nature its large side profile area and carangiform swimming style makes it an excellent fast-turning fish.
The two joints were actuated directly by brushless d.c. servomotors housed in small pressure vessels, the actuation mechanism penetrated the pressure vessel through a corrugated waterproof boot. The tail itself was left in a naked skeletal state, as it was thought that the majority of the propulsive force would be generated by the caudal fin, accurate representation of the rest of the body morphology was thought to be unnecessary.
Subsequent robot swimmers developed by NMRI, include the 65 cm four-link *PF-600*, the 70 cm fourlink *PF-700*, the 97 cm three-link *UPF-2001*, the 26 cm two-link *PF-200*, and the 57 cm three-link *PF-550* [6].
Like PF-300, all the subsequent robot swimmers to emerge from NMRI relied on radio communication remote control, limiting them to operations on or near the surface. All were constructed with open skeletal joints, however, effort was made to approximate the profile of real fish tails by attaching moulded sections to the tail vertebra.

The Tokyo Institute of Technology developed two robotic dolphins aimed as prototypes toward the design of a biomimetically propelled AUV [7].
The first had a pneumatic actuation system, and the second a d.c. servomotor.
Both robots had a three-vertebrae design 1.5 metres in length with one active joint at the top of the tail, and a passive joint at the caudal fin. By varying the stiffness of the passive joint, it was found that a wide variety of tail beat kinematics could be achieved [8].

Developers at the Istanbul Technical University also developed a robotic dolphin AUV prototype with the hope of improving upon the propulsion efficiency found in conventional AUVs [9].
The Istanbul dolphin had a four-vertebrae construction with each of the three joints actuated by an opposing bellows-type pneumatic system.
The flexing tail section was covered in a waterproof membrane supported by a flexible structure to allow the tail joints to remain dry. The caudal fin was made from cast silicon in order to mimic the flexibility of a real dolphin's caudal fin.

In contrast, the University of Essex has developed a series of multi-link carangiform and subcarangiform robot swimmers [10], the latest of which, namely *G9*, is based on a four-vertebrae tail structure constructed using stereolithography apparatus resin. The three joints are actively controlled by three powerful d.c. servomotors [11].
In this case no specific fish was chosen as a source of bioinspiration, instead an attempt was made to capture the more generalized principles of fish morphology.
The Essex fishes are currently being implemented in a collaborative project entitled ”Search and monitoring of harmful contaminants, other pollutants and leaks in vessels in port using a swarm of robotic fish (SHOAL)”.

The Beihang University Robotics Institute also developed a series of robotic fish based on nonspecific bioinspired morphology for use as unmanned underwater vehicles.
SPC-II and *SPC-III* had a common two-joint BCF type propulsion module. The two joints were each actuated by a 150W brushless d.c. motor, located within a sealed part of the vehicle.
SPC-II had a roughly fish-like morphology designed with a large side profile area for rapid

turning ability, with an overall length of 1.2 metres. Despite having a maximum depth rating of only 5 metres the SPC-II proved useful as a visual assistant for underwater archaeology [12]. SPC-III was constructed in many ways like a traditional AUV, [13]. However, in place of the propeller, the two-joint BCF tail was attached, as shown in Figure 1.4.

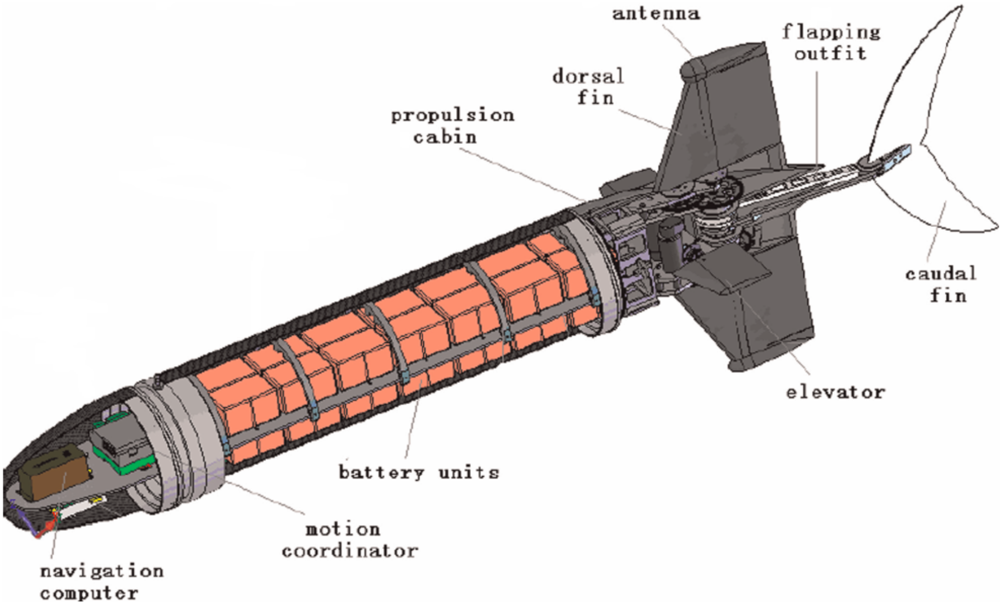

Figure 1.4: A sectional view of Beihang Robotics Institute's SPC-III.

Following on from a study that demonstrated that dead fish exposed to a harmonic stimulus could produce a forward-swimming gait [14], researchers at MIT have developed a simplified compliant body method for generating BCF swimming gaits in small biomimetic AUVs suitable for multi-agent survey tasks [15]. Various compliant body prototypes have been made, one of them can be seen in Figure 1.5.

Reports indicate that these simplified designs have proven to be fairly robust, giving good longevity.

A simple d.c.-servomotor-driven mechanism embedded into a moulded silicon body can produce a travelling body wave if activated harmonically. It was found that, by doping the silicon, the body could be given a different elastic modulus and hence produce different propulsive kinematics.

1.3.2 PMF swimmers

The excellent manoeuvrability and station-keeping ability of PMF swimmers in nature inspired *Kato* [16] at Tokai University to develop the *robotic black bass.*

The black bass was chosen because in nature it is a species known to use pectoral fins for low-speed locomotion and station-keeping manoeuvres.

Two servomotors for each pectoral fin allow the fins to be actuated on the yaw axis and the

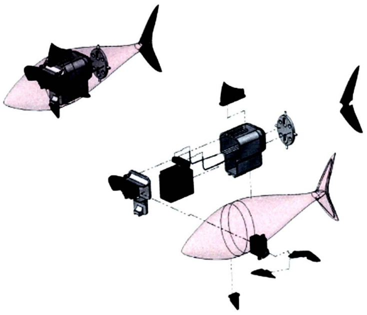

Figure 1.5: An exploded view of MIT's compliant tuna.

pitch axis respectively. By controlling the relative phase and magnitude of yaw and pitch oscillations, manoeuvring forces in the full six degrees of freedom could be achieved.
The black bass project could be considered to be the equivalent for biomimetic PMF locomotion to what RoboTuna was for biomimetic BCF locomotion.

AQUA was a six-finned robot swimmer developed at McGill University [17], shown in Figure 1.6. The swimming gait was roughly based on ostraciform swimming, with the six fins only actuated on the pitch axis and shaped more like flippers than wings.
The AQUA project demonstrated that, by using multiple simple single-axis actuated flippers, heave, surge, pitch, roll, and yaw motions can be achieved.

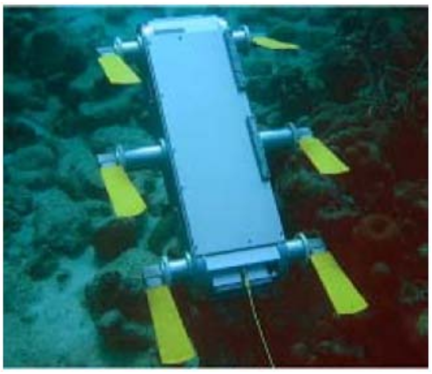

Figure 1.6: The hexapod underwater robot AQUA.

MIT researchers have also developed a multipaired fin swimming AUV [18]. Based roughly on the morphology of a sea turtle, MIT's *RoboTurtle* was a four-finned labriform-type swimmer. For simplicity of expansion, RoboTurtle's fins were constructed as self-contained modules [19]. Each module contained a 190 W d.c. brushed motor to provide actuation in roll, and a 15 W d.c. brushed motor to provide motion in pitch. Like the robotic black bass, manoeuvring forces were controlled by altering the phase and amplitude of oscillations.

A similar four-finned modular design has been adopted by the commercially available *Transphibian* AUV from the iRobot Corporation [20], by using the fins as legs, the Transphibian is also able to produce limited terrestrial locomotion.

Inspired by an observation that, in nature, many amphibious animals despite having four limbs tend to use only two for aquatic propulsion, researchers at Vassar Collage developed a four finned swimming robot called *Madeleine* for experimentation regarding the specific advantages of four and two fin swimming gaits [21].
Experiments indicated that, although the four-fin gait did produce improved acceleration and breaking rates compared with two-fin gaits, the peak velocities achieved were the same for both two and four fin gaits. Furthermore, the overall energy cost of transport for four fin gaits was more than double that of the two fin gaits.

In the commercial sector, Festo has developed manta-ray-based swimmer–glider AUVs, the *AquaRay* [22]. It uses a powerful hydraulic actuation system to control its wings, which have a 96 cm span.
Festo have gone on to use the fin ray effect in their penguin-inspired AUVs. Festo's *AquaPenguin* uses two pectoral fins in a labriform mode for propulsion [23].
Both fins are driven in the roll plane by a single shared d.c. motor, with mechanical gearing to give a synchronized roll oscillation; on each fin, pitch control is achieved using a dedicated d.c. servomotor.
Both Festo's biomimetic AUVs are shown in Figure 1.7.

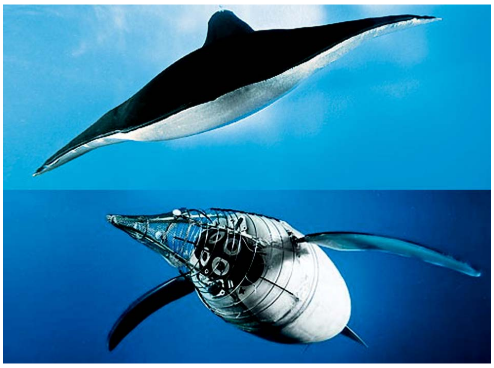

Figure 1.7: Pictures of Festo's AquaRay (top) and Festo's AquaPenguin without the outer skin (bottom).

Another manta-ray-based swimmer–glider AUVs have been developed in the commercial sector by EvoLogics [24]. The *Subsea glider* is available in a variety of sizes from 1.5m up to 3.5m wing span and incorporates a buoyancy-driven glider mechanism and a hydrojet propulsion system for precision manoeuvring as well as the ray-like swimming motion.

Most recently, researchers at the Robotics Institute of Beihang University have developed a robotic cow-nosed ray [25]. *Robo-Ray II* was built over a simple flexible rib, actuated by two McKibben-type pneumatic muscles, and a vertically flexing rudder section, also pneumatically actuated.

North Western University has developed a ribbon fin device based on the gymnotiform locomotion used by the black ghost knife fish [26]. The knife fish was selected as a source of bioinspiration because of its ability to manoeuvre effectively in all six degrees of freedom, including reversing manoeuvres, despite having a relatively stiff body.
The ribbon fin device consists of a flexible membrane suspended between spines arranged in a line down the underside of the craft. The spines themselves are each oscillated in the roll plane. By controlling the phase and amplitude of the oscillations, it was found that a propulsive wave could be propagated forwards or backwards and the introduction of various offsets could generate a great variety of manoeuvres.

Similar ribbon fin devices were used for propulsion systems in small-scale experimental robots developed at Nanyang Technological University [27]. A robotic knife fish using gymnotiform propulsion and a robotic stingray using rajiform propulsion had two such ribbon fin devices which were mounted in the pectoral positions for propulsion.

The most practically scaled example of such a propulsion mechanism can be found in the Delft University's *Galatea*, a box-like AUV using rajiform locomotion [28].

1.3.3 Combined BCF and PMF swimmers

Having developed both fast efficient BCF swimming and precision-stable PMF swimming mechanisms, the natural logical progression is to combine both to create a versatile AUV platform. Although several BCF swimming robots have incorporated actuated pectoral fins for vertical lift generation, there have been relatively few attempts to incorporate more sophisticated pectoral fin manoeuvring systems into BCF swimmers.

Peking University has been developing a 1.2 metres robotic dolphin, which combines BCF and PMF swimming.
The BCF motion comes from a novel adjustable amplitude Scotch yoke mechanism driven by a 150 W d.c. brush motor, which drives the tail section [29], and a 20 W d.c. servomotor, which actively controls the caudal fin.
The PMF motion comes from pectoral fin modules, which are similar to those used on the RoboTurtle, and enable the robotic dolphin to perform stationkeeping and reversing manoeuvres [30].

Taiwan University's *Biomimetic Autonomous Underwater Vehicle (BAUV)* is a 2.4m biologically inspired swimming robot that incorporates a threevertebrae BCF swimming mechanism, with two pectoral fins actuated in roll and pitch, to provide both high-speed BCF swimming with PMF precision manoeuvring [31].

Developers at the Chinese Academy of Science Beijing have developed a 78 cm biomimetic swimmer that uses a novel mechanical linkage system similar to that used in UPF-2001 to derive actuated control over two links from a single d.c. motor to provide BCF propulsion [32].
PMF manoeuvring comes from two pectoral fins driven by a three-motor arrangement similar to that found in Festo's AquaPenguin, giving active roll and pitch control for labriform locomotion.

1.4 Contribution to the field

The design of a biomimetic propulsion system for an autonomous underwater vehicle tries to accomplish the task of increasing the efficiency of the propulsion system, thus decreasing the the problem of the limitation of battery power.
The RoboSalmon biomimetic vehicle has been designed with the purpose of recreating the shape and the charaterics of a real Salmon fish, in order to achieve the efficiency and performance advantages that their tail propulsion system have in nature.
The main task presented in the thesis is the design and the implementation of a suitable control and guidance system for the navigation of the RoboSalmon vehicle.

- **Control system:** The first thing analysed is the control system, which has the task of making the RoboSalmon reach and maintain the desired heading reference. During this phase of the project, two different steering control systems have been designed, the first uses the simple and well-known PID control algorythm, while the second uses the sliding mode control.
  Both the control algorythms designed have been implemented and the simulations have proved that both the steering control systems guarantee a suitable heading control.
  Simulations analysing the differences between the two heading control algorythms has been presented, and the sliding mode control has proved itself to guarantee better performances than the PID one.

- **Guidance system:** After the implementation of a suitable steering control system, the next step is the implementation of the guidance system.
  The guidance system designed uses the Line of Sight (LOS) algorythm to elaborate the right heading, which is supposed to feed the steering control system, in order to reach the desired waypoint.
  Simulations show that the control and guidance systems designed allow to follow the desired set of waypoints, even in presence of ocean current disturbances. Even in this case, the differences between the control and guidance systems with the PID and the sliding mode steering control have been analysed, and the sliding mode has shown to guarantee better performances even in terms of waypoint reaching.

1.5 Thesis outline

The first part of the work carried out was the design, development and construction of the RoboSalmon prototype hardware. Chapter 2 describes the RoboSalmon hardware in detail, covering the reasons for the design decisions and an overview of all of the onboard electronic and mechanical systems.
In particular, a special effort has been made on the description and the mechanical implementation of the tendon drive tail propulsion system.
In the last part of the chapter the performances of the RoboSalmon are presented. In particular, the chapter concludes with an experimental comparison of the performance of the biomimetic tendon drive propulsion system with a conventional propeller based system on a similar vehicle.

The development of the mathematical model is described in Chapter 3. This modelling process covers the kinematics and dynamics of the RoboSalmon vehicle to assist with the understanding of the dynamics of the swimming process.
Details of the method used to model the tendon drive propulsion system are presented. Details of the modelling of the recoil motion are also given.

Chapter 4 presents the design and implementation of two different steering control systems for the RoboSalmon biomimetic vehicle. The first system uses the PID algorythm, while the second one uses the sliding mode control.
The chapter concludes with a simulation comparison of the performances of the RoboSalmon vehicle using both the heading control systems implemented.

The aim of the project, namely the implementation of a control and guidance system for the navigation of the RoboSalmon biomimetic vehicle, is presented in chapter 5.
In the first section of the chapter, a number of approaches that have been adopted for the guidance of air and sea vehicles, with an amphasis on autonomous underwater vehicles, is discussed.
In the second section, the line of sight guidance law (LOS) is presented. Particular effort has been made in the description of its design and implementation on the RoboSalmon vehicle.
Subsequently, in the last section of the chapter, a comparison between the LOS guidance law using the sliding mode control and the PID algorithms for the heading control of the RoboSalmon is illustrated.

Chapter 6 presents the ocean current model, in particular the two dimensinal case will be emphasized.
Subsequently, the integration of the ocean current model previously mentioned in the RoboSalmon's dynamics equation is presented
In order to study the behaviour of the vehicle in the presence of ocean current disturbances, in the last part of the chapter, simulations are presented.

Finally, chapter 7 presents the conclusions that have been drawn from this work along with a brief overview of how the results compare with the main aims and objectives previously set out in this introduction. Possible future developments are outlined as well.

Chapter 2

The RoboSalmon

Material covered in the previous chapter on AUVs provides an insight into the current uses of AUVs and shows how the application of biomimetics may provide certain benefits to underwater propulsion, in particular the propulsion efficiencies.
The main aim of the project, as previously mentioned, was the design of a suitable control and guidance system for an autonomous underwater vehicle. The AUVs, on which the system has been implemented, is the RoboSalmon. Therefore, before proceeding with the description of the project, the RoboSalmon biomimetic vehicle has to be described.
In this chapter the RoboSalmon is presented. Firstly the morphology of the vehicle is described, then its mechanical construction is illustrated, particular emphasy has been made on the description of the tail propulsion system.
More informations concerning the RoboSalmon biomimetic vehicle can be found in [33]

2.1 RoboSalmon morphology

When designing the RoboSalmon vehicle the aim has been to imitate the appearance and approximate the swimming motion of an Atlantic Salmon.
This particular species has been selected due to a number of factors including the importance of this species to the English national economy and the requirement to better understand the current decline in the stocks of this fish.
Work carried out on the design of fish passes for dams has also been a factor because of the need to understand the swimming motions and behaviour of Salmon. This crucial understanding of the biological behaviour of Salmon has allowed optimum, environmentally friendly fish passes to be developed.
Also, in terms of swimming performance, a Salmon has a good balance between speed and manoeuvrability, as is demonstrated in their interesting life cycle which requires them to swim in fast flowing rivers and in the ocean.
Lastly, from a technical perspective, the size of adult Atlantic Salmon should allow the prototype to have sufficient internal volume for location of all the required electrical and mechanical systems. The manageable size of the atlantic salmon is also beneficial as it enables a relatively smaller water tank to be used in the testing process, which is in stark contrast with some larger underwater vehicles that require specialist testing facilities and a team of operators.

2.2 RoboSalmon hardware

The first prototype was the RoboSalmon V1.0, shown in Figure 2.1. However, due to many limitations and reliability issues which prevented the gathering of any meaningful quantitative experimental data, no further investigations has been made on the prototype.

Figure 2.1: RoboSalmon V1.0 prototype.

The main aim with the design of the RoboSalmon V2.0 has been to develop a low cost, reliable and easy to use vehicle which would be a platform to allow various experiments to be carried out to determine the effectiveness of biomimetic propulsion systems.
The RoboSalmon vehicle is 0.85 m in lengths, weights 4.88 kg and is modelled on the relative dimensions of an adult Atlantic Salmon. The vehicle is split into two sections, the body, which contains the sensors, batteries and various other systems, and the tail, which is used for propulsion.
RoboSalmon hardware has been designed to be modular so as to allow multiple propulsion systems to be attached to a common body. Adopting this approach has reduced costs and construction time as only one body section would be needed for the project and different tail sections could be attached as and when completed. It also allows for easy expansion for future investigations out with the scope of this project.
A photograph of the RoboSalmon V2.0 is shown in Figure 2.2.

Figure 2.2: RoboSalmon V2.0 vehicle with Tendon drive tail attached.

The body section is constructed using a rigid aluminium frame onto which the housings for the electronics are fixed. Three waterproof enclosures are available for the electronics within the body, two on the main body and one small enclosure located in the head. This arrangement is illustrated in Figure 2.3.

The body section is designed to be flooded so as to make ballasting the vehicle for correct trim as simple as possible. Thin shaped sections, constructed from fibreglass, are secured around the body section to give the vehicle the shape and appearance of a fish. Shaped styrofoam was attached around the head section to give the appearance of a fish head instead of fibreglass due to buoyancy requirements and to reduce the load on the head servo.

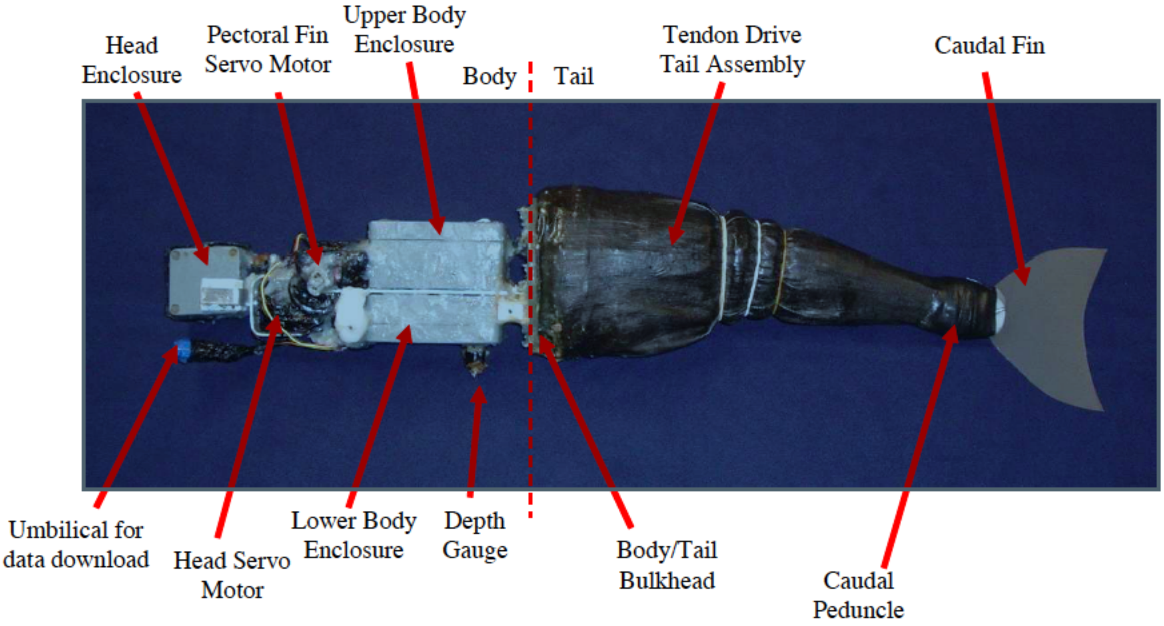

Figure 2.3: Photograph of body section of RoboSalmon V2.0 with shaped fibreglass body sections removed.

In addition the body section also houses two systems to assist with the investigation into the swimming characteristics of the vehicle, two servos which operate together and have rigid fins connected, which are intended to act as dive planes to allow the vehicle to alter its depth, and one servo, which actuates the head of the vehicle allowing it to turn from side to side with respect to the body.

One thing noticed is that water leaking into sensitive areas of the RoboSalmon causes a number of problems, not just electrical. As soon as significant amounts of water leak into the hull the buoyancy and trim of the vehicle is altered, this is usually fairly easy to notice and is one way to determine if there is a leak. One other problem is that any metal within the hull corrodes if it is not designed for use underwater. This includes some machine screws and bolts as well as electronic components and printed circuit boards.

In order to limit the problems caused by water leaks, as well as the waterproof body, the printed circuit boards and electric components were given a coating of special waterproof lacquer. Also, the PCBs are, where possible, mounted towards the top of the hull boxes so that if a leak does occur then it would be some time before water comes into contact with the circuit board.

2.2.1 Propulsion system

Two tail propulsion systems have been developed. The first was the biomimetic tendon drive system. The second system was a propulsion system based on a conventional propeller and rudder system, to allow for a comparison to be made between a biomimetic propulsion system and a more conventional system. The results of the comparison will be presented in the last section of this chapter.

Since the control and guidance system have been designed only for the biomimetic tendon drive tail propulsion system, only the design, mechanics and control electronics of this actuation system is discussed in the following sections.

Tendon drive propulsion system

The propulsion system implemented on the RoboSalmon vehicle wants to reproduce the tail of the real Atlantic Salmon fish. For this reason, the basis for design of the tendon tail is a similar concept to the spine found on living fish, i.e. many joints actuated by the contraction and expansion of the muscles on either side of the spine.

This tail section is made up of a central spine comprising ten plastic joints, as shown in Figure 2.4. Oval shaped rib sections made of thin PVC sheet are attached to the spine to provide the required external shape of the tail. Two tendon wires, which are attached to the front end of the caudal fin, run along each side of the spine and are connected to the arms of a d.c. servo-motor. It is the reciprocal motion of the arms of the servo motor that pulls the tendon wires causing the tail to move. This pulling motion is designed to emulate the muscle contraction in a real salmon tail.

In total the tail system occupies just under half of the overall length of the vehicle, therefore it can be thought to approximate the sub-carangiform swimming mode.

This design of tail has been adopted because it provides a simple and cost effective method of realising fish like propulsion. By using a single motor and tendons the complexity of the control and electronic systems is reduced.

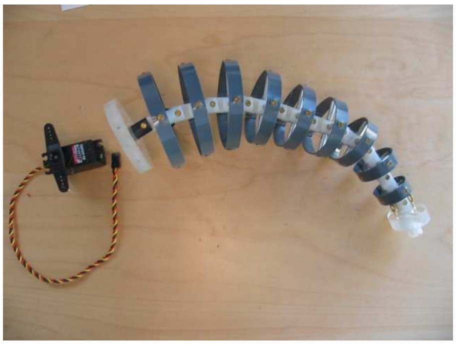

Figure 2.4: Tendon drive tail assembly.

The tendon drive tail is actuated using a Hitec HS-5645 Digital Servo [Hitec RCD, 2007]. The tail control system consists of a PIC 18F2480 8-bit microcontroller [Microchip, 2008] programmed in the C language and a Pololu Micro Servo Control Board [Pololu, 2005]. A single turn rotary potentiometer is attached to the output shaft of the servo to give the servo shaft positional information. This information is useful as it can be used to determine the actual rotational position of the servo motor output shaft as the servo itself provides no feedback on whether it has reached the desired commanded position. The information can also be differentiated numerically to obtain an estimate of the rotational speed of the output shaft. When this rotational velocity is scaled up by the gear ratio used in the servo an estimate of the actual DC motor speed can be also obtained.

To waterproof the tendon tail assembly a bespoke tail skin has been manufactured from liquid latex coated onto a thin nylon base material. This skin is flexible enough not to restrict the motion of the tail too severely whilst maintaining a waterproof barrier. The elastic nature of the skin also assists with the tail motion by providing a degree of restoring force during motion. The tail skin is sealed to the body by means of a compression fit between two plastic plates.

Caudal fin

For the biomimetic tail actuation system a caudal fin attached to the posterior of the tail is required in order to closely mimic a Salmon. Three main factors have to be considered when selecting a fin: shape, size and material.
The caudal fin used on the RoboSalmon tail can be seen in Figure 2.5, together with caudal fin of a real Atlantic Salmon for comparison.

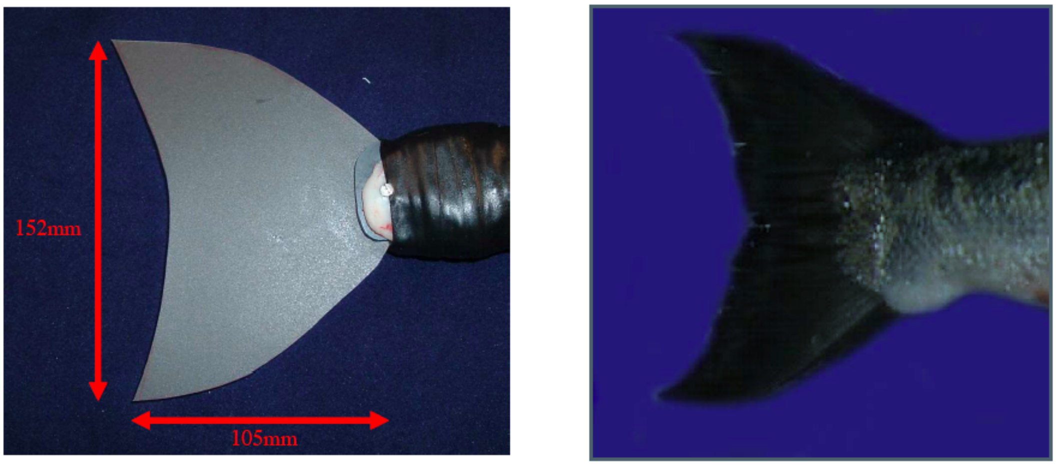

Figure 2.5: Caudal Fin used on tendon drive tail propulsion system (on the left), and caudal fin from real Atlantic Salmon (on the right).

A number of previous studies on the shape of fins for underwater propulsion applications have indicated that a shape close to that of real fish is optimal for developing maximum thrust. Therefore, the shape of the fin has been designed to be as close as possible to the caudal fin shape of a real salmon. The size of the caudal fin is then scaled from the measurements obtained from a real salmon to the dimensions of the RoboSalmon vehicle.

The last parameter required is the material from which to make the caudal fin. The material used to build the fin is flexible plastic, since literature indicate that fish fins are flexible, and that a flexible fin produces more thrust than a rigid fin. During initial testing this fin has been found to provide a surge force without creating an excessive load for the servo motor in the tendon drive system.

2.3 RoboSalmon performances

As stated in the introduction chapter, the efficiency and performance advantages are often cited as the motivation behind the development of biomimetic propulsion systems. However, there exists a distinct lack of data corroborating any such advantages over conventional propeller and rudder propulsion systems. For this reason, the RoboSalmon vehicle has been used in direct comparison experiments between biomimetic and conventional propulsion.

In this section, a brief discussion on the results obtained from the experimentation using the RoboSalmon biomimetic vehicle without any steering control system is presented. Firstly, the results for forward motion are duscussed, followed by the ones obtained when manoeuvring is required.

2.3.1 Forward motion

The first thing analysed during the first experimentation step is the determination of the relationship between tail beat frequency, tail beat amplitude and average forward swimming velocity.

The average forward motion for different tail beat amplitude and frequency is shown graphically in Figure 2.6, with the error bars indicating the range of results obtained for the five runs of each experimental program.

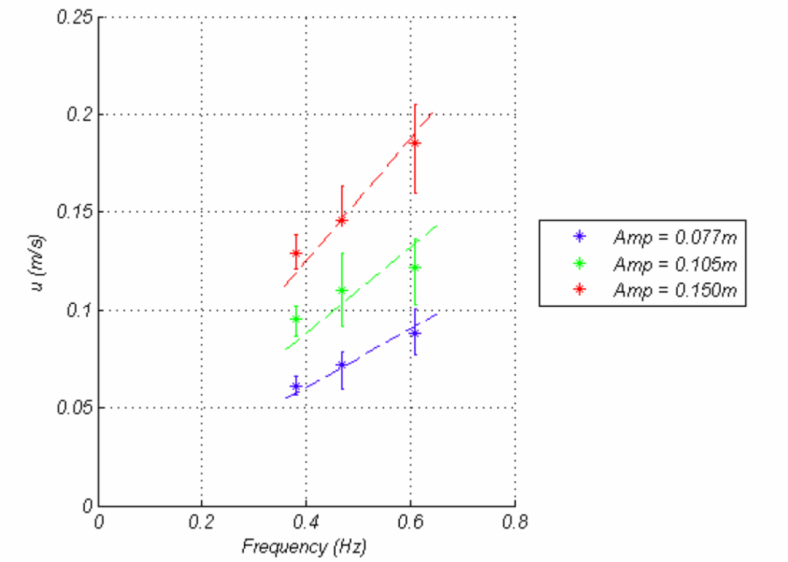

Figure 2.6: Plots of surge velocity versus tail beat frequency for three different tail beat amplitudes with no actuator saturation.

Two important trends for the tendon drive system can be observed. Firstly, for a constant tail beat amplitude it can be seen that, as the frequency increases, the average forward velocity increases. Secondly, with constant tail beat frequency it can be seen that increasing the tail beat amplitude also increases the surge velocity.

A comparison has then been made between the surge performance of the RoboSalmon vehicle and a real salmon, which shows that the performance obtained with the prototype is less than the surge performance of a real salmon by around a factor of three.
In fact, one important characteristic for efficient swimming is the Strouhal number which should lie in the range of 0.25 to 0.35. The data collected during each experimental run for forward swimming allows the Strouhal number to be calculated for each combination of tail beat frequency and tail beat amplitude for the tendon drive system. It has been seen that none of the experimental programs result in a Strouhal number which lies in the quoted range for efficient swimming. One reason for this is that fish very rarely appear to swim at low velocities in the range obtainable from the RoboSalmon.

Another thing that has been noticed during this experimental phase relies in the comparison between the power consumption and the swimming power of the tendon drive system. In fact, the estimate of the power expended in the recoil motion suggests that the power expended in the recoil motion is greater than the useful swimming power obtained.

Finally, there has been a comparison between the tendon drive system and the propeller drive system. This shows that the propeller system is capable of a greater surge speed than the tendon drive system, however the lowest speed obtainable is higher than the tendon drive system. The power consumption calculated from the experimental data for each system shows that at speeds less than $0.2ms^{-1}$ the tendon drive system uses less power for similar surge velocities.
The propulsive efficiencies for each system are then estimated using a combination of experimental data and thrust estimates from theory. When these efficiencies are compared it shows that the tendon drive system is more efficient over the range of surge values $< 0.2ms^{-1}$. However, for higher speeds the efficiencies of both systems would appear to converge if the data for the tendon drive system was extrapolated.

2.3.2 Manoeuvring

The first thing analysed is the turning from stationary performance. It has been seen that the manoeuvres for positive and negative tail offset are not symmetrical as the trajectory of the positive tail offset has more of the turn visible. The reason for this assymetry is due to the construction of the vehicle. Firstly, there may be imperfections in the hull of the vehicle which contribute to this asymmetry when turning. Secondly, there can be slight differences in the tensions of the tendon wires within the tendon drive tail system which, even when the tail is calibrated out of water, will also add to the asymmetry.
The next set of trials conducted was turning from a steady speed which involved the vehicle travelling in a straight trajectory for 8 seconds then adding an offset to the tail centreline for manoeuvring.
In both the experimental sets, it has been seen, as expected, that the larger offset has the smaller turning circle.
A pull out manoeuvre is then used with the tendon drive system which proves that the tendon drive system is capable of carrying out manoeuvres in a similar manner to a conventional vehicle. The pull out manoeuvre also indicates that the RoboSalmon using the tendon drive propulsion system is straight line stable.
The pull out manoeuvre variant used in these experimental trials consists of the vehicle accel-

erating from stationary for a fixed time of 10 seconds with no tail offset, then implementing a costant tail offset for 5 seconds, then removing the tail offset and continuing swimming for a further 10 seconds. This variant does not follow exactly the method described by Fossen [34], due to the experimental aet up used, which only allowed for a limited range of data to be obtained.

Finally, the comparison between the biomimetic and conventional systems indicates that manoeuvring advantages can be obtained by using a tendon drive system in terms of reducing the turning radius. The main conclusions that can be drawn from the manoeuvring trials is that the tendon drive system can achieve superior low speed turning performance when compared to the propeller and rudder based system in terms of turning rates and turning radii.

Chapter 3

Mathematical Model

Recently, the development and use of simulation models is becoming an ever important process. The implementation of prototype hardware can be an expensive and time consuming task, for this reason it is increasengly common place to develop simulation models to predict the behaviour of a system before it is physically constructed. Furthermore the mathematical model allow the development of control algorithms and theories and provide a means for this to be tested before the hardware implementation.

In order to design a control system for the RoboSalmon biomimetic vehicle, it is necessary to develop and validate a simple mathematical model of the vehicle.
Modeling of marine vehicles involves the study of statics and dynamics. Statics is concerned with the equilibrium of bodies at rest or moving with constant velocity, whereas dynamics is concerned with bodies having accelerated motion. Furthermore, it is common to divide the study of dynamics into two parts: kinematics, which treats only geometrical aspects of motion, and kinetics, which is the analysis of the forces causing the motion.
The study of vehicle dynamics in underwater enviroment is, by itself, a complex topic to tackle. Hydrodynamics and unsteady mechanism related to fin-based propulsion make the task of modelling the RoboSalmon vehicle even more challenging.
The development of the mathematical model draws on methods used for modelling conventional marine vessels and techniques used for modelling robot manipulators.
Some differences between the conventional marine vessels model and the RoboSalmon model lay in the vehicle hull, which is designed to approximate that of a fish body, and in the different terms to represent the biomimetic nature of the prototype vehicle, such as the thrust and drug equations for fish propulsion.
In the following sections the various steps to obtain the model differential equations of the RoboSalmon vehicle are presented.
Firstly a brief overview on the notations, including the description of the frames and the model variables, used throughout the work is presented.

3.1 Model variables and reference frames

Before proceeding, a few words to explain the notation adopted throughout the thesis need to be spent.

First of all, when working with any vehicular system, is convinient to define reference frames or coordinate systems. For the mathematical model of the RoboSalmon introduced in this chapter two reference frames of particular interest are used: the earth-fixed frame (or space frame) and the body-fixed frame, as shown in Figure 3.1.

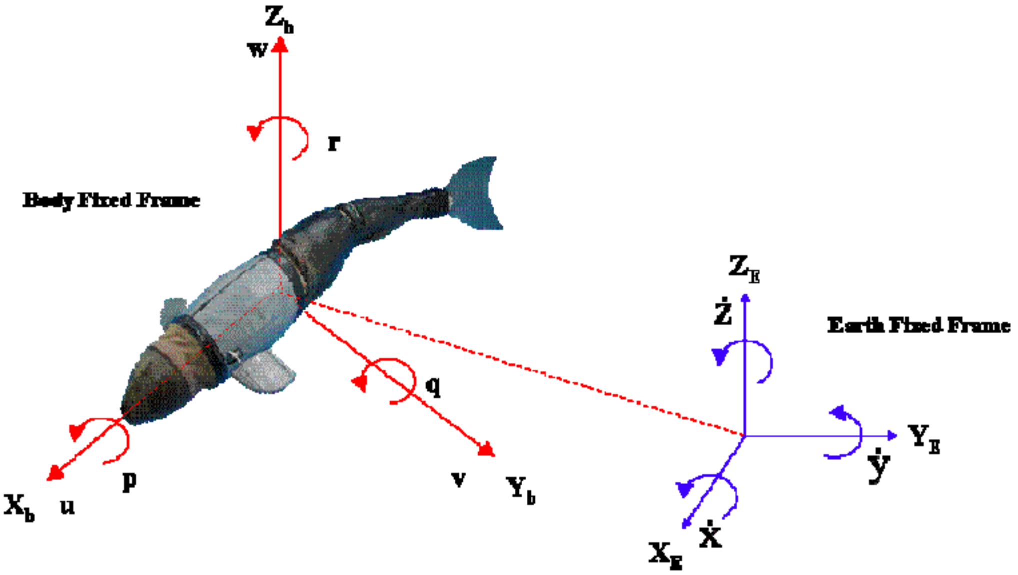

Figure 3.1: Body-fixed frame and earth-fixed frame.

The former is assumed to be fixed to a point in the real word, while the latter is attached to the vehicle and moves with the vehicle as it moves. For simplicity the origin of the body-fixed frame is located at the vehicle's centre of gravity.
Together with the reference frames, it is convinient to define a number of standard variables for describing velocities, desplacemnt, etc. As a vehicle in the space has six degrees of freedom it's convenient to define the variables used to describe the motion of the vehicle in each of these degree of freedom. A standard notation has been developed for use with marine vessels by the Society of Naval Arhitects and Marine Engineers (SNAME) for describing the various forces and moments in each of the six degrees of freedom. The notation adopted throughout the work is shown in Figure 3.2.

In order to simplify the mathematical model development the variables introduced above are usually presented in the vector form, as shown in the following equations (3.1), (3.2) and (3.3).

$$\eta = [\eta_1 \quad \eta_2]^T \tag{3.1}$$

Where $\eta_1 = [x, y, z]^T$ and $\eta_2 = [\phi, \theta, \psi]^T$are rispectively the linear and the angular position of the RoboSalmon in the inertial frame.

$$\nu = [\nu_1 \quad \nu_2]^T \tag{3.2}$$

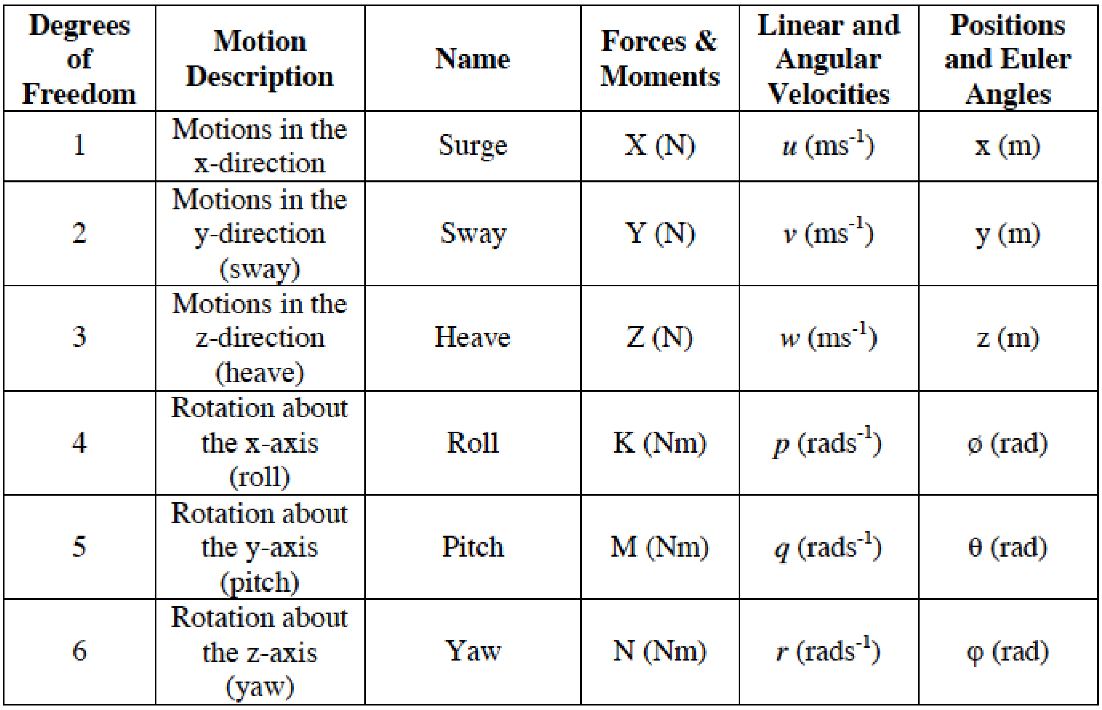

Degrees of Freedom	Motion Description	Name	Forces & Moments	Linear and Angular Velocities	Positions and Euler Angles
1	Motions in the x-direction	Surge	X (N)	u (ms^{-1})	x (m)
2	Motions in the y-direction (sway)	Sway	Y (N)	v (ms^{-1})	y (m)
3	Motions in the z-direction (heave)	Heave	Z (N)	w (ms^{-1})	z (m)
4	Rotation about the x-axis (roll)	Roll	K (Nm)	p (rads^{-1})	ø (rad)
5	Rotation about the y-axis (pitch)	Pitch	M (Nm)	q (rads^{-1})	θ (rad)
6	Rotation about the z-axis (yaw)	Yaw	N (Nm)	r (rads^{-1})	φ (rad)

Figure 3.2: SNAME notation for marine vessels.

Where $\nu_1 = [u, v, w]^T$ and $\nu_2 = [p, q, r]^T$ are rispectively the linear and the angular velocity of the RoboSalmon in the body frame.

$$\tau = [\tau_1 \quad \tau_2]^T \tag{3.3}$$

Where $\tau_1 = [X, Y, Z]^T$ is the force vector while $\tau_2 = [K, M, N]^T$ is the moment vector, both in the RoboSalmon's body frame.

3.2 RoboSalmon kinematics

The velocities and accelerations generated by the dynamics of the RoboSalmon vehicle, which will be discussed in the following section, are calculated with respect to the body-fixed reference frame.
Altough, in most cases, it is useful to know how the vehicle is moving in the earth-fixed reference frame, this is true particularly for tracking purposes. It is therefore usually necessary to translate the forces and velocities generated in the moving body-fixed frame to forces and velocities in the earth-fixed frame, which is assumed to be stationary relative to the body-fixed frame.

In order to translate the body-fixed velocities ,generated by the dynamics section of the model, to velocities in the inertially earth-fixed frame, a transformation is required. This transformation is made up of a series of rotations carried out in a specific order as outlined by *Euler's Theorem on Rotation.*
Generally, any rotation can be thought of as a composition of three sequential rotations. Depending on which axis these rotations are assumed to occur about, different representations are employed. In this case, the ZYX Euler angles are adopted, thus, denoting with ϕ, θ and ψ the roll, pitch and yaw angles respectively, any rotation from the earth-fixed frame to the body-fixed frame can be written as shown in equation (3.4).

$$J = J_x(-\phi)J_y(-\theta)J_x(-\psi) \tag{3.4}$$

Where the single rotation about one axis can be written as

$$J_x = \begin{bmatrix} 1 & 0 & 0 \\ 0 & \cos\phi & -\sin\phi \\ 0 & \sin\phi & \cos\phi \end{bmatrix}, J_y = \begin{bmatrix} \cos\theta & 0 & \sin\theta \\ 0 & 1 & 0 \\ -\sin\theta & 0 & \cos\theta \end{bmatrix}, J_z = \begin{bmatrix} \cos\psi & -\sin\psi & 0 \\ \sin\psi & \cos\psi & 0 \\ 0 & 0 & 1 \end{bmatrix},$$

Hence, the inverse map, from the body-fixed to the earth-fixed frame, can be obtained by transposing the previously presented rotation matrix J.
In order to carry out the transformation previously mentioned the linear and angular velocities are dealt with separately. Therefore, the velocity vector ν has been split into two separate vectors, ν_1 and ν_2, which are the linear and angular velocities in the body-fixed frame respectively, as shown previously in equation (3.2). The corresponding vectors of linear and angular position in the earth-fixed frame are given the notations η_1 and η_2 respectively, as it can be seen in equation (3.1).
The standard notation for the transformation between velocities in the body-fixed frame and velocities in the earth-fixed frame is shown in equations (3.5) and (3.6) for linear and angular velocities respectively.

$$\dot{\eta_1} = J_1(\eta_2)\nu_1 \tag{3.5}$$

$$\dot{\eta_2} = J_2(\eta_2)\nu_2 \tag{3.6}$$

Where $\dot{\eta_1}$ and $\dot{\eta_2}$ are the linear and angular velocities in the earth-fixed frame respectively and J_1 and J_2 represent the transformation matrices created with the composition of three different rotation, as previously mentioned. The rotation matrices for the linear velocities and for the angular velocities are shown in equations (3.7) and (3.8) respectively.

$$J_1(\eta_2) = \begin{bmatrix} c\psi c\theta & -s\psi c\phi + c\psi s\theta s\phi & s\psi s\phi + c\psi c\phi s\theta \\ s\psi c\theta & c\psi c\phi + s\psi s\theta s\phi & -c\psi s\phi + s\psi c\phi s\theta \\ -s\theta & c\theta s\phi & c\theta c\phi \end{bmatrix} \tag{3.7}$$

$$J_2(\eta_2) = \begin{bmatrix} 1 & s\phi t\theta & c\phi t\theta \\ 0 & c\phi & -s\phi \\ 0 & \frac{s\phi}{c\theta} & \frac{c\phi}{c\theta} \end{bmatrix} \tag{3.8}$$

Where, for reason of compactness, c, s and t represent the cosine function, the sine function and the tangent function respectively.

Therefore, the complete kinematic equation for translating from velocities in the body-fixed frame to velocities in the earth-fixed frame rearranged in one equation, as shown in equation (3.9).

$$\dot{\eta} = J(\eta_2)\nu \tag{3.9}$$

3.3 RoboSalmon dynamics

The dynamics of the Robosalmon vehicle in six degrees of freedom are modelled using the standard equation for modelling marine craft shown in (3.10). This equation has the origin of the body fixed frame located at the centre of gravity of the vehicle

$$M\dot{\nu} + C(\nu)\nu + D(\nu)\nu + g(\eta) = \tau \tag{3.10}$$

where $M = M_{rb} + M_a$ is the inertia matrix, composed of the rigid body inertia matrix and the added inertia matrix, $C(\nu) = C_{rb}(\nu) + C_a(\nu)$ is the Coriolis and centripetal matrix, made up of two components, the Coriolis and centripetal matrix due to the rigid body and the terms relating to the added mass effect, $D(\nu)$ is the dumping matrix, $g(\eta)$ is the vector of gravitational forces and moments, τ is the vector of control inputs, and v is the linear and angular velocity vector.
In the following sections each of these terms will be analysed in detail.

3.3.1 Rigid body dynamics

For the development of the mathematical model of the RoboSalmon vehicle, the whole system is assumed to be a rigid body. With this assumption it is implied that both the vehicle mass and shape remain costant and don't alter with time.
The assumption of the costant mass is reasonable, since the no fuel is consumed during the running of the vehicle thanks to the fact that the RoboSalmon is battery powered.
The latter assumption, regarding the costant shape of the vehicle, is not easily justified since the RoboSalmon's propulsion system is made of a moving tail.
However, assuming that the RoboSalmon is a rigid body is a reasonable approximation, since most of the mass is concentreted within the body of the vehicle.

The development of the rigid body equations of the motion is based on the Newton-Euler Formulation which is based on Newton's second law. Newton's second law relates the acceleration and mass of an object to the force acting on it, the mathematical formulation of the law is shown in equation (3.11)

$$\sum \mathbf{F} = m\mathbf{a} \tag{3.11}$$

Where m is the mass of the object in kg, $\mathbf{a}$ is the acceleration vector of the object in ms^{-2} and, finally, $\sum \mathbf{f}$ is the sum of all the forces vectors acting on the body in N.

In order to develop the rigid body equations of the motion of the RoboSalmon, Euler's first and second axioms will be used.
The two axioms express Newton's second law in terms of both linear momentum $\mathbf{p}_c$ and angular momentum $\mathbf{h}_c$, as shown rispectively in equations (3.12) and (3.13).

$$\dot{p}_c = f_c \qquad p_c = m\nu_c \tag{3.12}$$

$$\dot{h}_c = m_c \qquad h_c = I_c\omega \tag{3.13}$$

Where f_c and m_c are rispectively forces and moments referred to the vehicle's centre of gravity, ω is the angular velocity vector, m is the mass of the vehicle's body and I_c is the inertia referred to the body's centre of gravity.

The rigid body equations for each of the six degrees of freedom for the RoboSalmon biomimetic vehicle are shown in the following equations, from (3.14) to (3.19).

$$\text{Surge} \qquad X = m[\dot{u} - vr + wq] \tag{3.14}$$

$$\text{Sway} \qquad Y = m[\dot{v} - wp + ur] \tag{3.15}$$

$$\text{Heave} \qquad Z = m[\dot{w} - uq + vp] \tag{3.16}$$

$$\text{Roll} \qquad K = I_x\dot{p} + (I_z - I_y)qr \tag{3.17}$$

$$\text{Pitch} \qquad M = I_y\dot{q} + (I_zx - I_z)rp \tag{3.18}$$

$$\text{Yaw} \qquad N = I_z\dot{r} + (I_y - I_x)pq \tag{3.19}$$

Where I_x, I_y and I_z are the moment of inertia of the vehicle respectively about the x, y and z axes in the body frame.

Inertia matrix

The inertia matrix M, presented in the dynamics equation (3.10), is composed of two components as shown in equation (3.20).

$$M = M_{rb} + M_a \tag{3.20}$$

Where the first term, M_{rb}, is the rigid body inertia matrix, and the second term, M_a, is the added inertia matrix to take effects due to the added mass forces and inertia into account.

To simplify the matrices it is assumed that the centre of gravity is located at the same position as the origin of the body-fixed frame.

In order to give the vehicle a degree of metastability, the centre of buoyancy is set to coincide with the centre of gravity in the x and y axes, but is set to be slightly above the centre of gravity in the z axis.

In equation (3.21) and (3.22) are respectively shown the coordinates of the centre of gravity, c_g, and the centre of buoyancy, c_b, in the body-fixed frame.

$$c_g = \begin{bmatrix} x_g \\ y_g \\ z_g \end{bmatrix} = \begin{bmatrix} 0 \\ 0 \\ 0 \end{bmatrix} \tag{3.21}$$

$$c_b = \begin{bmatrix} x_b \\ y_b \\ z_b \end{bmatrix} = \begin{bmatrix} 0 \\ 0 \\ 0.02 \end{bmatrix} \tag{3.22}$$

A large number of marine vessel models assume that the vehicle to be modelled is neutrally buoyant. This means that the downward force due to gravity is equal to the upward force due to the water (the buoyancy force).

In reality, achieving neutral buoyancy is a near impossible task without a dynamic ballast system.

The RoboSalmon biomimetic vehicle has been designed to be slightly positively buoyant, so, if

any malfunctions occur, it rises to the surface
Therefore the rigid body inertia matrix for the RoboSalmon simplifies to

$$M_{rb} = \begin{bmatrix} m & 0 & 0 & 0 & 0 & 0 \\ 0 & m & 0 & 0 & 0 & 0 \\ 0 & 0 & m & 0 & 0 & 0 \\ 0 & 0 & 0 & I_x & 0 & 0 \\ 0 & 0 & 0 & 0 & I_y & 0 \\ 0 & 0 & 0 & 0 & 0 & I_z \end{bmatrix}$$

The moments of inertia for the vehicle are calculated using the standard equation for the moment of inertia of a cylinder.

Coriolis and centripetal terms

The centripetal force is caused when the motion of the vehicle follows a curved path.
The Coriolis effect is due to motion of the vehicle within a rotating reference frame.
However, for modelling purposes, the effect of the Coriolis and the centripetal forces acting on the vehicle are dealt with together within one matrix, $C(\nu)$, as shown in equation (3.10).

Like the inertia matrix, the Coriolis and centripetal matrix is made up of two components, as shown in equation (3.23).

$$C(\nu) = C_{rb}(\nu) + C_a(\nu) \tag{3.23}$$

Where the first term, $C_{rb}(\nu)$, represents the Coriolis and centripetal matrix due to the rigid body, and the second term, $C_a(\nu)$, is the term relating to the added mass effect.

Since the origin of the body-fixed reference frame is considered to be located at the same position as the centre of gravity, the term $C_{rb}(\nu)$ can be represented as shown in equation (3.3.1).

$$C_{rb} = \begin{bmatrix} 0 & 0 & 0 & 0 & mw & -mv \\ 0 & 0 & 0 & -mw & 0 & mu \\ 0 & 0 & 0 & mv & -mu & 0 \\ 0 & mv & -mv & 0 & I_z r & I_y q \\ -mw & 0 & mu & -I_z r & 0 & I_x p \\ mv & -mu & 0 & I_y q & -I_x p & 0 \end{bmatrix}$$

3.3.2 Hydrodynamic forces and moments

Hydrodynamic added mass terms

In this subsection the inertia and the the Coriolis and centripetal matrices due to the added mass effect will be analysed.
The movement of a submerged body results in a displacement of a portion of the surrounding fluid, namely a part of the fluid moves together with the body. Hence the added mass is a representation of the pressure induced forces and moments due to a forced harmonic motion of the body.

This phenomenon can produce consequential effects on the submerged body dynamics, depending on its geometry, hence it needs to be taken in account by modifying the inertia matrix and the matrix of Coriolis and centripetal terms.
In general, for every external force or moment applied to the submerged body, tha added mass effect produces forces and moments with components in all the three axes of the body-frame. Hence the standard interta matrix M_A containing the the added mass derivatives assumes the structure shown in equation (3.3.2).

$$M_a = \begin{bmatrix} X_{\dot{u}} & X_{\dot{v}} & X_{\dot{w}} & X_{\dot{p}} & X_{\dot{q}} & X_{\dot{r}} \\ Y_{\dot{u}} & Y_{\dot{v}} & Y_{\dot{w}} & Y_{\dot{p}} & Y_{\dot{q}} & Y_{\dot{r}} \\ Z_{\dot{u}} & Z_{\dot{v}} & Z_{\dot{w}} & Z_{\dot{p}} & Z_{\dot{q}} & Z_{\dot{r}} \\ K_{\dot{u}} & K_{\dot{v}} & K_{\dot{w}} & K_{\dot{p}} & K_{\dot{q}} & K_{\dot{r}} \\ M_{\dot{u}} & M_{\dot{v}} & M_{\dot{w}} & M_{\dot{p}} & M_{\dot{q}} & M_{\dot{r}} \\ N_{\dot{u}} & N_{\dot{v}} & N_{\dot{w}} & N_{\dot{p}} & N_{\dot{q}} & N_{\dot{r}} \end{bmatrix}$$

The evaluation of this R^{6x6} matrix can be fairly complex, but, in order to simplify the model, two simplifying hypothesis can be assumed.
Firstly, the motion of an underwater vehicle is usually low speed, non-linear and coupled. Secondly, it can be seen that the are certain symmetries within the RoboSalmon's hull form, which is assumed to be a prolate ellipsoid in shape, shown in Figure 3.3.
Thanks to both these assumptions the added mass matrix can be simplify to only the diagonal elements, as shown in equation (3.3.2).

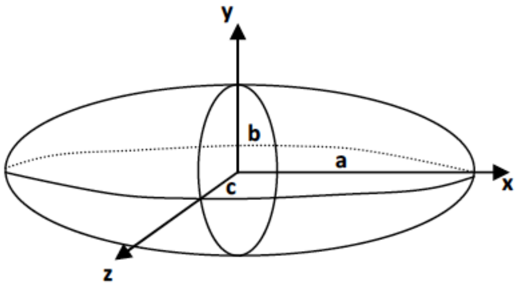

Figure 3.3: Prolate ellipsoid modelling the RoboSalmon's hull shape.

$$M_a = \begin{bmatrix} X_{\dot{u}} & 0 & 0 & 0 & 0 & 0 \\ 0 & Y_{\dot{v}} & 0 & 0 & 0 & 0 \\ 0 & 0 & Z_{\dot{w}} & 0 & 0 & 0 \\ 0 & 0 & 0 & K_{\dot{p}} & 0 & 0 \\ 0 & 0 & 0 & 0 & M_{\dot{q}} & 0 \\ 0 & 0 & 0 & 0 & 0 & N_{\dot{r}} \end{bmatrix}$$

The assumptions previously made, also lead to the simplification of the Coriolis an centripetal matrix due to the added mass terms, as shown in equation (3.3.2)

$$C_a(\nu) = \begin{bmatrix} 0 & 0 & 0 & 0 & -Z_{\dot{w}}w & Y_{\dot{v}}v \\ 0 & 0 & 0 & Z_{\dot{w}}w & 0 & -X_{\dot{u}}u \\ 0 & 0 & 0 & -Y_{\dot{v}}v & X_{\dot{u}}u & 0 \\ 0 & -Z_{\dot{w}}w & Y_{\dot{v}}v & 0 & -N_{\dot{r}}r & M_{\dot{q}}q \\ Z_{\dot{w}}w & 0 & -X_{\dot{u}}u & N_{\dot{r}}r & 0 & -K_{\dot{p}}p \\ -Y_{\dot{v}}v & X_{\dot{u}}u & 0 & -M_{\dot{q}}q & K_{\dot{p}}p & 0 \end{bmatrix}$$

Hence, using the prolate ellipsoid as the shape for the RoboSalmon's hull, the model has to consider only six added mass derivative terms, which can be calculated as shown in equations (3.24) to (3.28).

$$e = 1 - \left(\frac{b}{a}\right)^2 \tag{3.24}$$

$$X_{\dot{u}} = -\frac{\alpha_0}{2-\alpha_0}m \tag{3.25}$$

$$Y_{\dot{v}} = W_{\dot{w}} = -\frac{\beta_0}{2-\beta_0}m \tag{3.26}$$

$$K_{\dot{p}} = 0 \tag{3.27}$$

$$N_{\dot{r}} = M_{\dot{q}} = -\frac{1}{5}\frac{(b^2-a^2)^2(\alpha_0-\beta_0)}{2(b^2-a^2)+(b^2+a^2)(\beta_0-\alpha_0)} \tag{3.28}$$

Where e is the eccentricity and α_0 and β_0 are constants.

Restoring forces and moments

The restoring forces and moments analysed in this section are the terms which take into account the gravitational and buoyancy forces. In order to calcute these forces and moments for underwater vehicles, two parameters are really important. These parameters are the the distance between the origin of the body-fixed reference frame, the centre of gravity (called COG) and the centre of buoyancy (called COB) of the vehicle.

In many underwater vehicle models the vehicle is assumed to be neutrally buoyant, for simplicity reasons. As previously mentioned, obtaining the neutral buoyancy within the hardware is a near impossible task. Neverthless, making this assumption simplifies a number of terms within the mathematical model of the underwater vehicle.

The complete vector of restoring forces and moments, due to gravitational and buoyancy terms, is shown in equation (3.29)

$$g(\eta) = \begin{bmatrix} (W-B)\sin\theta \\ -(W-B)\cos\theta\sin\phi \\ -(W-B)\cos\theta\cos\phi \\ -(y_GW-y_BB)\cos\theta\cos\phi+(z_GW-z_BB)\cos\theta\sin\phi \\ (z_GW-z_BB)\sin\theta+(x_GW-x_BB)\cos\theta\cos\phi \\ -(x_GW-x_BB)\cos\theta\sin\phi-(y_GW-y_BB)\sin\theta \end{bmatrix} \tag{3.29}$$

An important aspect to consider when designing a marine vehicle is the stability in roll. With a correct positioning of both the COG and the COB, it is possible to create a roll restoring

momentwhich acts when the vehicle is subject to an angular roll desplacement taking it away from its upright position. For underwater vehicle, the stability in roll is usually achieved when the COB is positioned above the COG on the z axis.
In order to achieve the roll stability, for the RoboSalmon, the COB is assumed to be above the COG on the z axis, but has equal x and y axis terms. This produces moments which act to bring the underwater vehicle back to its equilibrium after the removal of any external forces.
Many underwater vehicles utilize this approach, used on the RoboSalmon, for passive roll control, as no actuators are required. The RoboSalmon is slightly positively buoyant, since the COB is positioned above the COG on the z axis, and much effort has been expended to make the COG and the COB as close as possible on the x and y axes.
The restoring forces and moments vector used for the simulation of the RoboSalmon vehicle is given in equation (3.30).

$$g(\eta) = \begin{bmatrix} 0 \\ 0 \\ 0 \\ (z_G W - z_B B)\cos\theta\sin\phi \\ (z_G W - z_B B)\sin\theta \\ 0 \end{bmatrix} \tag{3.30}$$

Hydrodynamic damping terms

The hydrodynamic damping or drag is a force that acts on any vehicle operating in the underwater environment. This force contribute to the dynamics of the vehicle, since it is required in the forces and moments section of the model to represent the drag force.
Damping is approximated using the standard equation for drag shown in equation (3.31).

$$f(U) = -\frac{1}{2}\rho C_D A|U|U \tag{3.31}$$

Where ρ is the density of fluid (kgm^{-3}), C_D is the drag coefficient, A is the cross-sectional area (m^2) and U is the velocity of the vehicle (ms^{-1}). This equation is used to calculate the drag force acting in surge, sway and heave, and it is also used to estimate the rotational drag terms in roll, pitch and yaw.
The equation for drag requires the drag coefficient C_D to be known in each degree of freedom. As the body of the RoboSalmon is not just a prolate ellipsoid, but an ellipsoid with fins, the drag due to these fins has to be taken into account when calculating the overall drag coefficient in each degree of freedom.
Firstly, the drag coefficient for the main body in surge, sway and heave directions can be estimated using the equation for the drag coefficient for simple streamlined ellipsoidal bodies at sub-critical Reynolds numbers, shown in equation (3.32).

$$C_D = 0.44(\frac{b}{a}) + 0.016(\frac{a}{b}) + 0.016\sqrt{(\frac{a}{b})} \tag{3.32}$$

Where a is the radius of the ellipsoid along the x axis and b is the radius of the ellipsoid along the y-z plane.
The drag force produced by the fins located on the body of the vehicle is estimated using the

standard drag equation and knowledge of the shape of the fins. The fins have been designed to be as close to NACA 0012 sections as possible. knowing the NACA section of these fins and the angle these fins make to the oncoming flow of fluid, allows the calculation of the drag force in surge direction produced form data tables of angle of attack versus drag coefficient. The drag force in heave is calculated simply from the planform area of the the fins and the drag coefficient of a flat plate. Combining the two methods described above an approximation for the rigid body drag can be deduced in the six degree of freedom.

The drag on a swimming fish is not as straight forward as using the rigid body drag previuosly illustrated, due to the complex interactions between the undulating fish body and the water. However, an attempt has been made to model the drag procuced by the moving tail by assuming the caudal fin is a wedge that has a surface area which is dependant on the angle the fin make with the oncoming water flow. The drag coefficient used for this wedge, representing the caudal fin, is 0.5. If the fin is at its maxumum amplitude then its surface ara is maximum and therefore increasing the drag force. On the other hand, if the fin is in line with the body, then the drag is reduced.

By making this assumption it can be seen that the drag force produced by the caudal fin is time varying. Actually it varies over one tail beat cycle, and, when viewed over several tail beat cycles the drag appears to oscillate about a steady value.

3.4 Tendon drive propulsion system

The aim of modelling the propulsion system is to allow for estimates of the control forces and momentsto be made using the input commands of the system.
These approximation of thrust are used in the dynamic section of the model.
In this section, the calculation of the control forces and moments for the tendon drive propulsion system will be explained.

As previously mentioned, the aim of modelling the propulsion system is to allow for estimates of the thrust and manoeuvering forces to be made using the inputs command of the system. For reason of simplicity the propulsion system model has been subdiveded into four sections, as shown in the flowchart presented in Figure 3.4, which will be analysed separately.

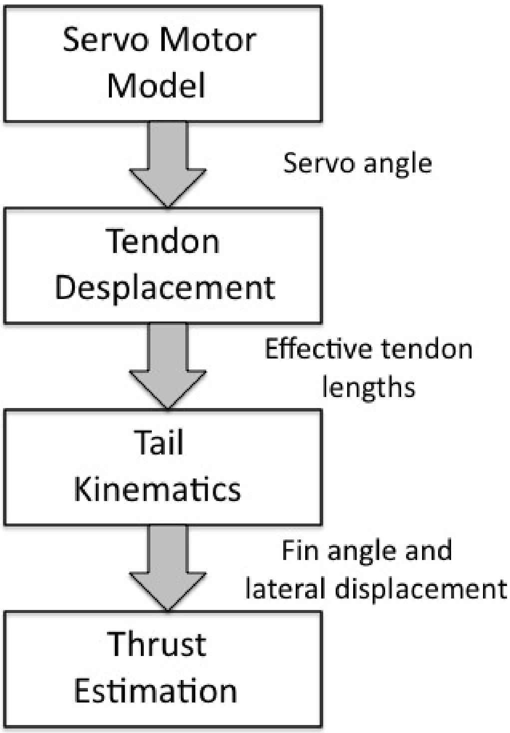

Figure 3.4: Flowchart of the tendon drive propulsion system.

As shown in the above flowchart, the input of the propulsion system is the desired tail beat frequency and the amplitude, which are passed to the servo motor model. This then causes the servo to move in the reciprocal manner to the servo motor parameters that will correspond to the desired tail commands. The servo motor output is the displacement of the servo motor arm, which is then used to elaborate the effective changes in the tendons length. These tendon displacements are used as input for the tail kinematics model, which relates the tendon lengths to the angular positions of each revolute joint in the tail. Knowing the the angular position of each of the ten revolute joints allows the calculation of the caudal fin tip displacement, together with the caudal fin angular displacement, namely the angle the caudal fin makes with the tail centre line. With these caudal fin parameters it is possible to estimate the thrust produced by the tendon drive tail.

3.4.1 Servo motor model

For the actuation of the tendon drive propulsion system, a Hitec HS-5645 Digital Servo motor is used. This motor operates by moving the output servo arm to an angular position which corresponds to the pulse width of the pulse width modulated signal (PWM) input signal.
The servo motor system is modelled as a DC motor with a reduction gearbox attached. In order to describe the dynamics of the motor, the standard electrical and mechanical equations for a DC motor are used, which are shown in equations (3.33) and (3.34).

$$L\frac{di}{dt} + Ri = V - K_e\dot{\theta} \tag{3.33}$$

$$J\ddot{\theta} + b\dot{\theta} = K_t - T_l \tag{3.34}$$

Where L is the inductance of the motor (H), i is the motor current (A), R is the motor resistance (ω), V is the applied voltage (V), K_e is the motor emf constant ($Vrad^{-1}s^{-1}$), θ is the servo motor arm angular displacement (rad), J is the inertia fo the motor shaft and load (Kgm^2), b is the viscous friction coefficient, K_t is the motor torque constant (NmA^{-1}), which is equal to the motor emf constant, and T_l is the load torque (Nm).

A proportional-integral-derivative controller (PID) is designed in order to control the position of the servo arm.
The design method used to elaborate the PID gains is the one used in the control law section, in the same section a brief description of the PID control algorithm is presented. The PID gains found are presented equation (3.35).

$$\begin{array}{rcl} K_p & = & 30 \\ K_d & = & 32 \\ K_i & = & 23 \end{array} \tag{3.35}$$

In Figure the simulated servo motor response to step changes of commands of ±30 degrees is presented.
The figure above allows to notice that the PID control algorithm designed to control the servo motor arm angular position is effective in allowing the servo arm to reach its commanded position with only slight overshoot and a reasonable rise time.

Commands are sent to the servo motor, which generates a reciprocal rotation motion of between ±45 degrees. The maximum frequency of this motion is limited to approximately 1 Hz, due to the mechanical limitations of the whole tendon drive system.

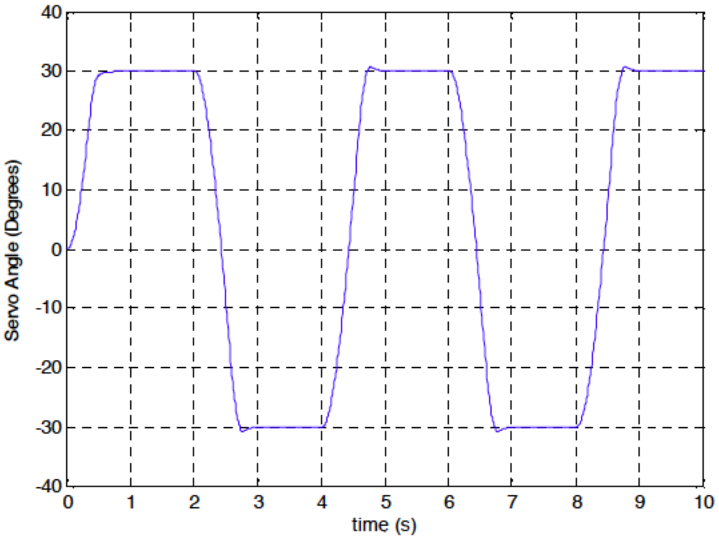

Figure 3.5: Simulated servo motor model response to step changes of ±30 degrees using the PID control algorithm.

3.4.2 Tendon displacements model

In order to determine the revolute joint variables for a particular servo motor angle, the relationship between the servo motor arm, tendons and joint assemblies has to be known.
Firstly, as mentioned in the previous servo motor section, the servo motor receives as input a PWM signal, which duty cycle corresponds to the desired output angle of the servo motor arm. The movement of the servo motor arm pulls on one of the tendons. This tendon is referred to as the active tendon, as it is this tendon which causes the deflection in the tail.
The other tendon, which is not being pulled, is assumed not to contribute to the motion at this instant. As the servo motor is mounted in the body section, the length of tendon wire within the tail assembly is reduced, this is referred to as the effective shortening of the tendon.

The relationship between the servo motor arm angular position and the effective shortening of the tendon length is calculated using the geometry of the internal mechanics of the tail and servo assembly. Calling β the servo arm angle and x_l and x_r the left and right tendons length respectively, their relationship is shown in equation (3.36) and (3.37).

$$x_l = \sqrt{(l_{arm}\cos\theta - z)^2 + (l_{servo} - l_{arm}\sin\beta)^2} - x_c \tag{3.36}$$

$$x_r = \sqrt{(l_{arm}\cos\theta - z)^2 + (l_{servo} + l_{arm}\sin\beta)^2} - x_c \tag{3.37}$$

Where the other parameters l_{arm}, l_{servo} and z represent the length of the servo arm, the distance from the motor shaft to the start of the tail assembly and the distance between the tendons at the start of the tail respectively.
The parametr θ represents the servo motor angular position, as in the servo motor model section, and the last parameter, x_c, is the length of the tendons when the tail is at its centre

position.

This overall change in the tendon length is distributed among the ten revolute joints. From experimentation with the prototype it has been apparent that this distribution is not equal. This behaviour is due to the fact that the joint angles towards the end of the tail fin are greater to those towards the body, because of the mechanics of the tail.
For this reason, the distribution of the change in the tendon length is assumed to be linearly increasing over the ten revolute joints.
A scheme of the plan view of one revolute joint from the tail assembly is shown in Figure 3.6. The joint angle of a revolute joint can be easily calculated from the corresponding change in length of the active tendon for that joint assembly using trigonometry, as shown in equation (3.38).

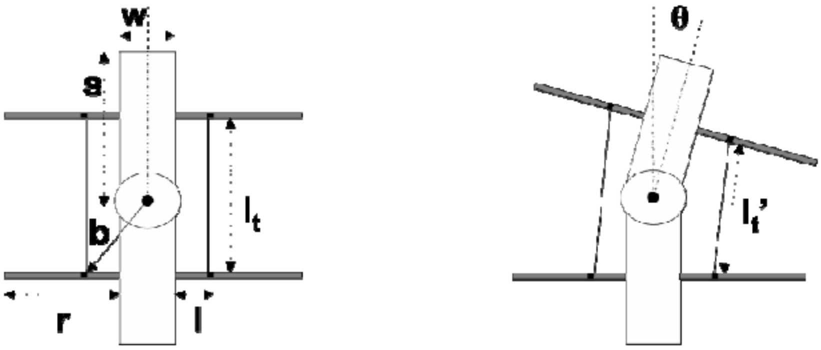

(a) Tendon lengths equal. (b) Right tendon shortened

Figure 3.6: Individual revolute joint assembly showing tendons and rib sections both for equal tendon lengths, in figure a, and different tendon lengths, in figure b.

$$\theta_x = -\left(180 - 2\sin^{-1}\left(\frac{l + \frac{w}{2}}{b}\right) - 2\sin^{-1}\frac{l_t'}{2b}\right) \tag{3.38}$$

Where θ_x is the is the angle for the joint number x, l is the distance of the tendon from the segment at the shortest point (m), w is the width of the segment (m), l_t and l_t' represent the lengths of the tendonat its centre position and when shortened respectively.

3.4.3 Tendon tail kinematics

The tail can be considered as a robot manipulator with ten revolute joints, due to its design. As such, the kinematic equations used to describe robot manipulators can be applied to describe the tendon drive tail.

The standard method used to model the forward kinematics of robot manipulators is the Denavit-Hartenberg representation (D-H), introduced by Jaques Denavit and Richard S. Hartenberg. This method involves assigning each joint a reference frame according to the following procedure set:

- z_i: the z_i axis is chosen to be coincident with the $i+1$ joint axis.
- x_i: the x_i axis is parallel to the common normal: $x_i = z_i \times z_{i-1}$. The direction of x_i is from z_{i-1} to z_i.
- y_i: the y_i axis is simply chosen to create a right frame $y_i = z_i \times x_i$.
- The origin of the (i) frame is at the intersection of x_i and z_1.
- The origin of the (0) frame is chosen to be coincident with the (1) frame.
- The origin of the last frame (n) is chosen to be coincident with the (n-1) frame, and the z_n axis has the direction of the last joint.

Having the frames for each revolute joint, allows the definition of the four Denavit-Hartenberg parameters as follows:

- The angle between the z_{i-1} and z_i axis is called twist of the link and it is referred to as α_i.
- The angle between the x_{i-1} and x_i axis is called rotation, and it is referred to as θ_i.
- The distance between the origin of the (i-1) frame and the x_i axis is called offset and it is referred to as d_i.
- The distance between the origin of the (i) frame and the z_{i-1} axis is called length of the link and it is referred to as a_i.

The joint-link representation for the ten segment tendon drive RoboSalmon tail is shown in Figure 3.7.

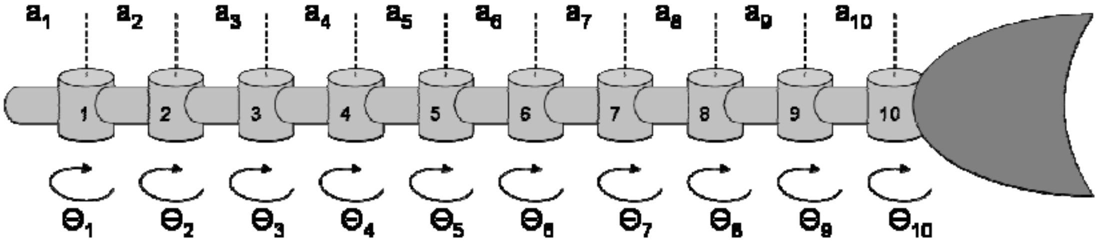

Figure 3.7: Joint and link D-H representation of the RoboSalmon tail assembly.

The parameters for all the joints are then assembled into a table referred to as the D-H parameter table.
The creation of the parameters table allows easy calculation of the T matrix for each revolute joint. The T matrix is referred to as the rototranslation matrix, and it is a combination of all the four possible movements, namely the rotation about the x, y and z axis together with a translation. Using the T matrix for each joint allows for transformation between successive joint reference frames.

Using the Denavit-Hartenberg notation, the position matrix $T_{i-1,i}$ between successive link assumes the standard structure shown in equation (3.39).

$$T_{i-1,i} = \left[\begin{array}{ccc|c} \cos\theta_i & -\sin\theta_i \cos\alpha_i & \sin\theta_i \cos\alpha_i & a_i \cos\theta_i \\ \sin\theta_i & \cos\theta_i \cos\alpha_i & -\cos\theta_i \sin\alpha_i & a_i \sin\theta_i \\ 0 & \sin\alpha_i & \cos\alpha_i & d_i \\ \hline 0 & 0 & 0 & 1 \end{array}\right] \tag{3.39}$$

The parameters included in the D-H parameter table are shown in Figure 3.8.

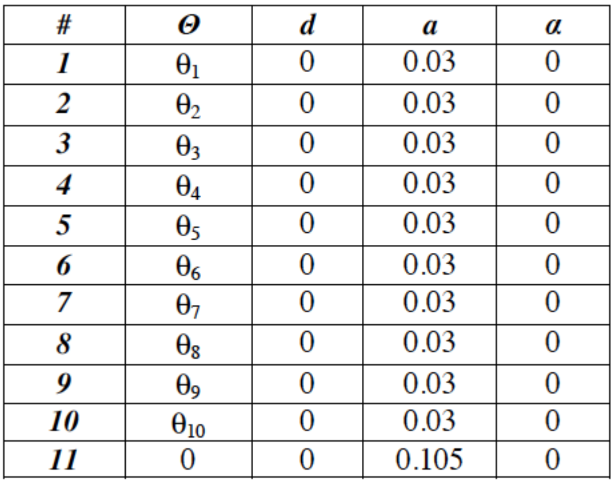

#	**Θ**	**d**	**a**	**α**
1	θ_1	0	0.03	0
2	θ_2	0	0.03	0
3	θ_3	0	0.03	0
4	θ_4	0	0.03	0
5	θ_5	0	0.03	0
6	θ_6	0	0.03	0
7	θ_7	0	0.03	0
8	θ_8	0	0.03	0
9	θ_9	0	0.03	0
10	θ_{10}	0	0.03	0
11	0	0	0.105	0

Figure 3.8: D-H parameters table representation of the RoboSalmon tail assembly.

By using the T matrices derived from the D-H parameters table transformation between the first segment frame (the one connected to the body) and the last joint (representing the caudal peduncle), it is possible to determine the position of each joint in the caudal peduncle reference frame.

For reason of simplicity, the rototranslation matrix $T_{i-1,i}$ between the (i-1) and the (i) links has been called A_i.
The process of transformation between the body and caudal peduncle is carried out as follows in equation (3.40).

$$T = T_{0,1}T_{1,2}T_{2,3}T_{3,4}T_{4,5}T_{5,6}T_{6,7}T_{7,8}T_{8,9}T_{9,10} = A_1A_2A_3A_4A_5A_6A_7A_8A_9A_{10} \tag{3.40}$$

In order to know the position of each joint in tail in the body frame, the transformation matrices can be calculated as shown below in equations from (3.41) to (3.50).

$$\text{frame 1 to body: } T = T_{0,1} = A_1 \tag{3.41}$$

$$\text{frame 2 to body: } T = T_{0,1}T_{1,2} = A_1A_2 \tag{3.42}$$

$$\text{frame 3 to body: } T = T_{0,1}T_{1,2}T_{2,3} = A_1A_2A_3 \tag{3.43}$$

$$\text{frame 4 to body: } T = T_{0,1}T_{1,2}T_{2,3}T_{3,4} = A_1A_2A_3A_4 \tag{3.44}$$

$$\text{frame 5 to body: } T = T_{0,1}T_{1,2}T_{2,3}T_{3,4}T_{4,5} = A_1A_2A_3A_4A_5 \tag{3.45}$$

$$\text{frame 6 to body: } T = T_{0,1}T_{1,2}T_{2,3}T_{3,4}T_{4,5}T_{5,6} = A_1A_2A_3A_4A_5A_6 \tag{3.46}$$

$$\text{frame 7 to body: } T = T_{0,1}T_{1,2}T_{2,3}T_{3,4}T_{4,5}T_{5,6}T_{6,7} = A_1A_2A_3A_4A_5A_6A_7 \tag{3.47}$$

$$\text{frame 8 to body: } T = T_{0,1}T_{1,2}T_{2,3}T_{3,4}T_{4,5}T_{5,6}T_{6,7}T_{7,8} = A_1A_2A_3A_4A_5A_6A_7A_8 \tag{3.48}$$

$$\text{frame 9 to body: } T = T_{0,1}T_{1,2}T_{2,3}T_{3,4}T_{4,5}T_{5,6}T_{6,7}T_{7,8}T_{8,9} = A_1A_2A_3A_4A_5A_6A_7A_8A_9 \tag{3.49}$$

$$\begin{aligned}\text{peduncle to body: } T &= T_{0,1}T_{1,2}T_{2,3}T_{3,4}T_{4,5}T_{5,6}T_{6,7}T_{7,8}T_{8,9}T_{9,10} \\ &= A_1A_2A_3A_4A_5A_6A_7A_8A_9A_{10}\end{aligned} \tag{3.50}$$

Using the above transformation matrices , the location of the origin of each joint frame in the body reference frame can be plotted in two dimensions from the x and y translational coordinates in each of the matrices.
This method also allows the lateral displacement of the caudal fin from the tail centre line to be calculated.

From the above discussion of the tail kinematic system, the overall kinematics of the tail can be computed knowing the input angle from the servo motor.
In Figure 3.9 the comparison between an ideal fish tail kinematics and the RoboSalmon tail kinematics is shown for one instant during a tail beat cycle.

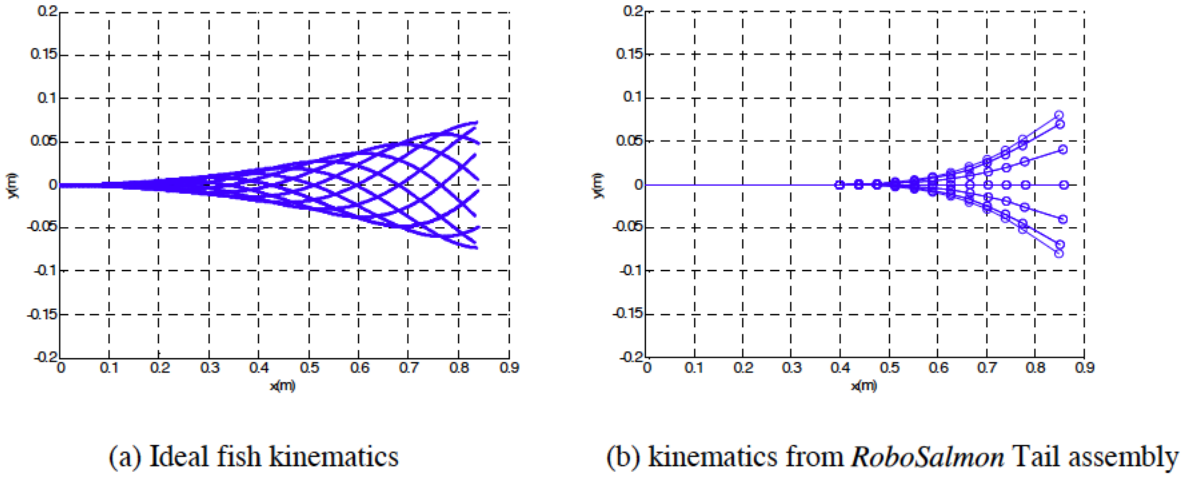

(a) Ideal fish kinematics

(b) kinematics from ***RoboSalmon*** **Tail assembly**

Figure 3.9: Comparison of an ideal tail kinematics (on the left, solid line) and the obtained tail kinematcs (on the right, circled line).

From the comparison presented in the above figure, the limitations of the RoboSalmon tail assembly are apparent. As it can be seen in the figure, although the position of the RoboSalmon tail tip is fairly close to the ideal one, the shape of the RoboSalmon tail during the tail beat cycle differs from the ideal situation. Another thing to notice is that the tail tip amplitude and the angle of the tail fin are in phase, whereas, from observations of real fish, they appear to be

90 degrees out of phase.
These differences between the RoboSalmon tail kinematics and the ideal one are unavoidable, due to the mechanical design and actuation method of the tail assembly implemented.
However, the simplicity and low cost nature of this approach should compensate for the difference in the kinematics and any adverse effect this may have on the performance of the vehicle.

3.4.4 Thrust estimation

For the tendon drive tail propulsion system implemented on the RoboSalmon, a method of estimating the thrust produced by the tail motion was required.
From surveys of the available literature on fish propulsion, there does not appear to be an exact and definitive theoretical method for easily calculating the thrust produced by the undulating tail and fin movements of fish swimming.
Some sources suggest that solving the Navier-Stokes equation gives an accurate prediction of the thrust, however, this method requires the use of computational fluid dynamics and would take a substantial amount of time to solve due to its complexity.

From the literature surveyed there appears to be two main methods for estimating the thrust force produced by an undulating tail.
The first method is referred to as the vortex theory, while the second method is the elongated body theory and its derivatives. As it will be seen, both methods have their advantages and disadvantages.

The vortex method estimates the thrust produced by analysing the vortices left in the wake as the fish swims. This method uses parameters of the vortex wake, such as circulation, size, positioning and number of vortices in the wake.
However, this method is of limited use for the modelling and simulation of the propulsion system implemented on the RoboSalmon. At present there does not appear to be a simple method of predicting the formation of the vortices and vortex parameters from the movements of the fish without the use of complex computational fluid dynamics methods, or direct observation and measurement of the vortices produced while swimming. Using this method in runtime while the vehicle is in operation would be difficult due to the speed at which the vortex information could be obtained and processed.

The other method that can be used to estimate the thrust produced by the tail propulsion system is the Lighthill's *large amplitude elongated body theory.* The main idea of this theory lies in the transfer of momentum between fish and water, and in the assumption that the majority of this transfer happens at the caudal fin. Therefore, only the heave and pitch motions of the caudal fin are involved in the estimation of the thrust.
In the context of this theory, heave motion is the side to side displacement of the caudal fin and pitch is the angle of the caudal fin to the centreline of the fish. These two parameters are different from the standard heave and pitch used to describe marine vessels. This is due to the initial investigations into propulsion using a species that had a horizontal caudal fin, and so heave and pitch were used to describe the motion. However, the same theory applies to both horizontal and vertical fin orientation.
Both heave and pitch are assumed to be sinusoidal functions. From observations of real fish

and simulations, it has been noticed that the heave and pitch are approximately 90 degrees out of phase from one another.
The equation used for the thrust estimate is shown in equation (3.51).

$$F_t = m_v w W - \frac{1}{2} w^2 m_v \tag{3.51}$$

Where F_t is the surge thrust force (N), m_v is the virtual mass per unit length (Kg), w is the perpendicular velocity of the tail (ms^{-1}) an W is the lateral velocity of the tail tip (ms^{-1}).
Figure 3.10 shows plots of the thrust and drag force in surge for a tail beat frequency of 1 HZ, starting initially from rest.

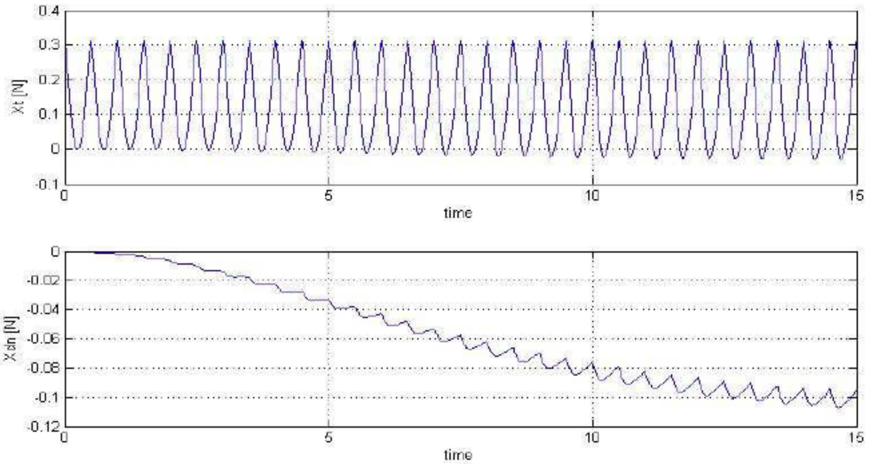

Figure 3.10: Comparison of an ideal tail kinematics (on the left, solid line) and the obtained tail kinematcs (on the right, circled line).

Although the thrust force varies dramatically over one tail beat cycle, when the instantaneous force is averaged for steady swimming, it coincides with the drag force produced.

3.5 Tendon tail manoeuvring

In order for the RoboSalmon vehicle to manoeuvre, the centreline of the tail oscillation can be altered.

For forward propulsion the tail offset is in line with the body of the RoboSalmon. On the contrary, for turning manouevering, the position of the tail oscillation centreline has to be altered (by angle $\Delta\theta$). In this case it is assumed that a component of the thrust force acts in sway and thus yaw. This is illustrated in Figure 3.11.

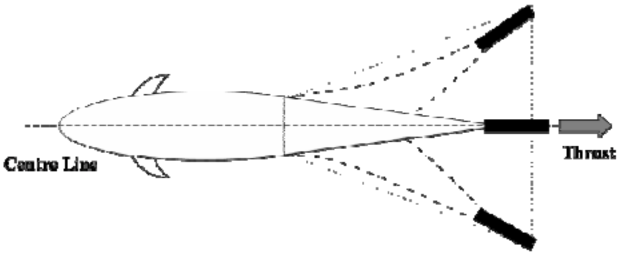

(a) Thrust force when tail beat centred (Forward Motion)

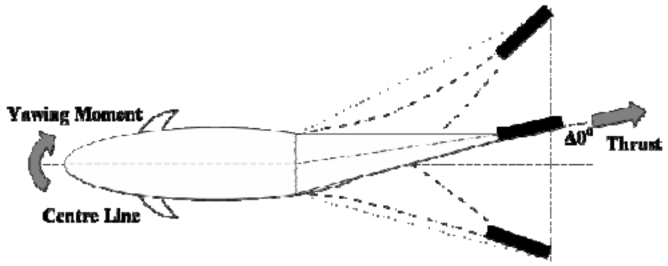

(b) Thrust force when tail beat offset (Turning Motion)

Figure 3.11: Diagram of tail sweep and thrust force for forward propulsion (on the top) and turning propulsion (on the bottom).

With the tail oscillating with the centreline offset, the force components in surge, sway and yaw are calculated using trigonometric relationship. This allows for the model to represent the manoeuvring forces generated by the tendon drive tail.

3.6 Recoil motion

From experimentation with the RoboSalmon biomimetic vehicle, one aspect of the swimming that has become apparent is the level of the recoil motion generated by the tendon drive tail. The recoil motion occurs when the tail moves one way and the rest of the vehicle's body recoils in reaction. This behaviour causes the vehicle to exhibit unwanted roll, pitch and yaw motions. Also real fishes experience recoil motion, but it is not as severe as the recoil that can be noticed in certain biomimetic vehicles, like the RoboSalmon. This is because the real fishes have a number of metohods of dealing with recoil motion, such as having a flat body profile, which increases lateral drag. Another way the fishes use to deal with the recoil motion is in the undulatory motion of the body and the tail during swimming, which, at any one istant, there are parts of the body and of the tail at both side of the fishes centreline and, as the undulatory motion is cyclical, the lateral forces causing the recoil are thought to cancel out.

From the first simulations with the RoboSalmon vehicle it has become apparent that the recoil motion is most evident in yaw and roll. Therefore, the model has to take this recoil motion into account in its representation of these particular degree of freedom.

In roll, the recoil motion is assumed to be caused by a combination of two main factors.
The first factor is the moment created by the mass of the tail as it moves a certain distance away from a pivot point, the vehicle centreline, as shown in Figure 3.12.

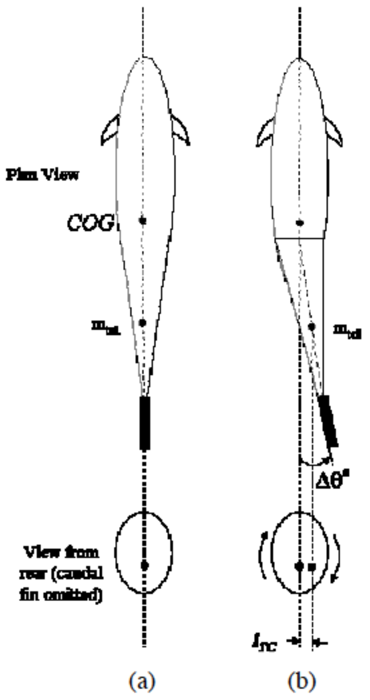

Figure 3.12: Representation of the recoil motion in roll. On the left figure (a) the tendon tail is in line with the body of the vehicle. On the right figure (b) the tendon tail has an offset of $\Delta\theta$ degrees.

In the figure above, m_{tail} is in kg and its position indicates the approximate centre of mass of the tail and l_{TC} represents the distance, on the y axis of the body-fixed frame, between the centreline of the RoboSalmon vehicle and the centre of mass of the tail in meters.
During the motion of the vehicle, the oscillation of the tail moves the centre of mass of the tail from the centreline, thus generating a moment about the x axis, with magnitude equal to the weight of the tail multiplied by the l_{TC} parameter.
The second factor contributing to the roll recoil is the moment caused by the drag force acting on the caudal fin as it moves through the water. As the caudal fin is mounted above the centreline of the vehicle by a distance called l_{cf}, the drag force acting on the fin will create a moment in the roll axis.

The recoil motion in yaw is slightly more difficult to represent within the mathematical model. From observations of the RoboSalmon vehicle swimming in a straight line, the recoil in yaw presents itself as a rotational motion of the body as the tendon drive tail moves away from its centreline. The rotational motion of the body is in the opposite direction to the motion of the tail if the vehicle centre of gravity (COG) is taken as the pivot point (as the tail moves clockwise, the body recoils anti-clockwise).
This effect is represented within the model in terms of the moment produced by the lateral drag force of the fin as it moves in the tendon tail actuation system. If the tendon drive RoboSalmon vehicle is actuated out of the water, on a bench say, no recoil is observed, as the drag force on the fin due to the air resistance is significantly less than in water and also the friction between the vehicle and the bench prevents the body from moving in reaction to the tail moving. However, when the system is actuated in the water environment the hydrodynamic drag due to the movements of caudal fin is significantly greater and so will produce a moment about the COG of the vehicle acting in the yaw axis.
Within the model, this beahaviour is represented by using the drag force produced by the caudal fin to create a recoil torque, called τ_{RECOIL}, as it moves to create a moment about the vehicle COG, which is assumed to be located half a body length in front of the caudal fin. This is presented in Figure 3.13.

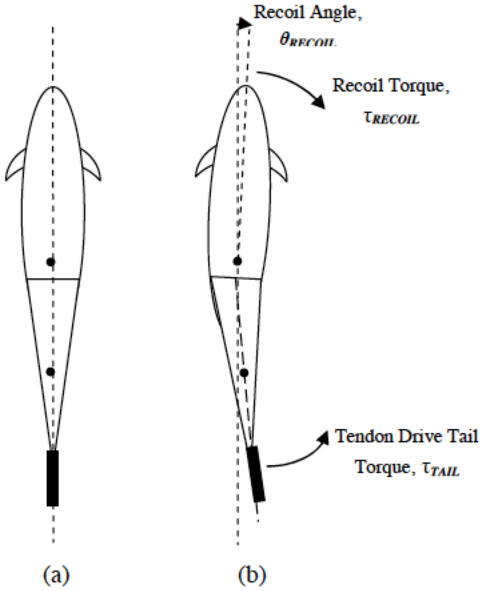

Figure 3.13: Representation of the recoil motion in yaw. On the left figure (a) the tendon tail is in line with the body of the vehicle. On the right figure (b) the tendon tail has an offset of $\Delta\theta$ degrees.

3.7 Input forces and moments

The overall control forces and moments due to the tendon drive tail are shown in equations from (3.52) to (3.55).

$$X_t = F_t \cos(\theta) \tag{3.52}$$

$$Y_t = F_t \sin(\theta) \tag{3.53}$$

$$K_t = 0.5m_{tail} \cdot g \cdot l_{TC} - l_{cf} D_{fin} \tag{3.54}$$

$$N_t = Y_t \frac{l}{2} + \tau_{RECOIL} \tag{3.55}$$

Where the surge force X_t is calculated from the estimate thrust produced by the tail motion F_t multiplied by the cosine of the tail centreline, to take into account the reduction in thrust when manoeuvring is requred. The sway force Y_t is represented in a similar way to the surge force, except it is multiplied by a sine of the tail centreline to produce a manoeuvring force with the tail centreline offset. The roll term K_t is produced by the recoil motion as shown in figure 3.12. Finally, the yaw term N_t consists of a turning component generated by the moment arm produced by the sway term multiplied by half the body length and an additional term to represent the recoil motion, as discussed in the previous section.

3.8 RoboSalmon state space equations

The standard equations of motion for modelling the dynamics of the RoboSalmon vehicle, shown previously in equation (3.10) can be rearranged into state space form as shown in equation (3.56).

$$\dot{v} = M^{-1}(\tau - C(v)v + D(v)v + g(\eta)) \tag{3.56}$$

The complete set of state space equations for each degree of freedom is shown in equations from (3.57) to (3.62).

$$\text{Surge :} \qquad \dot{u} = \frac{mvr - mwq + X_t + X_D - Y_{\dot{v}}vr + Z_{\dot{w}}wq}{m - X_{\dot{u}}} \tag{3.57}$$

$$\text{Sway :} \qquad \dot{v} = \frac{-mur + mwp + Y_t + Y_D + X_{\dot{u}}ur - Z_{\dot{w}}wp}{m - Y_{\dot{v}}} \tag{3.58}$$

$$\text{Heave :} \qquad \dot{w} = \frac{-muq + mvp + Z_D - X_{\dot{u}}uq + Y_{\dot{v}}vp}{m - Z_{\dot{w}}} \tag{3.59}$$

$$\text{Roll :} \qquad \dot{p} = \frac{K_t + K_D - J_z qr + J_y qr - Y_{\dot{v}}vw + Z_{\dot{w}}wv - M_{\dot{q}}qr + N_{\dot{r}}qr}{J_x - K_{\dot{p}}} \tag{3.60}$$

$$\text{Pitch :} \qquad \dot{q} = \frac{M_t + M_D - J_x rp + J_z rp + X_{\dot{u}}wu - Z_{\dot{w}}wu + K_{\dot{p}}rp - N_{\dot{r}}rp}{J_y - M_{\dot{q}}} \tag{3.61}$$

$$\text{Yaw :} \qquad \dot{r} = \frac{N_t + N_D - J_y pq + J_x pq - X_{\dot{u}}uv + Y_{\dot{v}}uv - K_{\dot{p}}pq + M_{\dot{q}}pq}{J_z - N_{\dot{r}}} \tag{3.62}$$

The kinematic relationships used to translate the linear and angular velocities in the body-fixed frame to linear and angular velocities in the earth-fixed frame, shown in equations (3.5) and (3.6), can be used to calculate the linear and angular velocities in the earth-fixed frame, as illustrated in equations from (3.63) to (3.68).

$$\dot{x} = u\cos\psi\cos\theta + v(\cos\psi\sin\theta\sin\phi - \sin\psi\cos\phi) + w(\sin\psi\sin\phi + \cos\psi\cos\phi\sin\theta) \tag{3.63}$$

$$\dot{y} = u\sin\psi\sin\phi + v(\cos\psi\cos\phi + \sin\phi\sin\psi\sin\theta) + w(\sin\theta\sin\psi\cos\phi - \cos\psi\sin\phi) \tag{3.64}$$

$$\dot{z} = -u\sin\theta + v\cos\theta\sin\phi + w\cos\theta\cos\phi \tag{3.65}$$

$$\dot{\theta} = p + q\sin\phi\tan\theta + r\cos\phi\tan\theta \tag{3.66}$$

$$\dot{\phi} = q\cos\phi - r\sin\phi \tag{3.67}$$

$$\dot{\psi} = q\frac{\sin\phi}{\cos\theta} + r\frac{\cos\phi}{\cos\theta} \tag{3.68}$$

Where θ can't assume the values ±90 degrees in order to avoid singularities.
The constants used within the mathematical model of the RoboSalmon vehicle are given in Appendix.

Deriving the linear and angular velocities in the earth-fixed frame allows the calculation of the position and orientation of the RoboSalmon vehicle in the same frame. These informations are necessary in order to have a reliable feedbak when implementing the vehicle's control and guidance system, as it will be seen in the next sections.

Chapter 4

Heading Control

The aim of the project is the design of a suitable control and guidance system for the RoboSalmon biomimetic vehicle.
In order to accomplish this aim, it is necessary to design the steering control system, and then to proceed with the design of the guidance system.
The heading control system is responsable of controlling the steering system, allowing the RoboSalmon to control the yaw angle. As stated in the prevoius chapter, in order to make the vehicle turning it is necessary to control the tail offset.

In the following sections two different control systems for the RoboSalmon biomimetic vehicle are designed and implemented.
The first steering control system designed and implemented is the PID control algorythm. This choice has been made since the PID algorythm is one of the easier and common control system in literature.
Then the sliding mode control system for the heading control of the RoboSalmon is designed and implemented, due to its advanteges in the control of highly non linear and coupled dynamics systems.
In the final section, a comparison between the two control algorithm is presented. The set of simulation trials illustrated in this section have allowed the performance and characteristics of the two RoboSalmon heading controls implemented to be determined for forward motion and turning manoeuvring.

Before proceeding with the design of the steering control system, it is necessary to notice that, due to the resctrictions of the experimental hardware and size of the test pool avaliable, the results obtained only allow for validation of the model in four degrees of freedom, surge, sway, roll and yaw. For this reason, the dynamics of the RoboSalmon involved in the implementation of the heading control system does not take into account the remaining two degrees of freedom, heave and pitch.
These means that the depth of the biomimetic vehicle, namely the position on the z axis, is assumed to be constant.

4.1 PID heading control

The first control system developed for the RoboSalmon heading control is the PID control algorythm. This choice has been made since the PID controller is one of the most common control system, thanks to its implementation simplicity, and it has been deeply analysed in literature.

In order to design the steering control system, the dynamics equations of the RoboSalmon, derived in the previous chapter, have to be analysed. As it can be seen in equations from (3.57) to (3.62), the dynamics of the RoboSalmon is coupled and highly non-linear in each degree of freedom.

Therefore, in order to design the PID controller for the heading of the vehicle, namely the yaw angle position, a linearization of the system is necessary.

The two equations of the dynamics and kinematic directly involved in the yaw angle position and velocity estimation are presented in equations (4.1) and (4.2)

$$\dot{r} = \frac{N_t + N_D - J_y pq + J_x pq - X_{\dot{u}} uv + Y_{\dot{v}} uv - K_{\dot{p}} pq + M_{\dot{q}} pq}{J_z - N_{\dot{r}}} \tag{4.1}$$

$$\dot{\psi} = q\frac{\sin\phi}{\cos\theta} + r\frac{\cos\phi}{\cos\theta} \tag{4.2}$$

Only the yaw dynamics and kinematics are taken into account in the previous linearization, since the dynamics of the other degrees of freedom is not directly involved in the yaw angle motion. Therefore, the varibles not directly involved in the steering dynamics, for small reference heading, can be considered to be constant.

For simplicity reason, the sway dynamics is not taken into account.

First of all it's known that the pitch angle θ is always zero, since, for the previously mentioned reasons, the depth of the RoboSalmon is assumed to be constant.

For small yaw angle desplacement ψ, also the roll ϕ angular position can be assumed to be zero, or at least the oscillation around zero, caused by the recoil motion, can be assumed to have zero mean. Hence, the yaw position dynamics equation, presented in equation (4.2), can be written as shown in equation (4.3)

$$\dot{\psi} = r \tag{4.3}$$

Before proceeding with the linearization, it is necessary to analyse every term of the yaw velocity dynamics equation (4.1). This can be done using the information presented in the mathematical model chapter.

The equation of the thrust component in yaw, N_t, is shown in equation (4.4).

$$N_t = F_t l/2 \sin\alpha - \tau \tag{4.4}$$

Where F_t represents the thrust force, l is the body length of the RoboSalmon and τ is the recoil motion caused by the tendon drive tail propulsion system. The tail centreline angle has been called α, contrary to the notation used in the previous chapter.

It can be seen that N_t depends on the sine of the offset of the tail α, which is the control input. Again, for small heading, also the control input is going to have small values, hence the sine of the control input can be simplifyed with the control input α.

The drag component in yaw, N_D, can be written as shown in equation (4.5).

$$N_D = C_D abs(r) r \tag{4.5}$$

Where the drag coefficient term C_D depends on the ellipsoidal shape of the RoboSalmon, as shown in equation (3.32). For small reference input α, also the yaw velocity r is small, therefore the drag component in yaw can be rounded to zero.
The yaw dynamics depends on the surge and sway velocities, which are assumed to be constant for small reference heading. Therefore, the thrust component generated by the recoil motion τ and the surge and sway velocites are grouped in a term called C_τ.
Finally, the yaw dynamics and kinematic equations can be linearized as shown in the system in equation (4.6).

$$\begin{cases} \dot{r} &= \frac{F_t \alpha l/2 - C_\tau}{J_z - N_{\dot{r}}} \\ \dot{\psi} &= r \end{cases} \tag{4.6}$$

The term C_τ, containing the recoil thrust component and the terms depending on the surge and sway velocities, is supposed to be constant. Therefore, the term $C_\tau/(J_z - N_{\dot{r}})$ is assumed to be a constant disturbance in the linear system.
Using the Laplace transformation, it can be seen that the transfer function $P(s)$ between the tail offset α and the heading of the fish ψ, in the earth-fixed frame, is a double integrator, as it can be seen in equation (4.7).

$$P(s) = \frac{\psi(s)}{\alpha(s)} = \frac{F_T l/2}{J_z - N_{\dot{r}}} \frac{1}{s^2} \tag{4.7}$$

Since the constant disturbance $C_\tau/(J_z - N_{\dot{r}})$ has a high value, compared to the values involved in the linear system, in the design of the PID controller the constant disturbance isn't taken in account.
The PID control algorythm has the well known transfer function $C(s)$, shown in equation (4.8).

$$C(s) = K_p + \frac{K_i}{s} + \frac{sK_d}{1 + T_l s} \tag{4.8}$$

Where K_p, K_i and K_d are the gains of the proportional term, the integral term and the derivative term respectively, and T_l is the high frequency pole gain. The high frequency pole has been added in order to make achievable the derivative term.
The usual feedback scheme of the PID control system for the linearized system can be seen in the following Figure 4.1.

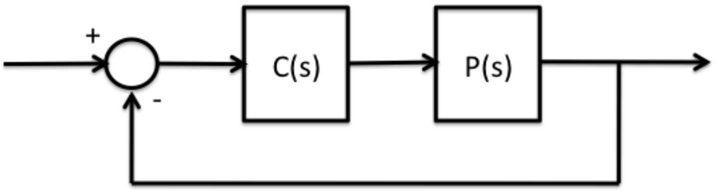

Figure 4.1: Control scheme.

The PID controller $C(s)$ can be divided in three action, the proportional, the derivative and the integral, which are associated with the previously mentioned gains. The block structure of the PID can be seen in the following Figure 4.2.

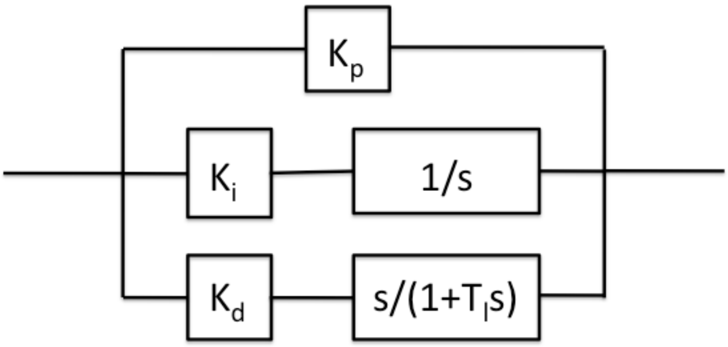

Figure 4.2: PID controller structure.

In order to obtain the gains of the PID controller associated with the stability of the linearized system, the Ziegler-Nichols method has been used. The gains obtained are written in equation (4.9).

$$\begin{aligned} K_p &= 0.65 \\ K_i &= 0.2889 \\ K_d &= 0.3656 \end{aligned} \tag{4.9}$$

Since the Ziegler-Nichols tuning method yields an aggressive gain and overshoot, a further manual tuning has been needed.
In order to tune the PID gains, the following rules can be applied, while looking at the response of the controlled system to a step reference input:

- **Proportional control:** Larger values of the proportional gain mean a decrease in the rise time and in the steady-state error. However it leads to an increase in the overshoot
- **Derivative control:** Larger values of the derivative gain lead to an increase in the stability of the system, still it leads to the signal noise amplification.
- **Integral control:** Larger values of the integral gain imply steady state errors are eliminated more quickly. On the other hand larger values lead to a larger overshoot and to a decrease in the stability of the system.

The final values of the PID gains, which guarantee accetable performance of the controlled linear system, are shown in equation (4.10).

$$\begin{aligned} K_p &= 1.15 \\ K_i &= 0.05 \\ K_d &= 0.95 \end{aligned} \tag{4.10}$$

The PID controller designed for the linear system has been implemented in the whole RoboSalmon system. Even if the RoboSalmon dynamics is coupled and highly non-linear, the PID control designed, has proved to guarantee accetable performances.

In the last section of the chapter, simulations for forward motion and turning manoeuvring of the RoboSalmon using the PID heading control will be presented, in comparison with the simulations obtained when the sliding mode steering control is implemented, which is going to be analysed in the following section.

As stated before, the heading control is achieved controlling the tail centreline. It can be seen that, for positive offset, the heading of the fish is negative, hence all the PID gains must be negative.

4.2 Sliding mode control

4.2.1 Introduction

During the last three decades, since the publication of the survey paper in the IEEE Transactions on Automatic Control in 1977, significant interest on variable structure systems (VSS) and sliding mode control (SMC) has been generated in the control research community worldwide.
One of the most intriguing aspects of sliding mode is the discontinuous nature of the control action whose primary function of each of the feedback channels is to switch between two distinctively different system structures (or components) such that a new type of system motion, called sliding mode, exists in a manifold. This peculiar system characteristic is claimed to result in superb system performance which includes insensitivity to parameter variations, and complete rejection of disturbances.
The reportedly superb system behavior of VSS and sliding mode control naturally invites criticism and scepticism from within the research community, and from practicing control engineers alike. The sliding mode control research community has risen to respond to some of these critical challenges, while at the same time, contributed to the confusions about the robustness of sliding mode control by offering incomplete analyzes, and design fixes for the so-called chattering phenomenon.
Many analytical design methods were proposed to reduce the effects of chattering, for it remains to be the only obstacle for sliding mode to become one of the most significant discoveries in modern control theory; and its potential seemingly limited by the imaginations of the control researchers.

Sliding mode is originally conceived as system motion for dynamic systems whose essential open-loop behavior can be modeled adequately with ordinary differential equations.
The discontinuous control action, which is often referred to as variable structure control (VSC), is also defined in the continuous-time domain. The resulting feedback system, the so-called VSS, is also defined in the continuous-time domain, and it is governed by ordinary differential equations with discontinuous right-hand sides. The manifold of the state-space of the system on which sliding mode occurs is the sliding mode manifold, or simply, sliding manifold.
For control engineers, the simplest, but vividly perceptible example is a double integrator plant, subject to time optimal control action. Due to imperfections in the implementations of the switching curve, which is derived from the Pontryagin maximum principle, sliding mode may occur. Sliding mode was studied in conjunction with relay control for double integrator plants, a problem motivated by the design of attitude control systems of missiles with jet thrusters in the 1950's.
The chattering phenomenon is generally perceived as motion which oscillates about the sliding manifold. There are two possible mechanisms which produce such a motion. First, in the absence of switching nonidealities such as delays, i.e., the switching device is switching ideally at an infinite frequency, the presence of parasitic dynamics in series with the plant causes a small amplitude high-frequency oscillation to appear in the neighborhood of the sliding manifold. These parasitic dynamics represent the fast actuator and sensor dynamics which, according to control engineering practice, are often neglected in the open-loop model used for control design if the associated poles are well damped, and outside the desired bandwidth of the feedback

control system. Generally, the motion of the real system is close to that of an ideal system in which the parasitic dynamics are neglected, and the difference between the ideal and the real motion, which is on the order of the neglected time constants, decays rapidly. The mathematical basis for the analysis of dynamic systems with fast and slow motion is the theory of singularly perturbed differential equations, and its extensions to control theory have been developed and applied in practice. However, the theory is not applicable for VSS since they are governed by differential equations with discontinuous right hand sides. The interactions between the parasitic dynamics and VSC generate a nondecaying oscillatory component of finite amplitude and frequency, and this is generically referred to as chattering.

Second, the switching nonidealities alone can cause such high-frequency oscillations. We shall focus only on the delay type of switching nonidealities since it is most relevant to any electronic implementation of the switching device, including both analog and digital circuits, and microprocessor code executions. Since the cause of the resulting chattering phenomenon is due to time delays, discrete-time control design techniques, such as the design of an extrapolator can be applied to mitigate the switching delays. These design approaches are perhaps more familiar to control engineers.

In the next section the design of the sliding mode control for the RoboSalmon system will be presented.

4.2.2 Sliding mode steering control system

In this section, the sliding mode for the control of the RoboSalmon's heading is presented. The sliding mode control implementation needs the separating of the system into noninteracting (or lightly interacting) subsystem. In this case the key motion equations for the separate function of steering control has been grouped together.

The steering system will be responsable for control of the heading errors.

The speed control and the diving control systems are not going to be analysed in this paper.

With the single heading control active, the subsystem can be treated as a single input, multistate system with its own sliding surface defintion

$$\sigma(t) = s\tilde{x}(t) \tag{4.11}$$

where $\tilde{x}(t)$ represent the error of the states involved in the heading control, and s is the coefficient matrix, on which depends the closed-loop response of the controlled system.

The states involved in the steering control system are the yaw angle position $\psi(t)$, the yaw angle velocity $r(t)$ and the sway linear velocity $v(t)$. Therefore the dynamics of the three states can be collected in the following system (4.12).

$$\begin{cases} \dot{v} &= \frac{-mur+mwp+Y_t+Y_D+X_{\dot{u}}ur+Z_{\dot{w}}wp}{m-Y_{\dot{v}}} \\ \dot{r} &= \frac{N_t+N_D-J_ypq+J_xpq-X_{\dot{u}}uv+Y_{\dot{v}}uv-K_{\dot{p}}pq+M_{\dot{q}}pq}{J_z-N_{\dot{r}}} \\ \dot{\psi} &= q\frac{\sin\phi}{\cos\theta}+r\frac{\cos\phi}{\cos\theta} \end{cases} \tag{4.12}$$

The design procedure using sliding mode methods is to properly select surfaces yielding stable closed-loop error dynamics.

Global asymptotic stability of the sliding surface dynamics is guaranteed through consideration of $\sigma(t)$ in terms of a Lyapunov function $V(\sigma(t))$, yielding

$$V(\sigma(t)) = 0.5\sigma'(t) * \sigma(t)$$

Global asymptitic stability of $\sigma(t)$ is assured if

$$\frac{dV(\sigma(t))}{dt} = \dot{\sigma}(t)\sigma(t) < 0 \qquad \forall t > 0$$

Defining the positive function $\eta(t)$ then global asymptotic stability for the dynamic of $\sigma(t)$ will be given by

$$\dot{\sigma}(t) = -\eta sgn(\sigma(t)/\phi) \tag{4.13}$$

In fact, it is better to use a continuous function to define ”practical” sliding surface dynamics using a tanh function, as in

$$\dot{\sigma}(t) = -\eta \tanh(\sigma(t)/\phi) \tag{4.14}$$

The equation (4.14) means that, if η is large enough, then the system response will be governed by the response of the $\sigma(t)$ and by the choice of the sliding surface parameters.
ϕ is the sliding surface boundary layer parameters, used to retain continuity of control as motion trajectories cross the sliding surface and prevent chattering.
It remains to compute the control law to provide the desired $\sigma(t)$ dynamic and select s so that stable dynamics of $\sigma(t)$ results in stability of the tracking errors.
In order to design the sliding mode control system, the system (4.12) have to be linearize. Following the same linearization scheme introduced in the PID controller section, the linearized system will be

$$\begin{bmatrix} \dot{v} \\ \dot{r} \\ \dot{\psi} \end{bmatrix} = \begin{bmatrix} 0 & \frac{(X_{dotu}-m)\overline{u}}{m-Y_{\dot{v}}} & 0 \\ \frac{(Y_{\dot{v}}-X_{dotu})\overline{u}}{J_z-N_{\dot{r}}} & 0 & 0 \\ 0 & 1 & 0 \end{bmatrix} \begin{bmatrix} v \\ r \\ \psi \end{bmatrix} + \begin{bmatrix} \overline{F}_t \\ \overline{F}_t l/2 \\ 0 \end{bmatrix} \alpha \tag{4.15}$$

Where $\overline{u}$ is the mean of the surge velocity for small reference input, $\overline{F}_t$ is the mean of the thrust generated by the tendon drive tail motion and α is the control input, namely the tail centreline. Tha matrix of the states coefficient in the linearize system will be called A, likewise the vector of the input in the linearize system will be called b.
The matrix A and the vector b, with numerical values are

$$A = \begin{bmatrix} 0 & -0.0748 & 0 \\ 1.6479 & 0 & 0 \\ 0 & 1 & 0 \end{bmatrix}, b = \begin{bmatrix} 1.5319 \\ 0.6511 \\ 0 \end{bmatrix}$$

It can be seen that the pair (A, b) is controllable, therefore the sliding surface coefficients are elements of the left eigenvector of the closed-loop dynamic matrix A_c corresponding to a pole at the origin

$$s'[A_c] = 0 \tag{4.16}$$

Where the matrix A_c is given by $A_c = [A - bk']$.
$k' = [0.625, 0.1325, 0]$ is the closed-loop vector that places the closed-loop poles of the linearized system (4.15) at $[\lambda_1, \lambda_2, \lambda_3] = [0, -0.35, -0.53]$, selected for performance.

The sliding mode coefficients are $s' = [-1.13693, 0.52975, 0.1]$.
Hence the sliding surface has the following expression shown in equation (4.17).

$$\sigma(t) = -1.13693\tilde{v}(t) + 0.52975\tilde{r}(t) + 0.1\tilde{\psi}(t) \tag{4.17}$$

The resulting sliding control law $\delta(t)$ becomes

$$\delta(t) = -k'x(t) - [s'b]^{-1}\eta \tanh(s(3)\sigma(t)/\phi) \tag{4.18}$$

Where the vector $x(t) = [v(t), r(t), \psi(t)]$. Using the numerical values and considering $\tilde{v}$ and $\tilde{r}$ to be zero since it is not our goal to control the yaw velocity, results in the control law shown in equation (4.19).

$$\delta(t) = -0.625v(t) + 0.1325r(t) + 1.0739 \tanh(\widetilde{\psi(t)}); \tag{4.19}$$

The block structure of the sliding mode control obtained can be seen in Figure 4.3.

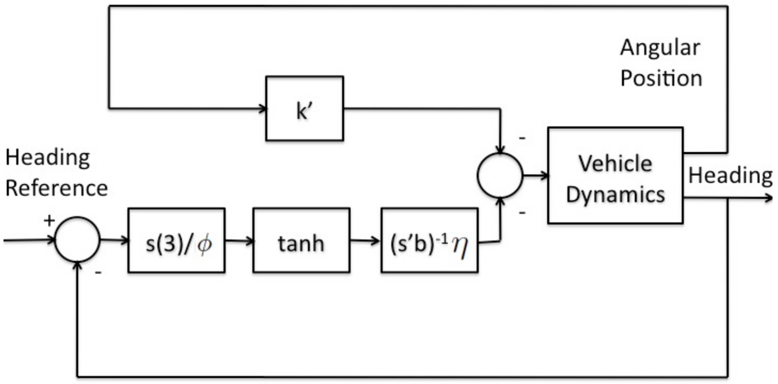

Figure 4.3: Sliding mode control block structure.

Where η and ϕ have already been substituted with their numerical values, as described in the following paragraph.
Notice that, in the above equation (4.19), the heading error term $\tilde{\psi}$ is only included in the nonlinear switching term, while the linear feedback of $v(t)$ and $r(t)$ act only to stabilize the sway and the yaw dynamics.
The choice of the switching gain η and the "boundary layer thickness" ϕ is selected to eliminate control chattering. So long as η is chosen to be "large enough" to overcome the destabilizing effects of any disturbance mismatch, bounded stability of the error is assured even though asymptotic stability is only approached as ϕ tends to zero. In this case $\eta = 1.5$ is selected so that $\eta > ||s||$ and $\phi = 0.1$.
Likewise the PID controller, also for the sliding mode control it's necessary to use the control law $-\delta(t)$, since the offset of the tail has the opposite sign of the yaw angle controlled.

4.3 Comparisons

In this section, a comparison between the two control algorythms has been made.
In order to analyse the behaviour of the two different control systems designed in the prevoius sections, three different simulations set has been created. In the first simulation, the forward motion of the RoboSalmon vehicle has been analysed. While, in the other two simulations presented, the turning manoeuvring has been described for a small and a bigger turning radious respectively.
The simulation sets illustrated in the following sections last for 25 seconds. The simulation time has proved to be long enough in order to analyse the behaviour of the controlled system, and it is not to long for the simulations to be accomplished.

4.3.1 Forward motion

In this subsection, the results for the RoboSalmon vehicle for forward or surge motion using its biomimetic tendon drive propulsion system are presented and discussed using both the PID and the sliding mode steering control systems.
When the forward motion is simulated without the use of a steering control, the direction of the RoboSalmon is slightly moving away from the ideal trajectory, where the y position is always zero. This is caused by the oscillating tail propulsion system. In fact, the first oscillation cause the yaw angle to be non zero even if the tail centreline is zero, causing the RoboSalmon not to travel on the ideal direction.
In order to mantain the yaw angle to be zero it is necessary to use one of the two feedback controls implemented.
The behaviour of the RoboSalmon for forward motion using the PID controller and the sliding mode control, implemented in the previous sections, is shown in Figure 4.4.

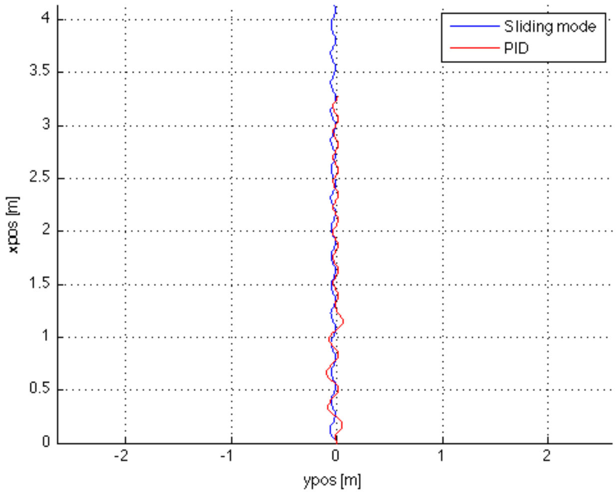

Figure 4.4: RoboSalmon's forward motion using the PID control algorythm (in red) and the sliding mode control (in blu).

The first thing that can be noticed is that both the steering control algorythms allow the RoboSalmon vehicle to reach the desired heading. This allows to say that, at least for forward motion, the task of implementing a usefull steering control system for the RoboSalmon has been accomplished.
Another thing to point out is the difference between the two heading control algorythms. As it can be seen from the Figure 4.4, in 25 seconds, the sliding mode steering control allows the vehicle to cover more road.
In order to understand the reason why the sliding mode control allows better performances than the PID control, a deeper analysis of the simulation is required.
In Figure 4.5, the linear and angular velocities of the RoboSalmon vehicle are illustrated.

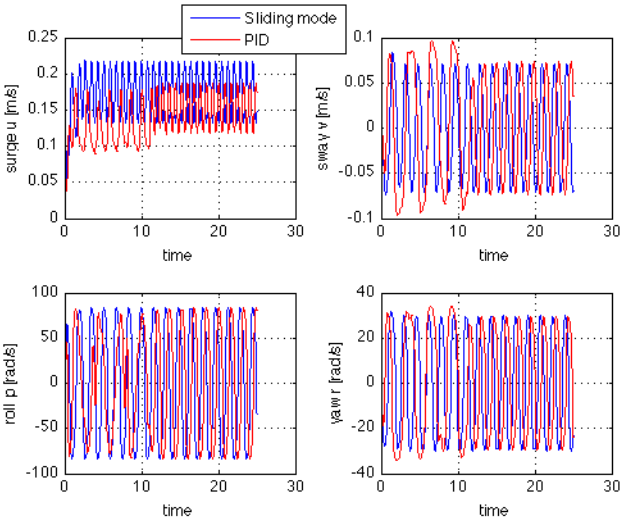

Figure 4.5: RoboSalmon velocities for forward motion using the PID control algorythm (in red) and the sliding mode control (in blu).

The roll, sway, and yaw oscillations have small meaning, since they're caused by the recoil motion and affect at the same way the controlled vehicle with both the steering control systems implemented.
The heave and pitch velocities have not been presented since they're supposed to be zero, as previously mentioned.
As it can be seen from the figure on the top right of Figure 4.5, the only significant difference can be noticed on the surge linear velocity. It is clear that using the sliding mode control insted of the PID algorythm for the heading control allows to reach an higher amplitude surge velocity, and this is the reason why more road can be covered.
In Figure 4.6, the linear and angular positions of the RoboSalmon vehicle are illustrated.

As has been said for the linear and angular velocites, also for the position the roll, yaw and y axis oscillations are caused by the recoil motion. Still the yaw angle is oscillating around zero, as it is supposed to do.
Watching at the y axis allows to notice that, for both the heading control algorythms, and

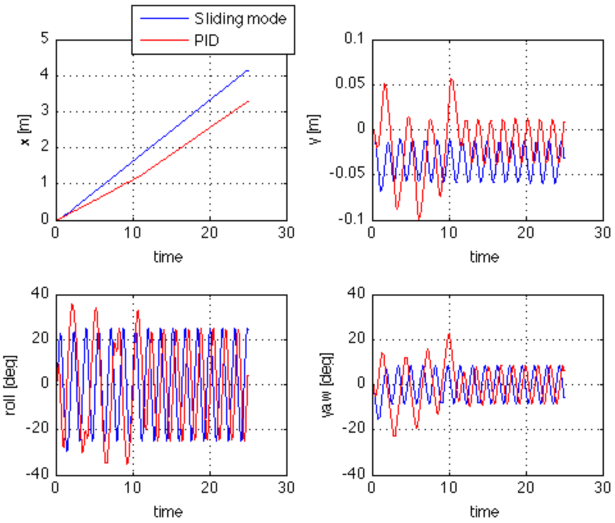

Figure 4.6: RoboSalmon positions for forward motion using the PID control algorythm (in red) and the sliding mode control (in blu).

in particular for the sliding mode control, the position of the RoboSalmon vehicle is slightly different from zero. This is caused by the first oscillation of the tendon tail, which cause the vehicle to slightly turn on the right.
The position of the RoboSalmon on the x axis is different since, as it has been already said, the sliding mode steering control allows to cover more road.
Another thing to notice is that, when the PID control is implemented, there is a significant initial oscillation around the steady state oscillation value for the y linear position and both the roll and yaw angular position. This is problably due to the overshoot and the absence of the anti-reset wind-up filter on the PID algorythm.

Analysing the previous figures only allows to notice that the sliding mode control, for forward motion, assures better performances, but they do not explain why.
In order to find out the reason why the sliding mode control is better than the PID one it is necessary to analyse Figure 4.7, in which the tail offset for both the steering control algorythms is presented.

At this point it is usefull to remember that the tail centreline is the output of both the steering control algorythms implemented.
As it can be seen from Figure 4.7, when using the PID heading control, the output of the algorythm, namely the tail centreline, is always saturating at ±45 degrees. This cause the RoboSalmon to have larger amplitude oscillations, which cause an higher energy loss due to the recoil motion.
Also real fishes tends to maintain a fairly constant tail oscillations amplitude when swimming. When a change in the surge velocity is needed, usually only the tail beat frequency is variated. The saturation of the PID controller is caused by the fact that it has been designed for the linearized system, and when the real RoboSalmon system is used, due to its highly non-linear and coupled dynamics, the PID control shows all its limitations. While the sliding mode

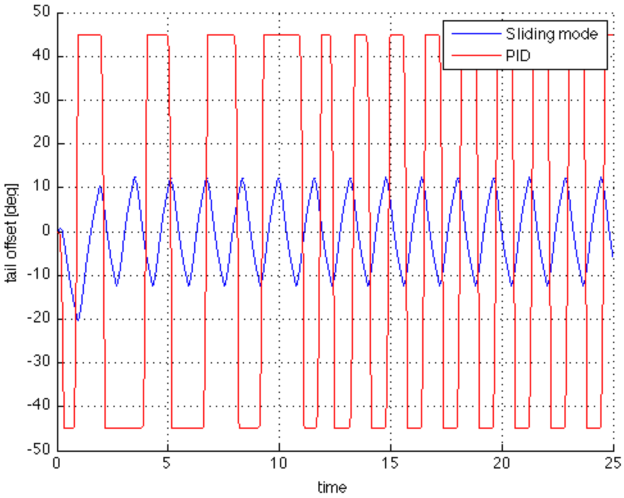

Figure 4.7: RoboSalmon tail centreline for forward motion using the PID control algorythm (in red) and the sliding mode control (in blu).

algorythm has been properly designed for non-linear and coupled dynamics, and this is the reason why it guarantees better performances.

4.3.2 Small amplitude heading

In this set of simulations the yaw reference angle has been chosen to have a small amplitude, namely 45 degrees. In order to reach the reference heading, the RoboSalmon vehicle has to perform a small turning manoeuvre, as it can be seen in Figure 4.8.

As it has been seen for forward motion, also for small amplitude reference heading the sliding mode control guarantees better performances, allowing the RoboSalmon vehicle to cover more road than using the PID algorythm.
In this simulation the oscillations amplitude when using the PID control are higher than the ones seen in the prevoius simulation. Although, both the algorythms designed allow the RoboSalmon vehicle to follow the desired reference heading.
This is due to the fact that the PID algorythm has been implemented for the linearized system, obtained for small amplitude reference input. When the reference input grows, the performance of the PID controller tends to be worse.
In order to understand the reason why the sliding mode control allows better performances than the PID control, a deeper analysis of the simulation is required.
In Figure 4.9, the linear and angular velocities of the RoboSalmon vehicle are illustrated.

The situation is similar to the one seen for forward motion. The oscillations are caused by the recoil motion and affect the vehicle with both the control systems implemented. In this case, the oscillations for the sway linear velocity have a slightly higher amplitude for the PID control. As it has been seen in the previous subsection, also for small reference heading the surge linear velocity mean is higher when the sliding mode is implemented, allowing the vehicle to cover

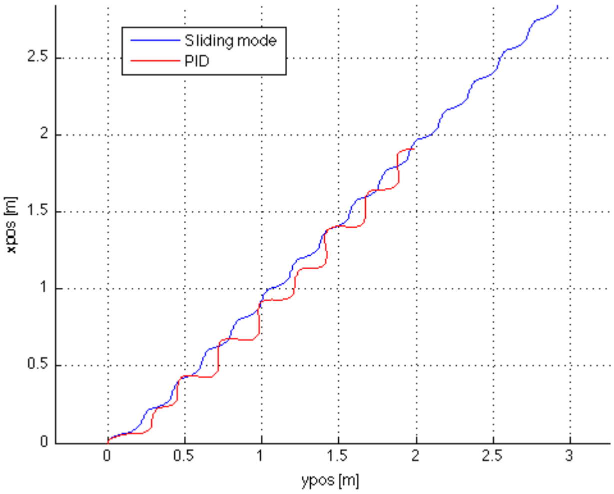

Figure 4.8: RoboSalmon's motion for small amplitude reference heading using the PID control algorythm (in red) and the sliding mode control (in blu).

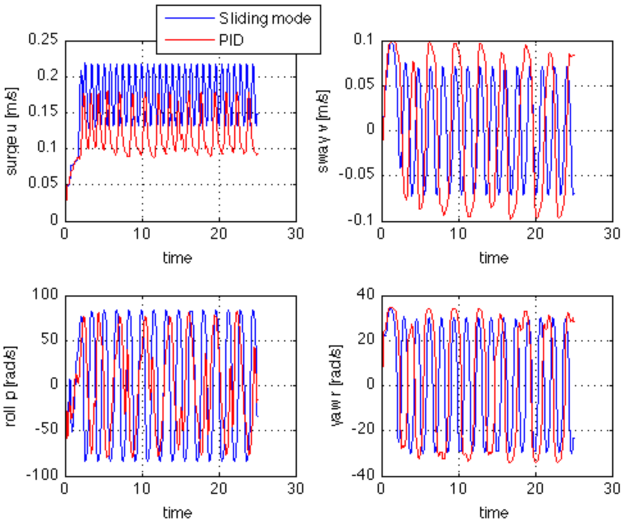

Figure 4.9: RoboSalmon velocities for small amplitude reference heading using the PID control algorythm (in red) and the sliding mode control (in blu).

more road.
In Figure 4.10, the linear and angular positions of the RoboSalmon vehicle are illustrated.

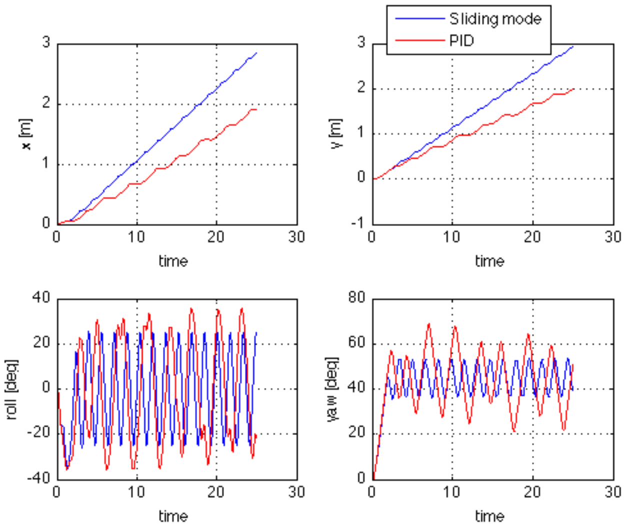

Figure 4.10: RoboSalmon positions for small amplitude reference heading using the PID control algorythm (in red) and the sliding mode control (in blu).

The first thing to notice is that, using the sliding mode heading control, allows the RoboSalmon vehicle to cover more road at the same time, as it has been previously noticed. This can be noticed analysing the x and y position of the vehicle.
The oscillations that affect the roll and yaw angular position are caused by the recoil motion. Meanwhile, for the yaw angular position, it can be noticed that the amplitude of the oscillations are higher when the PID control algorythm is implemented.
Another thing to point out is that, besides the oscillations, both the control algorythms implemented allow to reach and maintain the desired 45 degrees heading, as it can be seen on the yaw angular position figure.

Also for small heading reference the sliding mode control assures better performances when implemented in the steering control system of the RoboSalmon vehicle. In particular, the fact that the oscillations about the yaw steady state value are higher when using the PID control algorythm, causing the previously mentioned loss of performances, are caused by the saturation of the algorythm, as it can seen in Figure 4.11. The larger amplitude tail oscillations, when using the PID algorythm, cause an higher energy loss due to the recoil motion.

As mentioned in the previous simulations set, the saturation of the PID controller is caused by the highly non-linear and coupled dynamics of the RoboSalmon system, while the PID algorythm has been designed for the linearized system with small reference input. In this case the reference input is not close to zero, and that is the reason why the PID controlhas even worse performances than the ones seen for the forward motion.

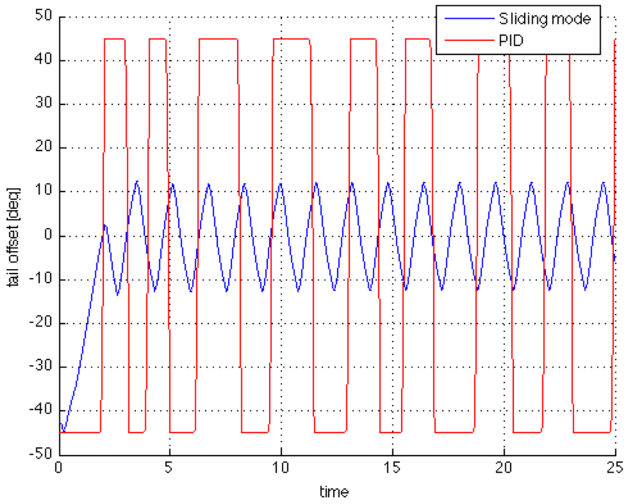

Figure 4.11: RoboSalmon tail centreline for small amplitude reference heading using the PID control algorythm (in red) and the sliding mode control (in blu).

4.3.3 High amplitude heading

In this set of simulations the yaw reference angle has been chosen to have a high value, namely 180 degrees. In order to reach the reference heading, the RoboSalmon vehicle has to perform a complete rotation, as it can be seen in Figure 4.12.

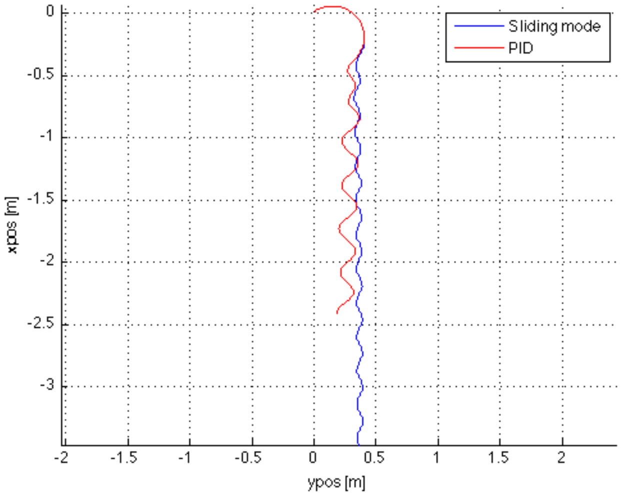

Figure 4.12: RoboSalmon's motion for high amplitude reference heading using the PID control algorythm (in red) and the sliding mode control (in blu).

The first thing to point out is that both the steering control algorythms implemented allow to reach and maintain the desired heading reference. This, finally, allows to say that the task

of implementing a usefull steering control system for the RoboSalmon biomimetic vehicle has been accomplished.
Even in this simulation it can be noticed that, when the sliding mode steering control is implemented, the RoboSalmon vehicle covers more road.
Another important thing to point out is that the behaviour of the RoboSalmon vehicle during the turning manoeuvering is the same with both the steering control algorythms designed.
In Figure 4.13, the linear and angular velocities of the vehicle are illustrated.

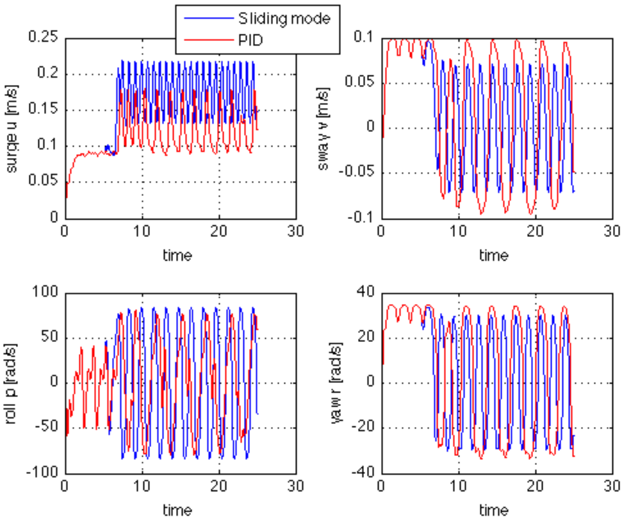

Figure 4.13: RoboSalmon velocities for high amplitude reference heading using the PID control algorythm (in red) and the sliding mode control (in blu).

The oscillations are caused by the recoil motion and have small meaning since they affect both the heading control systems implemented.
The first thing to notice is that the surge linear velocity has an higher amplitude when the sliding mode control is implemented, and this is the reason why it allows the RoboSalmon vehicle to cover more road.
It can be noticed that, for the first $5-6$ seconds of the simulation, there is no difference in the behaviour of the controlled systems, despite the two different control systems implemented. This means that, during the turning manoeuvering, the output of the two control systems is the same.
In Figure 4.14, the linear and angular positions of the vehicle are illustrated.

As it has been told for the linear and angular velocities, also for the positions, the oscillations are caused by the recoil motion and affect both the steering control algorythms, even if the amplitude is higher when the PID control is used.
During the turning manoeuvring the behaviour of the systems is the same, as it has been previously mentioned.
In this figure, it can be seen that the performances of the RoboSalmon system when the PID steering control is used are worse than the ones in the prevoius simulations, for forward motion

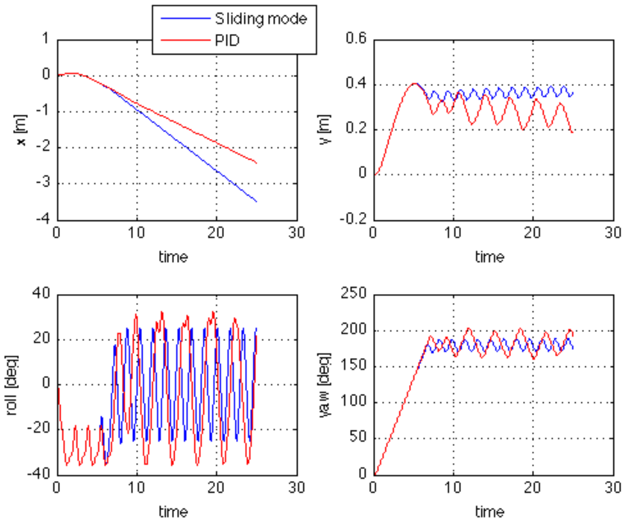

Figure 4.14: RoboSalmon positions for high amplitude reference heading using the PID control algorythm (in red) and the sliding mode control (in blu).

and small heading reference. In this case the reference heading is reached, but it is moving away from its steady state value.
This means that the PID implemented for the linearized system guarantees worse performances with the growing of the heading reference to follow.
In Figure 4.15, the output of the two heading control algorythms is presented.

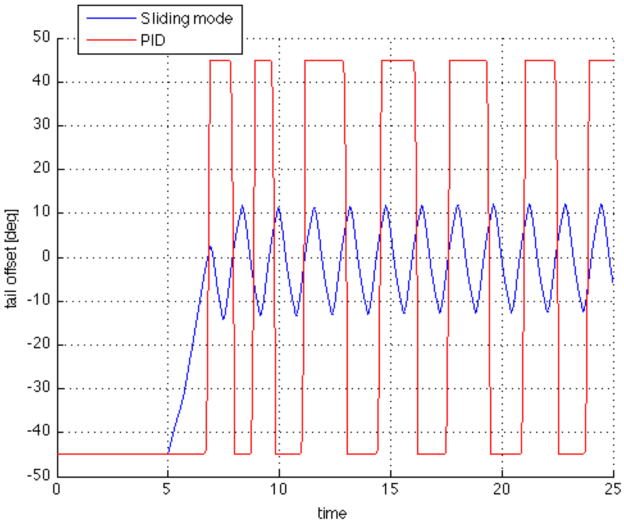

Figure 4.15: RoboSalmon tail centreline for high amplitude reference heading using the PID control algorythm (in red) and the sliding mode control (in blu).

As it has been said in the previous simulation subsections, the PID control output is always saturating, and this is the reason why the PID has proved itself to guarantee worse performances than the sliding mode control.

During the complete turning manoeuvre, it can be noticed that the output of the steering control algorythm is the same when the PID or the sliding mode algorythm is used. This is caused by the fact that, in order to accomplish the complete turning manoeuvring in the shortest time, the tail centreline is at its maximum desplacement.

Chapter 5

Guidance Law

The main problem in bringing autonomy to any vehicle lies in the design of a suitable guidance law.

For truly autonomous operations, the vehicle needs to have a reliable navigation, guidance and control system. In particular, the guidance system, generating suitable trajectories to be followed, represents the key element.

In this section the guidance law implemented for the RoboSalmon biomimetic fish will be discussed. At the same time, the aim of the simulations trials presented in the paper, is the comparison between the two heading control algorithm designed in the previous chapter, the sliding mode control and the PID control.

5.1 Guidance laws

All autonomous vehicles must have on-board navigation, guidance and control systems, which should work in accord with each other for proper operation. Imperfections in one system degrade the efficiency of the others.

In particular, the different tasks of the navigation, guidance and control are the following. The navigation system provides information related to the target, which is processed by the guidance system to generate reference headings. While the control system is responsible for keeping the vehicle on course as specified by the guidance processor.

The control system used in this chapter are the ones presented in the previous chapter. As already outlined, both the PID and the sliding mode steering control systems guarantee acceptable performances and, therefore, can be used as heading controllers.

In remotely operated systems, guidance commands are sent from a ground station, while autonomous vehicles have an on-board guidance processor which has the important task of elaborating the guidance commands. In this respect, a guidance system plays the vital role in bringing autonomy to the system.

Some definitions of the elements of a guidance system are presented as follows.

Guidance is the action of determining the course, attitude and speed of the vehicle, relative to some reference frame, to be followed by the vehicle [35].

And, from the perspective of a control system.

Guidance is a matter of finding the appropriate compensation network to place in series with

the plant in order to accomplish an intercept [36].
Also the father of inertial navigation, Charles Stark Draper, states.
Guidance depends upon fundamental principles and involves devices that are similar for vehicles moving on land, on water, under water, in air, beyond the atmosphere withi the gravitational field of earth and in space outside this field [37].
The guidance system decides the best trajectory to be followed by a vehicle, based on target location and vehicle capability.
The primary function of the elements that constitute a guidance system are sensing, information processing and correction. A rudimentary guidance and control system for a vehicle is shown in Figure 5.1.

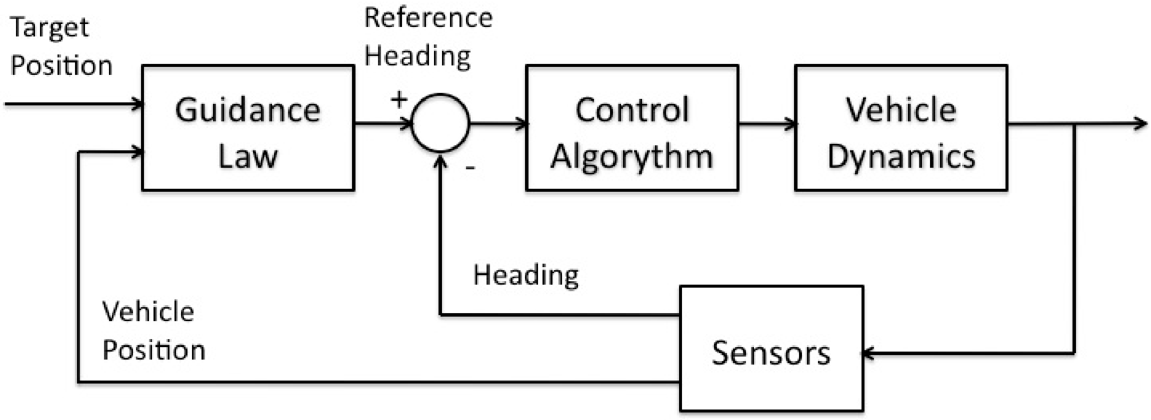

Figure 5.1: Scheme of the guidance and control system for a generic vehicle.

As shown in the figure above, the guidance system receives inputs from all the sensors on-board and generates the relevant signals or set points for the control system.
Guidance issues are mainly determined by the nature and location of the target and the environmental conditions. The nature of the target corresponds to the condition as to whether or not the target is stationary, moving, or manoeuvring. The target location is also imperative as it determines the heading to be followed by the vehicle. However, the accuracy of the system depends on the environmental conditions. As it'll be seen in the following sections, for autonomous underwater vehicles, the inluence of the ocean corrent has to be taken in account.
The guidance problem is also related closely to the bandwidth of the system. Indeed, it is often assumed while formulating the problem that the controller has a sufficiently large bandwidth to track the commands from the guidance subsystem. However, in practice, true vehicle capability can only be measured in the presence of constraints such as system dynamics and actuator limitations.

As mentioned before, the navigation, guidance and control of airborne vehicles have been reported extensively in the literature.
In particular, the guidance technology of missiles is a mature field with an abundance of guidance laws already implemented in real systems. Many different guidance laws have been employed exploiting various design concepts over the years. Currently, the popular terminal

guidance laws involve line-of-sight (LOS) guidance, LOS rate guidance, command-to-line-of-sight (CLOS) guidance, proportional navigation (PNG) [38], augmented proportional navigation guidance (APNG) [39] and optimal guidance laws based on linear quadratic regulator theory [40, 41] linear quadratic Gaussian theory [42] or linear quadratic exponential Gaussian theory [43].
Among the current techniques, guidance commands proportional to the line of sight angle rate are generally used by most high-speed missiles today to correct the missile course in the guidance loop.
Concerning tracking of moving targets, the missile guidance community probably has the most comprehensive experience. They commonly refer to the object that is supposed to destroy another object as either a missile, an interceptor, or a pursuer. Conversely, the threatened object is typically called a target or an evader.
In the missile guidance community, an interceptor typically undergoes three different phases during its operation; a launch phase, a midcourse phase, and a terminal phase. The greatest accuracy demand is associated with the terminal phase, where the interceptor guidance system must compensate for the accumulated errors from the previous phases to achieve a smallest possible final miss distance to target.
Since the main objective of the project is the design af a guidance law for an autonomous underwater vehicle, the RoboSalmon, here, the designations vehicle and target will be used. Furthermore, only terminal guidance strategies will be considered.

From the previous guidance laws directly comes the guidance techniques used on autonomous underwater vehicles.
The classical autopilots for autonomous underwater vehicles are designed by controlling the heading in the control loop. The guidance system can be easily designed including an additional loop in the control system, with position feedback from the sensors. The guidance system generates reference trajectories to be followed by the vehicle utilising the data gathered by the navigation system.
Denoting the position of the target by $p_t(t) = [x_t(t), y_t(t)]^T$, the control objective of a target-tracking scenario can be stated as

$$\lim_{t\infty}(p(t) - p_t(t)) = 0 \tag{5.1}$$

Where $p(t)$ denoted the position of the vehicle, and $p_t(t)$ is either stationary or moving by a non-zero and bounded velocity $v_t(t) = \dot{p}_t(t)$.

Different guidance laws will be presented in the following, namely line of sight, purse pursuit, constant bearing and Lyapunov based.

- **Line of sight guidance:**
  Line of sight (LOS) guidance is classified as a so-called three-point guidance scheme since it involves a typically stationary reference point in addition to the vehicle and the target. The LOS denotation stems from the fact that the interceptor is supposed to achieve an intercept by constraining its motion along the line of sight between the reference point and the target.

- **Pure pursuit guidance:**
  Pure pursuit (PP) guidance belongs to the so-called two-point guidance schemes, where only the vehicle and the target are considered in the engagement geometry.
  Simply put, the vehicle is supposed to align its velocity along the line of sight between the vehicle and the target.
  This strategy id equivalent to a predator chasing a prey in the animal world, and very often results in a tail chase.

- **Constant bearing guidance:**
  Constant bearing (CB) guidance is also a two-point guidance scheme, with the same engagement geometry as a PP guidance. However, in a CB engagement, the vehicle is supposed to align to the relative vehicle-target velocity along the line of sight between the interceptor and the target.
  This goal is equivalent to reducing the LOS rotation rate to zero such that the vehicle perceives the target at a costant bearing, closing in on a direct collision course. CB guidance is often referred to as a parallel navigation.
  The most common method of implementing CB guidance is to make the rotation rate of the vehicle velocity directly proportional to the rotation rate of the vehicle-target LOS, which is widely known as proportional navigation (PN).

- **Lyapunov based guidance:**
  In the Lyapunov based guidance a Lyapunov function can be considered as a generalisation of the concept of distance or energy.
  The Lyapunov theorem states that, if the distance of the state along any trajectory of a dynamic system, $\dot{x} = Ax$, decreases with time, then the state $x(t)$ must tend to zero as the time tends to the infinity. This concept has been used to develop a new guidance law for unmanned underwater vehicles.

The LOS guidance is the most widely used scheme in the field of autonomous underwater vehicles. That's the reason why it has been chosen as the RoboSalmon's guidance law, and it will be further analysed in the following section. Furthermore, in the simulation trials the target is considered to be stationary.
Before proceeding with the RoboSalmon's guidance law, different technologies based on the line of sight guidance law will be discussed in the following.

- *Vision based guidance:* The vision based guidance technique has been inspired from the work of ROV operators, which utilise or rely on the visual information to perform tasks thus making a strong argument that visual imagery could be used to guide an autonomous underwater vehicle.
  Vision based guidance has been mainly employed for cable tracking and docking problems.
  Briest *et al.* [44] suggest an optical terminal guidance scheme for the docking of an AUV using a beacon. The beacon cuold be a light-emitting device, which can be identified using

photo detectors onboard the AUV. The disadvantage of using beacon is that in swallow waters, especially during the daylight, the photo detectors can lock on to sunlight. The remedy could be to adjust the frequency of the light emitted by the beacon.

Gaskett *et al.* [45] proposed a vision based guidance for an AUV using two cameras. The authors demonstrated that the guidance could be achieved by a feature algorithm that requires two correlation operations within the feature tracker. The feature motion tracker follows each feature between previous and current images from a single camera while the feature range estimator correlates between the left and right camera images. The feature motion tracker correlates stored feature templates to determine the image location and thus the direction to each feature. Range is determined by correlating the features in both images to find their pixel disparity. This pixel disparity is related to an absolute range using camera extrinsic and intrinsic parameters, which are determined by calibration. The direction and range to each feature is then fed to the controller, which determines a set of thruster commands. To guide the AUV, thruster commands become a function of the position of visual features.

A major drawback of using visual systems in underwater guidance is that the performance degrades in case fo turbid water or when a cable is buried or there might be other similar cables appearing in the image. For such cases, a multi-sensor fusion technique has been proposed. This technique uses dead reckoning position uncertainty with a two dimensional position model of the cable to predict the region of interest in the image captured by a camera mounted on the AUV. The two dimensional position model of the layout of the cable is generated by taking the position coordinates of a few points along the cable, which is then used to predict the most likely region of the cable in the image.

Balasuriya and Ura [46] proposed a vision based guidance law using a single camera. The technique has been implemented for cable tracking and following a moving object. The basic idea underlying these schemes is that the feature to be tracked introduces a particular geometric feature in the image captured by the CCD camera. The vision processor then labels these features, extract their location in the image and interprets the appearance into a guidance parameter. These parameters are then fused with other sensory parameters to determine the control references for the underwater vehicle.

Rock *et al.* [47] devised a vision based system to track a dot of light generated by a laser. The hardware comprises two cameras, one of which is used to locate the target. The vision system works by scanning the image from the last known location of the target, or from the centre of the screen if the target was not previously in view. The pixels are examinated row by row, expanding outward towards the edge. If a target is found, ita angle and elevation with respect to the centre of the image is evaluated and transmitted to the vision processor, while range can be found using successive images from both cameras. The proposed law has been proved to be valid only in the case of a single distinguishable target.

- *Chemical signals guidance:* Consi *et al.* [48] proposed a guidance scheme for AUVs using chemical signals, using the fact that marine animals make extensive use of underwater chemical signals.

  The goal of the research was to use the information in the chemicals signals to locate the source of a chemical discharge. In this respect, it has a number of scientific, envirnmental, commercial and defence related applications. The sensors used in the AUV are conductivity sensors, and they're are used to enable the vehicle to follow a plume of saltwater in a freshwater flow-through flume. A simple gradient following algorithm is implemented to locate the source of discharge which has the obvious disadvantage of geting trapped in local concentration minima and maxima.

- *Guidance using magnetometers for cable tracking:* The underwater cable network and its capacity are expanding very rapidly, and its installation and maintenance is becoming more importante as well. Autonomous underwater vehicles could be a potential tool for underwater cable tracking, especially in case of deep water where human intervention is not possible.
  For buried electrical or telecommunication cables, the strategy adopted for cable tracking is to use on-board magnetometers, which can detect the magnetic field induced from the current flowing in the cable. The data from the magnetometer is fed to a cable locator that estimates the direction, burial depth and the distance of the vehicle from the cable. The data from the cable locator is then used to guide the vehicle.
  Guidance using magnetometers has limited applications, as it can only be used to guide the vehicle towards the source of the magnetic field.

- *Electromagnetic guidance:* The main problem of using optical or visual guidance systems is that the response is only good in nonturbid water, clear environments, and it's limited over a wide range of background lighting and water turbidity conditions. Also, the AUV have to lie within the field of light emitted by the beacon, and must be oriented in such a way that the optical sensors can detect the light.
  Feezor *et al.* [49] employed an electromagnetic guidance technique during the homing/docking mode of an AUV. The electromagnetic guidance uses a magnetic field generated by the coils in the dock, which is sensed by the coils in the AUV. The guidance system provides the AUV not only the bearing to the dock, but also the angle of the AUV relative to the field lines and thus the angle relative to the dock entrance.

5.2 Line of Sight guidance law

As stated in the previous section, the waypoint guidance law by line of sight is the most widely used scheme in the field of autonomous underwater vehicles.
In the key paper by Healy and Lienard [50], guidance is achieved by a heading command to vehicle's steering system to approach the line of sight between the current position of the vehicle and the waypoint to be reached.
This guidance strategy comes from the missile guidance, where it's related to "proportional navigation". The difference is that, in guiding AUVs, the vehicle response is slow, compared to the rates of change in command, unless the waypoint is many vehicle length away.
This guidance strategy can be used for path following, in this case guidance is achieved by splitting the path into a number of waypoints to be reached in the exact order.
The line of sight is defined to be the horizontal plane angle given by

$$\psi = \tan^{-1}\left[\frac{y_t(k) - y(t)}{x_t(k) - x(t)}\right] \tag{5.2}$$

Where $[x_t(k), y_t(k)]$ denotes the position of the next waypoint to be reached, while $[x(t), y(t)]$ is the current position of the vehicle.
As mentioned in the previous chapter, the output of the line of sight guidance law ψ directly feeds the steering control system.
The decision as a waypoint has been reached or not is made checking whether the vehicle position lies within a so called "ball of acceptance" ρ_0 defined around every waypoint. Namely the waypoint is considered to be reached if the location of the vehicle and the distance ρ_0 are such that the following equation is satisfied

$$\rho^2(t) = [x_t(k) - x(t)]^2 + [y_t(k) - y(t)]^2 < \rho_0^2 \tag{5.3}$$

If the waypoint is reached, then the system triggers the selection of the next waypoint, depending on the navigation plan.
On the other hand, if the condition that $d\rho/dt$ goes from negative to positive without the above equation being met, then the waypoint is not reached. In this case the guidance law must contains logic that will either hold the current waypoint, directing the vehicle to circle, or enter the next waypoint, depending on a mission planning decision.
For the RoboSalmon it has been chosen to hold the current waypoint until the vehicle manages to reach it. Anyway, as it will be seen in the following sections, using the line of sight guidance law, the RoboSalmon reaches all the waypoints stored in the mission plan.
The value of the "ball of acceptance" $\rho_0 = 40cm$ is approximitely half the length of the vehicle. Usually the values chosen as "ball of acceptance" are three or four times the vehicle length, but, thanks to the great manouvrability of the RoboSalmon, a smaller value can be used. In this way it is possible to use shorter path during the simulation, resulting in a faster simulation procedure.

It is really important to care about the proper quadrant when using the $\tan^{-1}$ function.
Actually in the RoboSalmon's guidance implementation it has been used the four quadrant inverse tangent function $atan2$, since its output goes from $-\pi$ to π. During the simulations of the RoboSalmon's guidance law it has been seeen that the function $atan2$ has some inaccuracy

problems when the output is close to $\pm\pi$. This problem is due to the singularity of the tangent function.

In order to solve the problem, and make the RoboSalmon capable of reaching point requiring a complete turning of 180 degrees, the reference system has been diveded into two different quadrant, as it can be seen on the following Figure 5.2. And the implemented algorithm checks in which of the quadrant the waypoint is located.

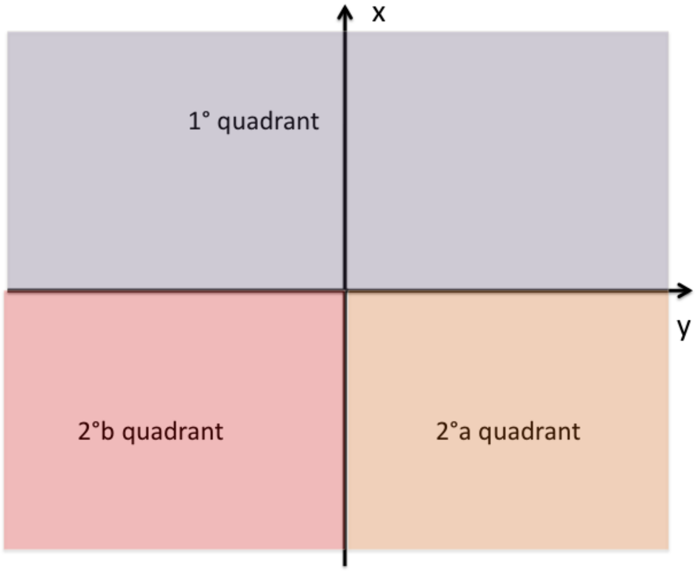

Figure 5.2: Division of the reference frame into quadrants.

In the first quadrant, the line of sight guidance law works as previously stated, without any changes in the algorithm.

On the other hand, if the waypoint is located in the second quadrant, the algorithm has been slightly changed in order to avoid the inaccuracy around $\pm\pi$ outputs. To solve the problem previously mentioned, both the current position of the RoboSalmon $[x(t), y(t)]$ and the position of the next waypoint to be reached $[x_t(k), y_t(k)]$ have been rotated of 180 degrees. Using this method, the output of the line of sight algorithm can never be close to the inaccuracy, around $\pm\pi$, point. In order to reach the desired waypoint and not the rotated one, it has been added $\pm\pi$ radiants to the output of the LOS algorythm, namely the reference heading needed to reach the rotated waypoint.

As it can be seen from the previous figure, the second quadrant has been further divided into two sub-quadrant. If the waypoint is located in the a second quadrant, then it has been added $+180$ degrees to the reference heading. While, if the waypoint is located in the b second quadrant, then -180 degrees has been added to the reference heading.

The sub-division of the second quadrant has been implemented to make the RoboSalmon to always have the minimum turning radious.

Another major problem found in the implementation of the algorithm still concerns the singularity of the four quadrant tanget function around $\pm\pi$. Specifically, the problem occurs when the reference heading changes (meaning that the waypoint has been reached) and the new ref-

erence heading has an amplitude higher than $\pi/2$ and the sign is the opposite of the previous heading sign. In this case the algorithm makes the RoboSalmon turning without going through the π angle, making the RoboSalmon to take the longest path to turn towards the next waypoint.
The result of this complication can be seen in the following Figure 5.3.

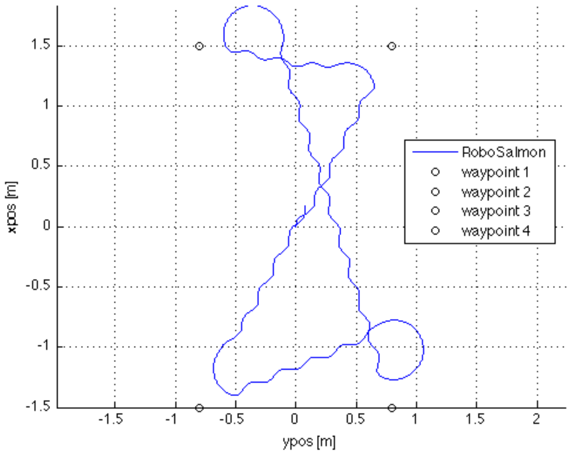

Figure 5.3: RoboSalmon following the path of the eight figure.

With the current algorithm, it can be seen that the RoboSalmon, during two change of directions, in order to reach the next waypoint stored, takes the longest turning circle. This behaviour is highly inefficient, bringing a useless loss of energy.
In order to solve this problem, when the waypoint to reach changes, in the LOS algorithm has been implemented the logic to check if the reference heading to reach the new waypoint has an amplitude higher than $\pi/2$ and the sign is opposite to the sign of the previous reference heading. If the condition is verified than the algorithm add -2π to the reference heading elaborated with the LOS algorithm.
The solution adopted manages to solve the inefficiency problem as it can be seen in the following Figure 5.4.

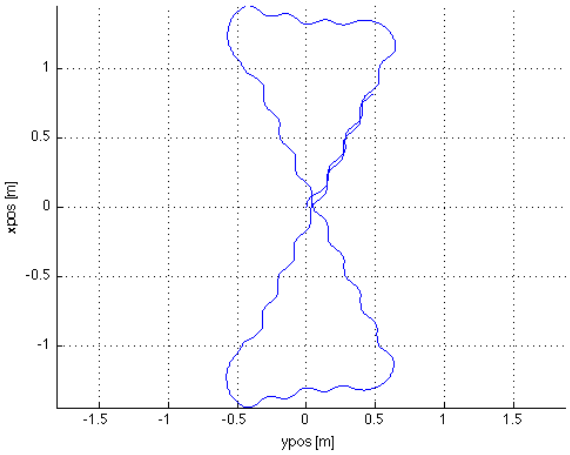

Figure 5.4: RoboSalmon following the path of the eight figure, with the added logic to solve the inefficiency problem.

5.3 Comparisons between heading control algorithms

As stated in the previous sections, the guidance law depends deeply from the control algorithm implemented. Since the guidance law generates heading reference, the control system is responsible for keeping the vehicle on the exact heading.
In this section the differences between the LOS guidance strategy with the sliding mode control algorithm and the LOS guidance law with the PID control algorithm have been analysed.
The figure of eight is the path followed by the RoboSalmon in all the simulations presented in this section to make a comparison between the two systems. The waypoints chosen to make the RoboSalmon follows the figure of eight path are:

$$\begin{aligned} wp_1 &= [1.5, 0.8] \\ wp_2 &= [1.5, -0.8] \\ wp_3 &= [-1.5, 0.8] \\ wp_4 &= [-1.5, -0.8] \end{aligned} \tag{5.4}$$

In order to complete the figure of eight, when the RoboSalmon reaches the last waypoint, wp_4, then the next waypoint stored in the navigation plan is the first waypoint, wp_1.
The simulations last for just 60 seconds.
In Figure 5.5, the position of the waypoints and the path followed by the RoboSalmon are presented.

In order to reach a better understanding of the comparison between the two guidance and control systems designed, the efficiency of the systems in terms of electrical and motion powers has been studied.
In the implementation of the RoboSalmon biomimetic vehicle all the informations to elaborate the powers have been saved. The equations to calculate the electrical power consumption end the motion power generated by the tendon drive tail propulsion system are shown respectively

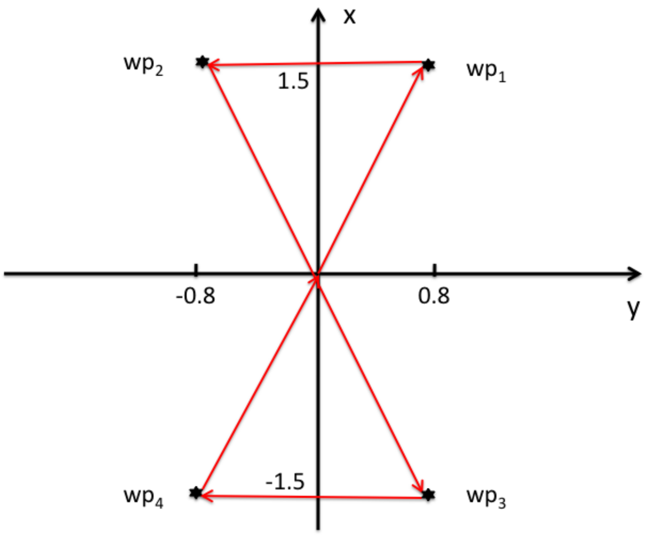

Figure 5.5: Waypoints stored in the RoboSalmon's navigation plan.

in equations (5.5) and (5.6):

$$P_{el} = V * i \tag{5.5}$$

$$P_m = F * u \tag{5.6}$$

Where V and i are respectively the voltage and the current of the servo motor used to move the tendons, F is the force produced by the tail and u is the surge velocity of the RoboSalmon.

In the the following Figure 5.6 the motion of the RoboSalmon, following the figure of eight with both the PID and the sliding mode heading control, is presented.

The first thing that can be noticed from the figure is that the RoboSalmon with the sliding mode control system covers more space than the one using the PID controller.
In the following table, the exact times in which the waypoints have been reached are presented.

	wp_1	wp_2	wp_3	wp_4
PID	13.0110	24.4470	51.0740	nr
Slid. mode	8.5570	16.5790	35.4550	43.1810

Where the abbrevation nr stands for not reached.
Thanks to both the figure and the table, it is easy to notice that the sliding mode control for the heading of the RoboSalmon allow better perfomance than the PID heading control.
It can be seen that, using the PID heading control, the RoboSalmon does not reach the fourth waypoint. While, with the sliding mode, not only the fourth waypoint is reached, but it has been reached even before the RoboSalmon with PID has reached the third waypoint.
Another thing that can be noticed from the figure is the oscillatory motion of the RoboSalmon vehicle. These oscillations, caused by the recoil motion, are due to the mechanical implementation of the tendon drive tail propulsion system and can not be eliminated.

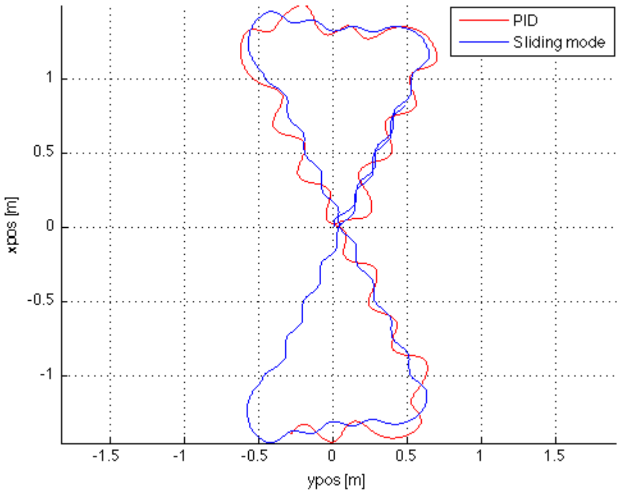

Figure 5.6: RoboSalmon following the path of the eight figure, with both the PID (in red) and the sliding mode (in blue) heading control system.

However, the oscillations with the PID heading control are deeper than the ones using the sliding mode heading control, and this brings to the loss of energy that reduces the perfomance of the vehicle with the PID heading control.
The oscillations generated by the tendon drive tail is deeper when using the PID heading control because the PID gains have been elaborated with the linearization method for small reference input. When the heading reference is not close to zero, then the algorithm makes the control signal always to saturate, and this generates a great loss of energy, as already stated in the previous chapter.
Before proceeding with the analisis, it is important to remember that the output of the heading control algorithms, both in the PID and in the sliding mode, for the RoboSalmon biomimetic vehicle is the tail offset.
In the following Figure 5.7 the outputs of both the control algorithms are presented.
As previously mentioned, the difference between the two heading control algorithms is very clear.
Using the sliding mode heading control, the saturation of the signal is reached only during the turning manoeuvre, as it should be. On the opposite, with the PID heading control, the signal is always saturating on the positive and negative side, making the tail to reach the maximum desplacement with every beat.
This high tail desplacement beat is highly inefficient, especially in the RoboSalmon vehicle, because it aggravates the recoil motion problem.

Now it is useful to procced with the analysis of the powers. In Figure 5.8 the electrical power consumption and the motion power for both the heading control algorithms are presented.
The only thing that can be clearly noticed is that the motion power generated by the tendon drive propulsion using the sliding mode heading control is generally higher than the one produced using the PID algorithm.
In order to understand what is happening, it is better to analyse the average powers during the

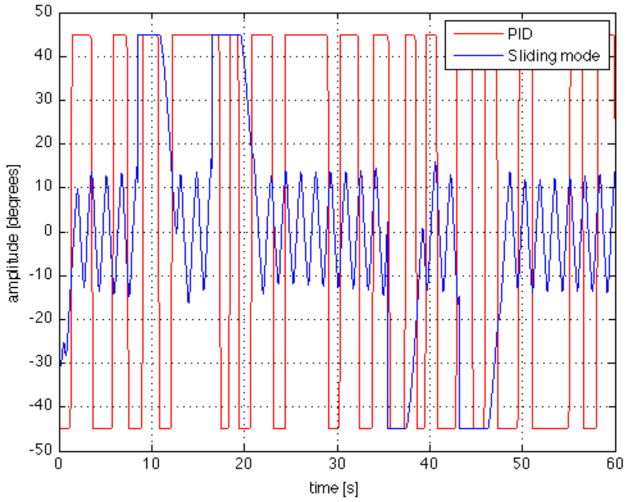

Figure 5.7: Output of the heading control algorithms during the manoeuvering phase.

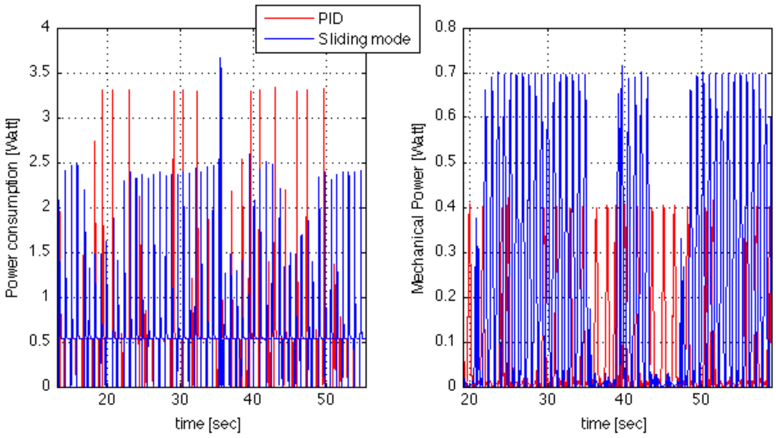

Figure 5.8: Electrical power (on the left) and motion power (on the right) involved during the simulation trial.

whole manoeuvring.

	average electrical power	average motion power
PID	0.5858	0.0753
slid. mode	0.6219	0.2089

It can be seen that the electrical power consumption is plus or less the same for both the heading control algorithms.
The real difference between them can be seen in the motion power generated by the tendon drive propulsion system. Using the sliding mode control brings to a greater efficiency than the one using the PID, in fact the motion power using the former is almost three times higher than the latter.

Chapter 6

Ocean Current

As mentioned in the introduction, the disturbances created by the Ocean currents has to be taken in account.
In this section the model for the Ocean current has been analysed. Then the influence of the Ocean current on the RoboSalmon has been studied with the use of simulations.

6.1 Ocean current mathematical model

Currents in the upper layers of the ocean are mainly generated by the atmospheric wind system over the sea surface.
Besides the *wind generated currents*, the heat exchange at the sea surface together with the salinity changes develop an additional sea current component, usually referred to as *thermohaline currents*. This process also explains why varying water types are observed in different climatic regions. The oceans are conveniently divided into two water spheres, the cold and the warm water sphere, which again are separated by the 8 degrees isotherm.
Since the earth is rotating, the Coriolis force will try to turn the major currents to the right in the northern hemisphere and opposite in the southern hemisphere.
Finally, tha major ocean circulations will also have a tidal component arising from planetary interactions like gravity. In coastal regions and fjords tidal components can obtain very high speeds, in fact speeds of 2 or 3 m/s can be measured.

The 10th ISSC (1988) proposed that one write the surface velocity V_c as a sum of the following velocity components, shown in equation (6.1).

$$V_c = V_t + V_{lw} + V_s + V_m + V_{set-up} + V_d \tag{6.1}$$

Where V_t is the tidal component, V_{lw} refers to the component generated by the local wind, V_s is the component generated by the nonlinear waves (Stokes drift), V_m represents the component from majior ocean circulation (for example the Gulf stream), V_{set-up} is the component due to set-up phenomena and storm surges and V_d is the local density driven current components governed by strong density jumps in the upper ocean.

- **Tidal component:**
  Let the vertical component z (m) be measured positive downwards. Hence, the velocity

profile of the tidal component can be written as shown in the following equation (6.2).

$$V_t(z) = \begin{cases} V_t(0) & \text{for} \quad 0 \leq z \leq d - 10 \\ V_t(0) \log_{10}\left(1 + \frac{9z}{d-10}\right) & \text{for} \quad d - 10 < z < d \end{cases} \tag{6.2}$$

Where $V_t(0)$, in (m/s), is the surface speed of the tidal and $d > 10$ (m) is the water depth.

- **Component generated by nonlinear waves:**
  The second order wave disturbances or so-called wave drift forces can be treated as an additional current component. The contribution to the surface drift (Stokes theory) resulting from the irrotational properties of the waves is shown in equation (6.3).

$$V_s(z) = \sum_{i=1}^{N} k_i \omega_i A_i^2 e^{-2k_i z} = \sum_{i=1}^{N} \frac{4\pi^2 A_i^2}{t_i \lambda_i} e^{-4\pi z/\lambda_i} \tag{6.3}$$

  The derivation of this expression is found in Sarpkaya (1981).

- **Component generated by local wind:**
  The component generated by the local wind can be written as shown in equation (6.4).

$$V_{lw}(z) = \begin{cases} V_{lw}(0)\frac{d_0 - z}{d_0} & \text{for} \quad 0 \leq z \leq d_0 \\ 0 & \text{for} \quad d_0 < z \end{cases} \tag{6.4}$$

  Where d_0 is the reference depth for the wind-generated current, usually taken to be 50 metres.
  Collar (1986) has shown that $V_{lw}(0)$ can be approximated as:

$$V_{lw}(0) = 0.02V_{10}$$

  Where V_{10}, in (m/s), is the wind velocity measured 10 metres above the sea level.

6.2 Including the ocean current in the RoboSalmon dynamics

It is known that the earth-fixed linear velocity could be transformed to body-fixed linear velocities by applying the principal rotation matrices $J_1^T(\phi, \theta, \psi)$.
The earth-fixed current velocity vector will be denoted by $[u_c^E, v_c^E, w_c^E]$. Hence, the body-fixed components can be computed as shown in equation (6.5).

$$\begin{bmatrix} u_c \\ v_c \\ w_c \end{bmatrix} = J_1^T(\phi, \theta, \psi) \begin{bmatrix} u_c^E \\ v_c^E \\ w_c^E \end{bmatrix} \tag{6.5}$$

Where $[u_c, v_c, w_c]$ denoted the current velocity in the body-fixed frame, and

$$J_1(\phi, \theta, \psi) = \begin{bmatrix} c\psi c\theta & -s\psi c\phi + c\psi s\theta s\phi & s\psi s\phi + s\psi c\phi s\theta \\ s\psi c\theta & c\psi c\phi + s\phi s\theta s\psi & -c\psi s\phi + s\theta s\psi c\phi \\ -s\theta & c\theta s\phi & c\theta c\phi \end{bmatrix}$$

is the principal rotation matrix.
It will be assumed that the body-fixed current velocity is constant or at least slowly-varying, such that the following holds:

$$\dot{\nu}_c = 0 \quad \Longrightarrow \quad \dot{\nu}_\tau = \dot{\nu}$$

It is useful to remember that $\nu = [\nu_1 \quad \nu_2]^T$, where $\nu_1 = [u, v, w]^T$ and $\nu_2 = [p, q, r]^T$ are rispectively the linear and the angular velocity of the RoboSalmon in the body-fixed frame.
Likewise, the vector ν_c refers to the the current velocities in the body-fixed frame. In this case the velocities are only linear, so that $\nu_c = [\nu_{1c} \quad \nu_{2c}]^T$, yields $\nu_{1c} = [u_c, v_c, w_c]^T$ and $\nu_{2c} = [0, 0, 0]^T$.
Finally, the vector ν_τ is given by the following equation (6.6).

$$\nu_\tau = \nu - \nu_c \tag{6.6}$$

Hence, the nonlinear relative equations of motion considering the current velocity vector ν_c is given by the following equations (6.7) and (6.8).

$$M\dot{\nu} + C(\nu_\tau)\nu_\tau + D(\nu_\tau)\nu_\tau + g(\eta) = \tau \tag{6.7}$$

Where $M = M_{rb} + M_a$ is the inertia matrix, composed of the rigid body inertia matrix and the added inertia matrix, $C(\nu) = C_{rb}(\nu) + C_a(\nu)$ is the Coriolis and centripetal matrix, made up of two components, the Coriolis and centripetal matrix due to the rigid body and the terms relating to the added mass effect, $D(\nu)$ is the dumping matrix, $g(\eta)$ is the vector of gravitational forces and moments and τ is the vector of control inputs.

$$\dot{\eta} = J(\eta)\nu \tag{6.8}$$

Where $\dot{\eta} = [\dot{x}, \dot{y}, \dot{z}, \dot{\phi}, \dot{\theta}, \dot{\psi}]$ is the vector of the linear and angular velocities in the earth-fixed frame, and $J(\eta)$ is the transformation matrix.
Notice that this representation of the RoboSalmon's dynamics is based on the state variables

(ν, ν_c, η).

Now it could be useful to see how the current model can be defined. Firstly the general three dimensional current model for submerged body will be analyse. Than the two dimensional model used throughout the project is presented.

6.2.1 Three dimansional current model:

If the vertical velocity profile $V_z(z)$ is known, then the average current velocity V_c over the draft of the vehicle can be computed as:

$$V_c = \frac{1}{T}\int_0^T V_z(z)dz$$

Where T is the hull draft.
The earth-fixed current velocity components (u_c^E, v_c^E, w_c^E) can be related to V_c by defining two angles, α (angle of attack) and β (sideslip angle), describing the orientation of the amplitude V_c about the y and z axis respectively.
Using the rotational matrices given by the Euler theory, the equation (6.9) can be written as.

$$\begin{bmatrix} u_c^E \\ v_c^E \\ w_c^E \end{bmatrix} = C_{y,\alpha} C_{z,-\beta} \begin{bmatrix} V_c \\ 0 \\ 0 \end{bmatrix} \tag{6.9}$$

Where V_c is the average current velocity in the earth-fixed reference frame,

$$C_{y,\alpha} = \begin{bmatrix} c\alpha & 0 & -s\alpha \\ 0 & 1 & 0 \\ s\alpha & 0 & c\alpha \end{bmatrix}$$

and

$$C_{z,-\beta} = \begin{bmatrix} c\beta & -s\beta & 0 \\ s\beta & c\beta & 0 \\ 0 & 0 & 1 \end{bmatrix}$$

The notation $C_{i,\lambda}$ denotes the transformation matrix defining a rotation angle λ about the i axis.
Expanding the expression in equation (6.9) yields the link between the current velocities in the earth-fixed frame and the average velocity V_c together with the angles α and β, shown in the equations system (6.10).

$$\begin{cases} u_c^E &= V_c \cos\alpha\cos\beta \\ v_c^E &= V_c \sin\beta \\ w_c^E &= V_c \sin\alpha\cos\beta \end{cases} \tag{6.10}$$

6.2.2 Two dimensional current model

In this project the RoboSalmon vehicle is considered to work in a two dimensional space. Hence, the z axis, namely the depth, both in the earth-fixed and in the body-fixed frames is supposed

to be constant.
For this reason, the three dimensional current model presented previously can be simplyfied. For the two dimensional case, the earth-fixed current components can be described by two parameters only, that is average current speed V_c and direction of current β.
Consequently, the three-dimensional equations system (6.10) reduce to the expression shown in equation (6.11).

$$\begin{cases} u_c^E &= V_c \cos\beta \\ v_c^E &= V_c \sin\beta \end{cases} \tag{6.11}$$

Since only the horizontla motion of the vehicle is considered, it can be assumed that both ϕ and θ are zero, which implies that the current components in the body-fixed frame (u_c, v_c) can be computed using the expression shown in equation (6.12).

$$\begin{bmatrix} u_c \\ v_c \end{bmatrix} = \begin{bmatrix} \cos\psi & \sin\psi \\ -\sin\psi & \cos\psi \end{bmatrix} \begin{bmatrix} u_c^E \\ v_c^e \end{bmatrix} \tag{6.12}$$

Substituting the expression for u_c^E and v_c^E, seen in equation (6.11), into the above eqution (6.12), finally yields the expression for the current components in the body-fixed frame, shown in equation (6.13).

$$\begin{cases} u_c &= V_c \cos(\beta - \psi) \\ v_c &= V_c \sin(\beta - \psi) \end{cases} \tag{6.13}$$

6.3 Ocean current disturbance and RoboSalmon

In this section some simulation about the RoboSalmon's motion in the presence of disturbances, namely the ocean current, will be presented. The aim of this part of the project is to analyse the behaviour of the RoboSalmon vehicle in presence of disturbances.
In order to carry on a good evaluation of the performance of the RoboSalmon in presence of disturbances a series of three simulations will be discussed.
In the first simulation series, the aim is to discover the maximum average current speed amplitude, V_c, applied on the vehicle and that can still allow good perfomances in terms of path following (the usual figure of eight will be used). During these simulations the direction of the the current β is not really important.
Subsequently, the amplitude of the average current speed will bw considered to be costant, and the direction of the current will be the matter of study. Firstly, the current direction will always be orthogonal to the heading of the vehicle. Finally, the current direction will be considered to be opposite to the RoboSalmon motion.
The path chosen during these simulations is the figure of eight presented in the previous section in Figure 5.5.

6.3.1 Maximum average current amplitude

The first thing to study in terms of ocean current disturbances is the limit of the average current velocity that can affect the RoboSalmon vehicle without making the vehicle unable to follow the path.
Analysing some simulations it has been seen that the RoboSalmon vehicle can operate only in certain condition, in fact the amplitude of the current velocity has to be low in order to mantain accetable performances in term of path following. For this reason the maximum current velocity used throughout this series of simulations is $V_{max} = 0.2$ (m/s).
The path chosen is a straight line, and the seven waypoints are positionned from 0.4 (m) to 2.8 (m). The waypoints are positioned at 40 (cm) distances to the next.
The amplitude of the current average velocity grows in a linear way from 0 to V_{max} during the 25 seconds simulation, while the direction of the current has been chosen to be costant, and equal to 45 degrees.
In Figure 6.1 the simulation is shown. As it can be seen from the figure, the simulation has been done for both the steering control algorithms.

The first thing to notice is that, even in this simulation, the sliding mode control guarantees better performance than the PID control algorithm.
In the following table the time in which the waypoints are reached is shown.

	wp_1	wp_2	wp_3	wp_4	wp_5	wp_6	wp_7
PID	0.0650	4.8220	nr	nr	nr	nr	nr
Slid. mode	0.0650	3.1120	5.9410	9.2630	13.9340	nr	nr

Where *nr* stands for not reached, and it means that the RoboSalmon has not been able to reach the waypoint.
The difference between the guidance and control system implemented on the RoboSalmon with

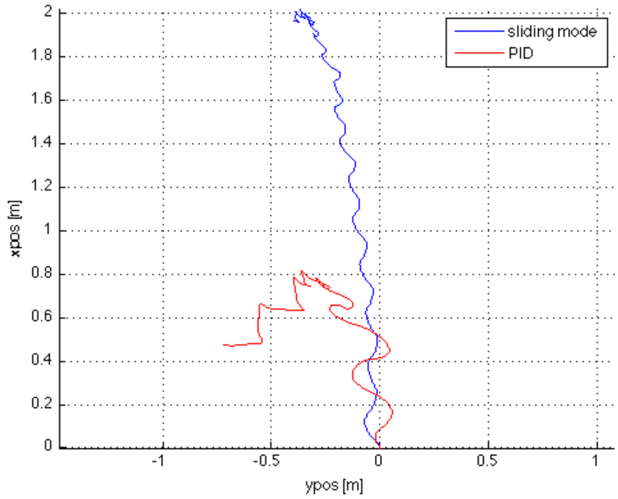

Figure 6.1: Motion of the RoboSalmon following the straight line path, in presence of growing current velocity amplitude and costant direction.

the sliding mode control or the PID control for the heading control is really important as it can be noticed analysing the simulation.
The performance of the RoboSalmon with the PID algorithm degrades fastly with the increase of the current velocity amplitude. The reason for this behaviour is to be found analysing the following Figure 6.2.

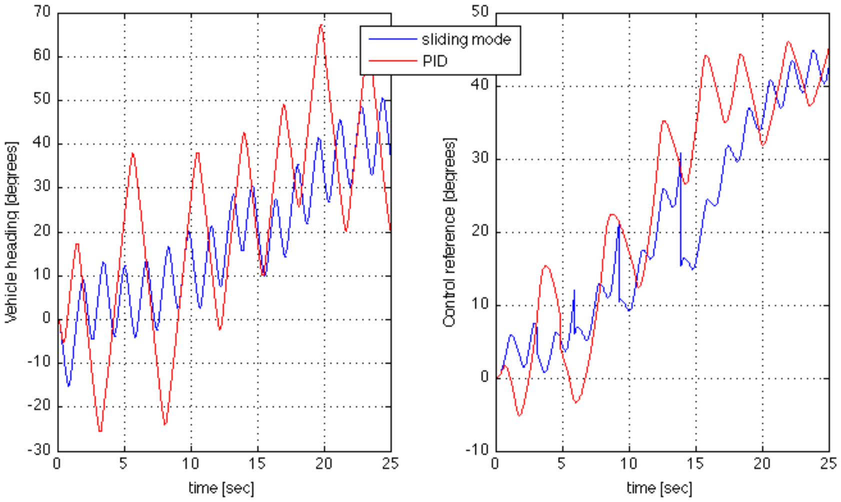

Figure 6.2: Heading of the RoboSalmon (on the left) and reference heading (on the right).

In particular, analysing the heading of the RoboSalmon during the manouevering phase (the figure on the left), it can be noticed that the amplitude of the oscillations using the PID controller is higher than the one noticed using the sliding mode control. On the opposite the frequency of the oscillations results to be lower when using the PID control algorithm. This behaviour, as explained in the previous section, is due to the saturation of the control signal and it is the reason why the guidance and control system implemented on the RoboSalmon with the PID heading control results to be less robust to the ocean current disturbances.

In the Figure 6.2 both the graph of the heading and the reference heading start from zero and then increase in order to compensate the current dusturbance.

Even if the performance of the RoboSalmon using the sliding mode control is better than the one using the PID control, it can be noticed that the last two waypoints can not be reached. This means that, for current velocity amplitude higher than 0.1 (m/s), the performace in term of path following decreases rapidly.

In particular, for current velocity amplitude around 0.2 (m/s), the current moves the vehicle on the 45 degrees direction, making the RoboSalmon to turn, as it can be seen in the following Figure 6.3.

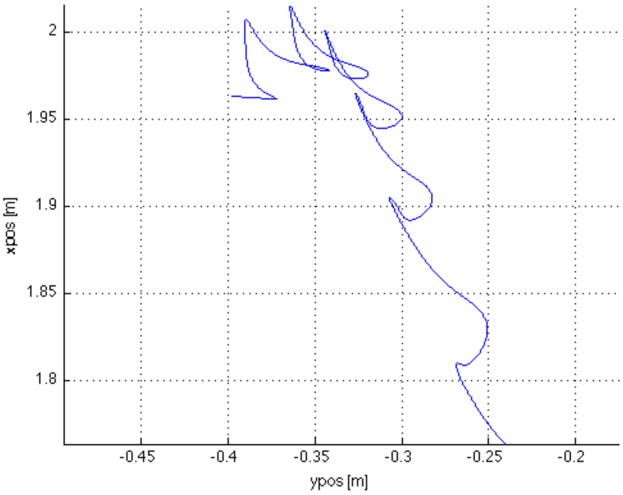

Figure 6.3: Particular of the last seconds of the manouevering phase for the RoboSalmon with the sliding mode heading control.

6.3.2 Orthogonal direction current

During this part of the project the reaction of the RoboSalmon to a costant velocity current orthogonal to the motion of the vehicle has been studied. The amplitude of the average current used throughout the simulations has been chosen to be $V_c = 0.05$.

The direction of the current, as previously mentioned, is orthogonal to the motion of the RoboSalmon vehicle. This means that the direction of the current changes everytime the heading reference changes, namely everytime one waypoint is reached and the navigation plan switch to the next waypoint.

Even in this section a comparisons between the two heading control algorithms has been brought forward.

In Figure 6.4 the motion of the RoboSalmon vehicle using both the algorithms for the heading control, together with the line of sight guidance law, is presented.

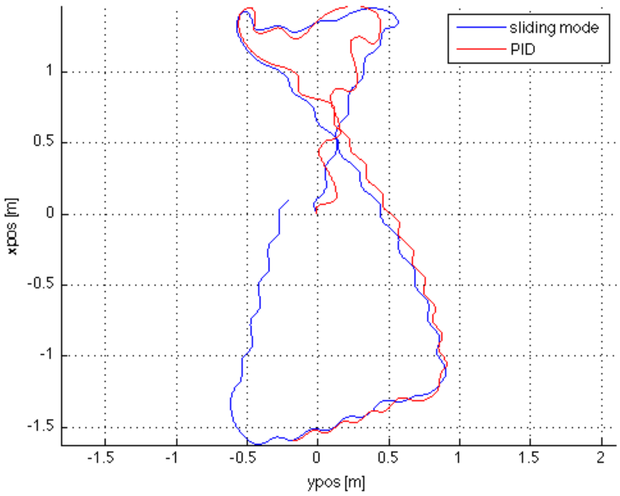

Figure 6.4: Motion of the RoboSalmon vehicle following the figure of eight path in the presence of orthogonal ocean current.

Analysing the motion of the RoboSalmon it can be noticed that the behaviour of the two heading control algorithms, the sliding mode and the PID, is approximately the same in the presence of the ocean current. This means that the sliding mode control still guarantees better performances than the PID algorithm, however the presence of the ocean current disturbance has the same effect in both the algorithms.
Clearly the disturbance affects the motion of the vehicle, however the waypoint can be reached with both the algorithms thanks to the small amplitude of the average current speed.

Also in this section the powers can be analysed. The graph of the motion and electrical powers has not been shown, although in the following table the average powers can be seen.

	average elec. power	average mot. power
PID	0.5858	0.0753
with orth. current	0.5776	0.0995
slid. mode	0.6219	0.2089
with orth. current	0.6237	0.2097

It can be noticed that there's no consistent difference in the average electrical power consumption with or without the ocean current disturbance, for both the heading control algorithms. Also the motion power generated by the tendon drive propulsion system doesn't significantly change when the sliding mode control algorithm is used.
However, the fact that the average motion power, using the PID controller, is higher in the presence of the ocean current disturbance is not easily explainable. Probably the current direction, being orthogonal to the motion, helps to decrease the oscillations amplitude, and at the

same time the recoil motion.

In Figure 6.5, the heading of the RoboSalmon and the reference heading during the manouevering are shown. Both the graph are presented using the PID and the sliding mode control algorithm.
Note that the reference heading is the output of the line of sight guidance law.

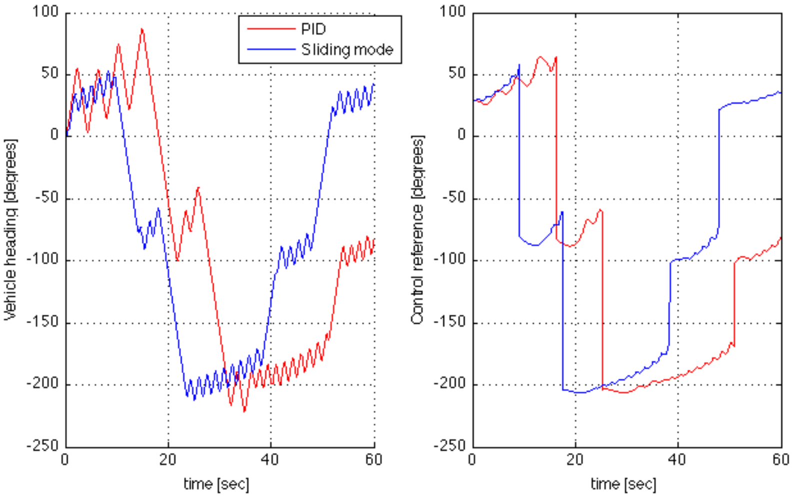

Figure 6.5: Heading of the RoboSalmon (on the left) and reference heading (on the right).

The first thing to notice is that, using the sliding mode heading control, the vehicle is faster. This behaviour has also been noticed in the prevoius section, and it's due to the higher motion power efficiency involved using the sliding mode algorithm.
Another thing to be noticed concerns the oscillation of the vehicle's heading. Using the PID heading control the oscillations have an higher amplitude than the one using the sliding mode. As it can be seen in the figure, the oscillations in the heading are transmitted to the reference heading.

6.3.3 Opposite direction current

In this part of the project the behaviour of the RoboSalmon with a constant velocity current opposite to the motion of the vehicle has been studied. The amplitude of the average current used throughout the simulations has been chosen to be $V_c = 0.05$, as the one used for the orthogonal direction current.
The direction of the current, as previously mentioned, is opposite to the motion of the RoboSalmon vehicle. This means that the direction of the current changes everytime the heading reference changes, namely everytime one waypoint is reached and the navigation plan switch to the next waypoint.
Even in this section a comparisons between the two heading control algorithms has been brought forward.
In Figure 6.6 the motion of the RoboSalmon vehicle using both the algorithms for the heading

control, the sliding mode control and the PID controller is shown. The line of sight algorithm designed in the project has been used as guidance strategy.

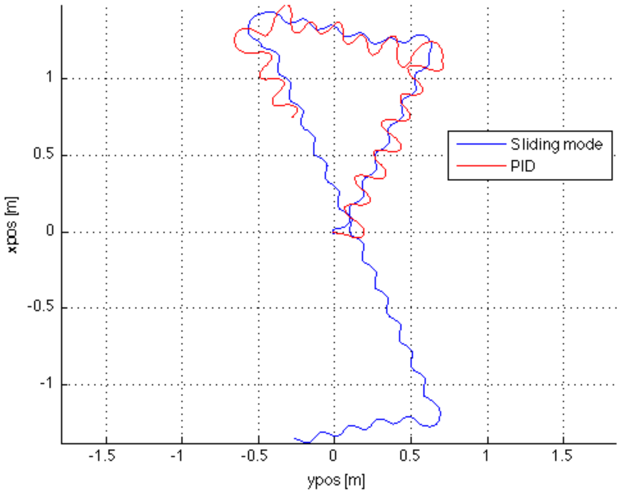

Figure 6.6: Motion of the RoboSalmon vehicle following the figure of eight path in the presence of orthogonal ocean current.

On the contrary of what have been seen for the orthogonal current direction, in this case the disturbance introduced by the opposite direction current affects deeply the performace of the RoboSalmon vehicle. It can be noticed that, using the PID control, only two points are reached in sixty second. Also using the sliding mode algorithm, the presence of the ocean current decreases the velocity of the RoboSalmon.
The reason for this degradation probably lies in the shape of the RoboSalmon's hull, which is not aerodynamic as the fishes one. Moreover, the direction of the current, being always opposite to the motion of the vehicle, increases the recoil motion and, at the same time, the amplitude of the oscillations. Despite the performance degradation, the waypoints can still be reached, even if it takes more time.

Also in this section the powers can be analysed. The graph of the motion and electrical powers has not been shown, although in the following table the average powers can be seen.

	average elec. power	average mot. power
PID	0.5858	0.0753
with opp. current	0.5869	0.0734
slid. mode	0.6219	0.2089
with opp. current	0.6311	0.2317

It can be seen that there's no consistent difference in the average electrical power consumption with or without the ocean current disturbance, for both the heading control algorithms. Also the motion power prodiced by the tendon drive propulsion system doesn't significantly change when the PID control algorithm is used.

However, the fact that the average motion power, using the sliding mode controller, is higher in the presence of the ocean current disturbance is not easily explainable.

The heading of the RoboSalmon during the manouevering and the reference heading, output of the line of sight guidance law, are shown in Figure 6.7. Both the graph are presented using the PID and the sliding mode control algorithms.

The first thing to notice is that, using the sliding mode heading control, the vehicle is faster.

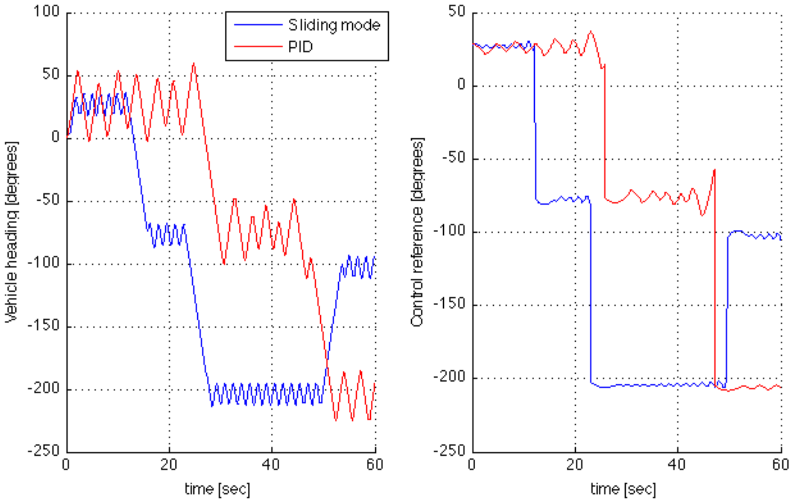

Figure 6.7: Heading of the RoboSalmon (on the left) and reference heading (on the right).

This behaviour has also been noticed in all the prevoius simulations, and it's due to the higher motion power efficiency involved using the sliding mode algorithm.

Another thing to be noticed concerns the oscillation of the vehicle's heading, which is way higher than the one seen when the direction of the current was orthogonal to the motion. Using the PID heading control the oscillations have an higher amplitude than the one using the sliding mode. As it can be seen in the figure, the oscillations in the heading, affecting the position of the vehicle, are transmitted to the reference heading elaborated by the LOS algorithm in order to reach the waypoint.

Chapter 7

Conclusions and Further Works

The task of the project presented in the thesis was the design of a suitable control and guidance system for the navigation of the RoboSalmon biomimetic vehicle. As it has been said in the prevoius chapters, the task as been accomplished. There have been designed and implemented two different control systems, the PID control algorythm and the sliding mode control. While, as a guidance system, only the Line of Sight guidance law has been implemented.
The whole control and guidance system has then been analysed in the presence of disturbances, namely the influence of the ocean currents.

The first thing to notice about the control system implemented is that both the PID algorythm and the sliding mode control allow to follow the desired heading reference.
It has been noticed that the sliding mode control, when implemented in the steering control system, guarantees better performances than the ones achievable with the PID control.
The PID control algorythm has been designed using the RoboSalmon linearized system for small reference heading, and, due to the highly non-linear and coupled dynamics of the RoboSalmon system, the performances of the controlled system rapidly decreases with the increase of the reference heading value. On the other side, the sliding mode control has been designed for the dynamics of the RoboSalmon and guarantees better performances. In particular, it has been seen that, when the PID control is used, the saturation of the control output, namely the tail centreline, makes the tail to oscillate with the maximum amplitude, causing a greater loss of energy due to the recoil motion.
Anyway, during the simulation trials it has been seen that both the algorythms allow to reach and maintain reference headings that can go from 0 degrees to ±180 degrees, making suitable the implementation of a guidance system.

Regarding the guidance law, the line of sight algorithm implemented on the RoboSalmon vehicle is very simple and requires some attention only in the selection of the proper quadrant, in order to avoid the singularity of the tangent function. Furthermore, together with the heading control, it has proved to guarantee good perfomances in terms of waypoint reaching, as shown in the simulations described in the prevoius chapter.
Concerning the heading control, a comparison between the two heading control algorithms designed for the RoboSalmon, The PID controller and the sliding mode control, has been brought forward throughout the project.
In conclusion it can be said that the sliding mode control guarantees better perfomances than

the PID controller. The reason is to be found in the fact that the sliding mode algorithm is designed to work on highly non-linear and coupled systems, while the PID control has been designed with the linearization method around a working point, and, when the working point moved from the one chosen for the linearization, the performances degrade quickly.
Analysing the control signal, namely the output of the heading control algorithm, using the PID controller, it has been seen in the simulations that it often saturates. Since the control signal is the tail centreline, the saturation of the control signal directly results in high amplitude oscillation of the tendon drive tail. As already mentioned, the problem of the recoil motion is due to the mechanical implementation of the tendon tail propulsion system, and the increase in the oscillations amplitude creates an increase in the loss of energy due to the recoil motion. Using the sliding mode control the problem of the recoil motion has not been solved, but at least the degradation of the efficiency is lower then the one seen using the PID control. As it has been seen during the analysis of the powers involved during the motion, for almost the same electrical power consumption, the motion power produced by the tendon drive propulsion system is almost three times higher when the sliding mode control is used instead of the PID algorythm as steering control system.

In the last chapter of the paper the behaviour of the system in the presence of the ocean current disturbances has been analysed. The first and most important thing to notice is that the RoboSalmon has accetable performances in terms of path following only in presence of relatively low amplitude average current speed. This means that the RoboSalmon vehicle can be used only in specific environment, where the current is absent or, at least very low.
Even during these simulations it has been noticed that the guidance and control systems designed for the RoboSalmon result to be more robust to the current dusturbances using the sliding mode heading control implementation. In fact, the maximum average current velocity that can be applied on the RoboSalmon with the sliding mode algorithm is almost two times the one that can be applied when the PID control algorithm is used.
The simulations with different current directions described in the last section emphasize the performances of the guidance and control systems designed. In particular it has been seen again that the sliding mode control algorithm allows better performances in terms of path following, even in presence of small amplitude ocean current disturbances.

The main problem with the RoboSalmon is the recoil motion. The guidance and control algorithm designed is not able to solve the problem because it is due to the mechanical implementation of the tendon drive tail system.
In order to solve the problem, a different mechanical implementation of the tendon tail drive propulsion system can be studied. In particular, it is thought to be necessary the use of more actuators, one actuator for each joint is enough to control the tail and makes it oscillating without changing the its centre of mass. This new implementation should be enough to solve or, at least, reduce the recoil motion.
Another thing that can be further analysed is the heading control itself, a more sophisticated algorythm can be used. Also, the steering control can be obtained in a different way than the control of the tail centreline, however this is an open issue in the research community.

Appendix A

Constants

The constants used within the mathematical model of the RoboSalmon, introduced in chapter 2, are defined below.

$$
\begin{aligned}
\text{Mass:} \quad & m &=& \; 4.88kg \\
\text{Length:} \quad & l &=& \; 0.85m \\
\text{Displacement:} \quad & V &=& \; 4.9L \\
\text{Semi-axis:} \quad & a &=& \; 0.425m \\
& b &=& \; 0.08m \\
& c &=& \; 0.08m \\
\text{Caudal fin height} \quad & h &=& \; 0.15m \\
\text{Caudal fin lenght} \quad & l_{fin} &=& \; 0.105m \\
\text{Caudal fin area:} \quad & A_{fin} &=& \; 0.10079m^2 \\
\text{Moments of inertia:} \quad & J_x &=& \; 0.0125kgm^3 \\
& J_y &=& \; 0.1825kgm^3 \\
& J_z &=& \; 0.1825kgm^3 \\
\text{Added mass derivatives:} \quad & X_{\dot{u}} &=& \; -0.4296 \\
& Y_{\dot{v}} &=& \; -4.1957 \\
& Z_{\dot{w}} &=& \; -4.1957 \\
& K_{\dot{p}} &=& \; 0 \\
& M_{\dot{q}} &=& \; -0.1098 \\
& N_{\dot{r}} &=& \; -0.1098
\end{aligned}
$$

Bibliography

[1] Barrett D. S, 1996. *The design of a flexible hull undersea vehicle propelled by an oscillating foil.* MS Thesis, Department of Ocean Engineering, Massachusetts Institute of Technology.

[2] Anderson J. M., P. A., 2000. *The vorticity control unmanned undersea vehicle (VCUUV): an autonomous robot tuna.* Draper Technology Digest.

[3] Atherton E., 2009. *Boston Engineering, TS1166-ROBO, Autonomous fish: swarms, surveillance, and swimming.*

[4] Kumph J. M., 2000. *Maneuvering of a robotic pike.* MS Thesis, Department of Ocean Engineering, Massachusetts Institute of Technology.

[5] Hirata K., Takimoto T., Tamura K., 2000. *Study on turning performance of a fish robot.* In Proceedings of the First International Symposium on Aqua bio-mechanisms.

[6] Hirata K., 2000. National Maritime Research Institute of Japan, Welcome to fish robot home page.

[7] Nakashima M., Ono K., 2002. *Development and experiment of two-joint dolphin robot.* Neurotechnology for biomimetic robots.

[8] Nakashima M., Takashi Y., Ono K., 2004. *Threedimensional manoeuvrability of the dolphin robot.* Bio-mechanisms of swimming and flying.

[9] Dogangil G., Ozcicek E., Kuzucu A., 2005. *Design, construction, and control of a robotic dolphin.* Proceedings of the International Conference on Robotics and biomimetics.

[10] Liu J., 2007. *Modelling and online optimisation of robotic fish behaviours.* PhD Thesis, University of Essex.

[11] Hu H., 2006. *Biologically inspired design of autonomous robotic fish at Essex.* Proceedings of the Fifth IEEE UK and RI Chapter Conference on Advances in cybernetic systems.

[12] Liang J., Wang T., Wang S., Zou D., Sun J., 2005. *Experiment of robofish aided underwater archaeology.* Proceedings of the International Conference on Robotics and biomimetics.

[13] Wang T., Wen L., Liang J., Wu G., 2010. *Fuzzy vorticity control of a biomimetic robotic fish using a flapping lunate tail.* J. Bionic Engng.

[14] Beal D. N., 2003. *Propulsion through wake synchronization using a flapping foil.* PhD Thesis, Department of Mechanical Engineering, Massachusetts Institute of Technology.

[15] Valdivia y Alvarado P., 2007. *Design of biomimetic compliant devices for locomotion in liquid environments.* PhD Thesis, Department of Mechanical Engineering, Massachusetts Institute of Technology.

[16] Kato N., 2000. *Control performance in the horizontal plane of a fish robot with mechanical pectoral fins.* IEEE J. Oceanic Engng.

[17] Georgiades C., German A., Hogue A., Liu H., Prahacs C., Ripsman A., Sim R., Torres L. A., Zhang P., Buehler M., Dudek G., Jenkin M., Milion E., 2004. *AQUA: an aquatic walking robot.* Proceedings of the IEEE/RSJ International Conference on Intelligent robots and systems.

[18] Licht S. C., 2008. *Biomimetic oscillating foil propulsion to enchance underwater vehicle agility and maneuverability.* PhD Thesis, Massachusetts Institute of Technology.

[19] Licht S., Polidoro V., Flores M., Hover F. S., Triantafyllou M. S., 2004. *Design and projected performance of a flapping foil AUV.* IEEE J. Oceanic Engng.

[20] 2010. iRobot, Maritime robots, Transphibian.

[21] Long Jr J. H., Schumacher J., Livingston N., Kemp M., 2006. *Four flippers or two? Tetrapodal swimming with an aquatic robot.* Bioinspiration Biomimetics.

[22] 2007. Festo, AquaRay.

[23] 2009. Festo, AquaPenguin.

[24] 2010. EvoLogics, Subsea glider with fin ray effect.

[25] Cai Y., Bi S., Zheng L., 2010. *Design and experiments of a robotic fish imitating cow-nosed ray.* J. Bionic Engng.

[26] Epstein M., Colgate J., MacIver M., 2006. *Generating thrust with a biologically inspired robotic ribbon fin.* Proceedings of the IEEE/RSJ International Conference on Intelligent robots and systems.

[27] Low K. H., Willy A., 2006. *Biomimetic motion planning of an undulating robotic fish fin.* J. Vibr. Control.

[28] Simons D., Bergers M., Henrion S., Hulzenga J., Jutte R., Pas W., van Schravendijk M., Vercruyssen T., Wilken A., 2009. *A highly versatile autonomous underwater vehicle with biomechanical propulsion.* Proceedings of Oceans.

[29] Yu J., Hu Y., Huo J., Wang L., 2007. *An adjustable scotch yoke mechanism for robotic dolphin.* Proceedings of the International Conference on Robotics and biomimetics.

[30] Hu Y., Wang L., Yu J., Huo J., Jia Y., 2008. *Development and control of dolphin-like underwater vehicle.* Proceedings of the American Control Conference.

[31] Guo J., 2006. *Guidance and control of a biomimeticautonomous underwater vehicle.* Advances in unmanned marine vehicles.

[32] Zhou C., Tan M., Gu N., Cao Z., Wang S., Wang L., 2008. *The design and implementation of a biomimetic robotic fish.* Int. J. Advd Robotic Systems.

[33] Watts C.M., 2009. *A Comparison Study of Biologically Inspired Propulsion Systems for an Autonomous Underwater Vehicle.* PhD Thesis, University of Glasgow.

[34] Fossen T.I., 2002. *Marine Control Systems.* Norway, Marine Cybernetics.

[35] Fossen T.I., 1994. *Guidance and Control of Ocean Vehicles.* West Sussex UK, John Wiley & sons Ltd.

[36] Lin C.F., 1991. *Modern Navigation, Guidance, and Control Processing, Volume II.*

[37] Draper C. S., 1971. *Guidance is forever.* Navigation 18.

[38] Locke A. S., 1955. *Guidance.* D. Van Nostrand Company, Inc.

[39] Zarchan P., 2002. *Tactical and Strategic Missile Guidance.* American Institute of Aeronautics and Astronautics, Inc.

[40] Bryson A. E. Jr., Ho Y. C., 1969. *Applied Optimal Control.* Blaisdell, Waltham, MA, USA.

[41] Nazaroff G. J., 1976. *An optimal terminal guidance law.* IEEE Trans. Automat. Contr.

[42] Potter J. E., 1964. *A guidance-navigation separation theorem.* AIAA Paper AIAA, Washington DC, USA.

[43] Speyer J. L., Greenwell W. M., Hull D. G., 1982. *Adaptive noise estimation and guidance for homing missile.* AIAA Guid. and Contr. Conf., Washington DC, USA.

[44] Briest S., Cowen S., Dombrowski J., 1997. *Underwater docking of autonomous undersea vehicles using optical terminal guidance.* Oceans'97 MTS/IEEE Conference Proceedings, Halifax, Canada, Vols 1.

[45] Gaskett C., Wettergreen D., Zelinsky A., 1999. *Autonomous guidance and control for an underwater robotic vehicle.* International Conference on Field and Service Robotics.

[46] Balasuriya A., Ura T., 1998. *Autonomous target tracking by underwater robots based on vision.* Proceedings of IEEE UT'98.

[47] Rock S. M., Lee M. J., Wang H. H., Marks R. L., Burton R. C., 1992. *Combined camera and vehicle tracking of underwater objects.* Proceedings of ROV'92.

[48] Consi T. R., Goudey C. A., Cho J., Atema J., Chryssostomidis C., 1994. *AUV guidance with chemical signals.* Proceedings of the 1994 Symposium on Autonomous Underwater Vehicle Technology.

[49] Feezor M. D., Sorrell F. Y., Blankinship P. R., Bellingham J. G., 2001. *Autonomous underwater vehicle homing/docking via electromagnetic guidance.* IEEE Journal of Oceanic Engineering.

[50] Healey A. J., Lienard D., 1993. *Multivarible Sliding Mode Control for Autonomous Diving and Steering of Unmanned Underwater Vehicles*. IEEE Journal of Oceanic Enineering.

[51] Naeem W., Sutton R., Ahmad S.M., Burns R.S., 2003. *A Review of Guidance Laws Applicable to Unmanned Underwater Vehicles*. The Journal of Navigation.

[52] Breivik M., Fossen T.I.. *Guidance Laws for Autonomous Underwater Vehicles*

[53] Roper D.T., Sharma S., Sutton R., Culverhouse P., 2011. *A review of Developments towards Biologically Inspired Propulsion Systems for Autonomous Underwater Vehicles*. Proceedings of the Institution of Mechanical Engineers, Part M: Journal of Engineering for the Maritime Environment.

[54] Young K. D., 1999. *A Control Engineer's Guide to Sliding Mode Control*. IEEE Transactions on Control Systems Technology.